NASA Contractor Report 4327

Magnetic Suspension and Balance System Advanced Study—Phase II

R. W. Boom, M. K. Abdelsalam,
Y. M. Eyssa, and G. E. McIntosh
Madison Magnetics, Inc.
Madison, Wisconsin

NASA

National Aeronautics and
Space Administration

Office of Management

Scientific and Technical
Information Division

1990

PHASE II PROJECT SUMMARY
OF NASA CONTRACT NAS1-18279

"Magnetic Suspension and Balance System Advanced Study"

The objectives of this study are to experimentally confirm several advanced design concepts on Magnetic Suspension and Balance Systems (MSBS). The advanced design concepts were identified as potential improvements by Madison Magnetics, Inc. (MMI) during 1984 and 1985 studies of an MSBS utilizing 14 external superconductive coils and a superconductive solenoid in the airplane test model suspended in a wind tunnel. The design concepts, now based on confirmed experiments, are substituted in the 1985 MSBS design to provide the new 1989 MSBS design.

Specifically, the project objectives are: 1) full-scale solenoid construction and test for the F16 airplane model, 2) small-scale solenoid development toward high current density, 3) mechanical tests of new permanent magnet wings materials, and 4) a new MSBS design using these accomplishments.

All objectives are achieved. The 1989 improvements over previous MMI designs are shown below. The weight and power savings result in a 1989 inflation-adjusted cost estimate of $19.1 M compared to $21.5 M in 1985 and to $88 M in 1981. The improvements are due to: the holmium insert in the model coil; 100% of wing volume is new permanent magnet material; fiberglass-epoxy structure instead of stainless steel; and shorter saddle roll coils.

Specifications

MMI DESIGNS	COST (10^6)	SYSTEM (tonnes)	COIL (tonnes)	CONDUCTOR (MAm)	LIQUEFIER (ℓ/h)
1984	29.9	368	171	755	560
1985	21.5	210	80.9	468	379
1989	19.1	140	47.9	341	299

Performance

MMI DESIGNS	MOMENT (10^4Am^2)	WING B$_r$ (T)	AC LOSS (W)	ENERGY (MJ)	POWER (MW)
1984	2.63	0.70	2212	906	97.2
1985	3.12	0.98	522	408	31.2
1989	2.89	1.2	374	222	18.3

An additional task, not in the original statement of work, is the conceptual design of a new compact configuration of external solenoids which eliminates specific roll coils. In principle, unlimited pitch and roll angles should be achieved and drag coils could be reduced or eliminated. Savings up to 30% of the magnet cost from the 1985 cost estimate are possible, or an equal cost-equal size MSBS unit could be built with much better operational specifications.

FOREWORD

The purpose of this report is to present the results of an advanced study of a Magnetic Suspension and Balance System suitable for a wind tunnel having an 8 ft. x 8 ft. test section capable of operating at speeds up to Mach 0.9 with ± 0.1% control forces at 10 Hz for an F16 model airplane. Full-scale model core superconductive solenoid tests and integrated magnet system design advance the status of feasibility for the construction of a superconductive MSBS.

R. W. Boom, M. K. Abdelsalam, Y. M. Eyssa and G. E. McIntosh are the major contributors to the study.

Use of trade names or names of manufacturers in this report does not constitute an official endorsement of such products or manufacturers, either expressed or implied, by the National Aeronautics and Space Administration.

v

TABLE OF CONTENTS

LIST OF FIGURES

LIST OF TABLES

REFERENCES

[1] H.L. Bloom, et al., "Design Concepts and Cost Studies for Magnetic Suspension and Balance Systems," NASA CR-165917, July 1982.

[2] R.W. Boom, Y.M. Eyssa, G.E. McIntosh, and M.K. Abdelsalam, "Magnetic Suspension and Balance System Study," NASA CR-3802, July 1984.

[3] R.W. Boom, Y.M. Eyssa, G.E. McIntosh, and M.K. Abdelsalam, "Magnetic Suspension and Balance System Advanced Study," NASA CR-3937, October 1985.

[4] C. Britcher, M.J. Goodyer, R.G. Scurlock, and Y.Y. Wu, "A Flying Superconducting Magnet and Cryostat for Magnetic Suspension of Wind-Tunnel Models," Cryogenics, Vol. 24, No. 4, April 1984.

[5] W. Schauer and F. Arendt, "Field Enhancement in Superconducting Solenoids by Holmium Flux Concentrators," Cryogenics, Vol.23, No. 10, October 1983.

[6] R.W. Hoard, et al., "Field Enhancement of a 12.5 T Magnet Using Holmium Poles," IEEE Trans. on Magnetics, Vol. MAG-21, No. 2, March 1985.

[7] Xu Peifei, et al., "Superconducting Magnets Impregnated with Epoxy Resins," Proc. of the ICEC 10, Butterworth, 1985.

[8] M. Sagawa, et al., "Permanent Magnet Materials Based on the Rare Earth - Iron - Boron Tetrogonal Compounds," IEEE Trans. on Magnetics, Vol. MAG-20, No. 5, September 1984.

[9] S. Arai and T. Shibata, "Highly Heat Resistant Nd-Fe-Co-B System Permanent Magnets," paper presented at the 1985 INTERMAG Conference, St. Paul, Minnesota.

[10] Li Chengren and D.C. Larbalestier, "Development of High Critical Current Densities in Niobium 46.5% Titanium," Cryogenics, Vol. 27, No.4, April 1987.

[11] D.C. Larbalestier, Li Chengren, W. Starch, and P.J. Lee, "Limitation of Critical Current Density by Intermetallic Formation in Fine Filament Nb-Ti Superconductors," IEEE Transactions on Nuclear Science, NS 32 (1985).

[12] S.H. Kim, S.T. Wang, and M. Lieberg, "Operating Characteristics of a 1.5 MJ Pulsed Superconducting Coil," Advances in Cryogenic Engineering, Vol. 25, Plenum Press, NY, 1980, pp. 90-97.

1. INTRODUCTION

1.1 Background

Magnetic suspension and balance systems (MSBS) for wind tunnels have been increasingly developed and utilized during the past 25 years. The primary aerodynamic advantage of MSBS is the elimination of air flow disturbances caused by the test model mechanical support system and by the required alterations in the test model. The primary technological advantages of MSBS are that static and dynamic forces and torques on the test model can be applied and recorded (from magnet currents) without the severe sting restraints.

The potential availability of MSBS for large transonic tunnels improves steadily in line with the development of the new high temperature superconductor materials and the expanded use of low temperature superconductive magnet systems in many fields, such as: high energy physics and energy storage. Compact superconductive systems provide high magnetic fields on the test model.

The design studies by General Electric [1] in 1981 and by Madison Magnetics in 1984 [2] and 1985 [3], and a pilot model at Southampton in 1983 [4] show that practical full-size superconductive MSBS systems can be built well within the present state of the art for superconductive systems. Design improvements and cost reductions continue in this Phase II-1989 design study for a MSBS suitable for an 8' x 8' test section at Mach 0.9 with ± 0.1% control forces at 10 Hz for an F16 model airplane.

1.2 **Summary**

The two conceptual MSBS designs for 8' x 8' wind tunnels in this Phase II study by Madison Magnetics Inc. (MMI) continue the trend of improvements that was started with the MMI-1984 and MMI-1985 MSBS designs. These MMI-1989 and MMI-1990 designs have more flexibility in magnet choices and more control capabilities with simpler coil configurations than previously.

In Chapter 2 the six principal objectives of this Phase II study are outlined in preparation for the work reported in later sections. The first four objectives cover experimental projects to demonstrate improved components. The final two objectives are extensions of the MMI design studies labeled here as MMI-1989 and MMI-1990 MSBS designs.

In Chapter 3, section 3.1 a full-scale model core solenoid is built, tested, and qualified for use in an F16 airplane model. The critical aspects of a solenoid in a tight-fitting portable cryostat container are dealt with by experimental staged improvements until a workable final system is completed. The recommendations for best design based on this experiment provide a conservative, high magnetic moment model core solenoid at 30 kA/cm^2 which will be a good candidate for the first 8' x 8' tunnel.

In Section 3.2 a higher current density solenoid development is attempted to prove that using a higher thermal enthalpy potting epoxy would allow higher current densities. This effort is only marginally successful. By indirect interpretation it appears that a potted solenoid with a

2

special mixture of epoxy and high specific heat ceramic powder may survive a thermal disturbance of about 1.29 K at 6 T compared to 1.20 K for standard epoxy potting. The difference, 0.09 K is just slightly larger than the measurement uncertainty. The enthalpy-stability potting idea to help absorb thermal disturbances is a new avenue for improvements. One could wish that the improvement here might be larger, and, therefore, more certain. It may be that this is a first step in the right direction. At least the technology of doping an epoxy with a thermal stabilizing ceramic, SCIA, should be of general use for many cryogenic and superconductive purposes in NASA and elsewhere.

In Section 3.3 the use of the permanent magnet material Nd-Fe-B (Neomax trade name) for wings of an F16 model is solidified by bending strength measurements which show that Neomax is strong enough to use without stainless steel skin support. The general replacement of magnetized soft iron wings by high performance rare earth permanent magnet material is an enormous advance for MSBS model roll characteristics. External superconductive roll coils can thereby be significantly smaller, less powerful, and less expensive.

In Section 3.4 an extended MSBS design is undertaken to essentially solidify the 1985 design with the actual experimental achievements replacing previous conceptual designs. The solenoid parameters are about as predicted, except now the magnetic moment is known and proven. Not all design and construction choices were best; in particular the design was too tight as a result of trying for too high a

3

magnetic moment. But at least now it is known what is critical and what should be achieved. A clear example of one item illustrates the more general conclusions to this work: in a prescribed 75 cm long envelope MMI built and tested a solenoid with active windings 70 cm long, which leaves only 2.5 cm on each end for support and thermal transition from 4.2 K to 300 K. Based on this Phase II construction experiment we recommend 5 cm on each end to get better helium hold time.

The MMI-1989 redesign has an improvement of 30% reduction in ampere-meters and 50% reduction in energy stored over the 1985 design. These improvements are mainly due to the removal of skin support in model wings and optimizing the locations of the 14 suspension coils.

In Section 3.5 a new integrated design approach, MMI-1990, is presented primarily to make use of simple external solenoids instead of the more complicated saddle roll coils of the MMI-1989 design. The MSBS system cost estimates are slightly reduced by properly sharing the force requirements more widely between coils. When the new high T_c brittle superconductors become available their first use will be in simple solenoid configurations with simpler stress problems than in complicated windings such as the saddle coils.

2. PHASE II TECHNICAL OBJECTIVES AND APPROACH

The thirteen original objectives of Phase I were achieved and justify the selection of four key objectives for Phase II. These objectives are: 1) full-scale solenoid construction and test for the F16 airplane model, 2) small-scale solenoid development toward the highest current density, 3) mechanical tests of new permanent magnet wings materials, and 4) a new 1989 MSBS design using the above three Phase II objective accomplishments.

A fifth objective added to the Phase II tasks is to incorporate a new integrated system design philosophy which is an attempt to take advantage of cross coupling between X, Y, and Z coils and thereby to achieve a simpler system with more capability.

2.1 Full-Scale Model Solenoid

The magnetic pole strength and moment of the persistent superconducting solenoid in the F16 model determine the size of the external X and Z coils. Any required force is the product of the pole strength times the external field and a required torque is the product of solenoid moment times the external field. Thus, doubling the model coil pole strength could reduce to half the required size of external X and Z coils. The economic impact of the solenoid performance is immense; a small $150,000 component determines the cost of the major part of the $18 M magnet system.

In the Phase I design a high current density of 30 kA/cm^2 at 6.1 tesla (T) was assumed for an epoxy impregnated coil.

Such coils do not contain much copper or cooled surfaces, their ability to tolerate disturbances is limited to the adiabatic heat capacity of the conductor material, and they can achieve 30 kA/cm^2 in less severely restricted shorter solenoids. The Phase I design is a precise tight-fitting cryostat. To verify the validity of the Phase I design, it is important to demonstrate that 30 kA/cm^2 solenoids can be built by commercial vendors, successfully mounted in tight-fitting cryostats and oscillated safely through specified angular ranges at 10 Hz. We contend that this is proof to demonstrate commercial industrial availability of the Phase I MSBS design, since the model solenoid is the most critical component.

The present Phase II design uses a holmium core mandrel. Holmium has superior magnetic properties at 4.2 K with a saturation magnetic moment of 3.9 tesla [5,6]. With the initial model coil specifications shown in Table 2.1-1, the total magnetic pole strength of holmium and winding is 4.45 x 10^4 Am.

The solenoids specified in Table 2.1-1 and in Fig. 2.1-1 are provided by commercial vendors using standard manufacturing techniques. The holmium coil form is provided separately by MMI. The persistent switch and electrical activation are procured from the coil manufacturer.

Standard industrial epoxy winding techniques are used. The epoxy must be flexible enough to stick to the coil form through cooldown contraction and through coil energization.

6
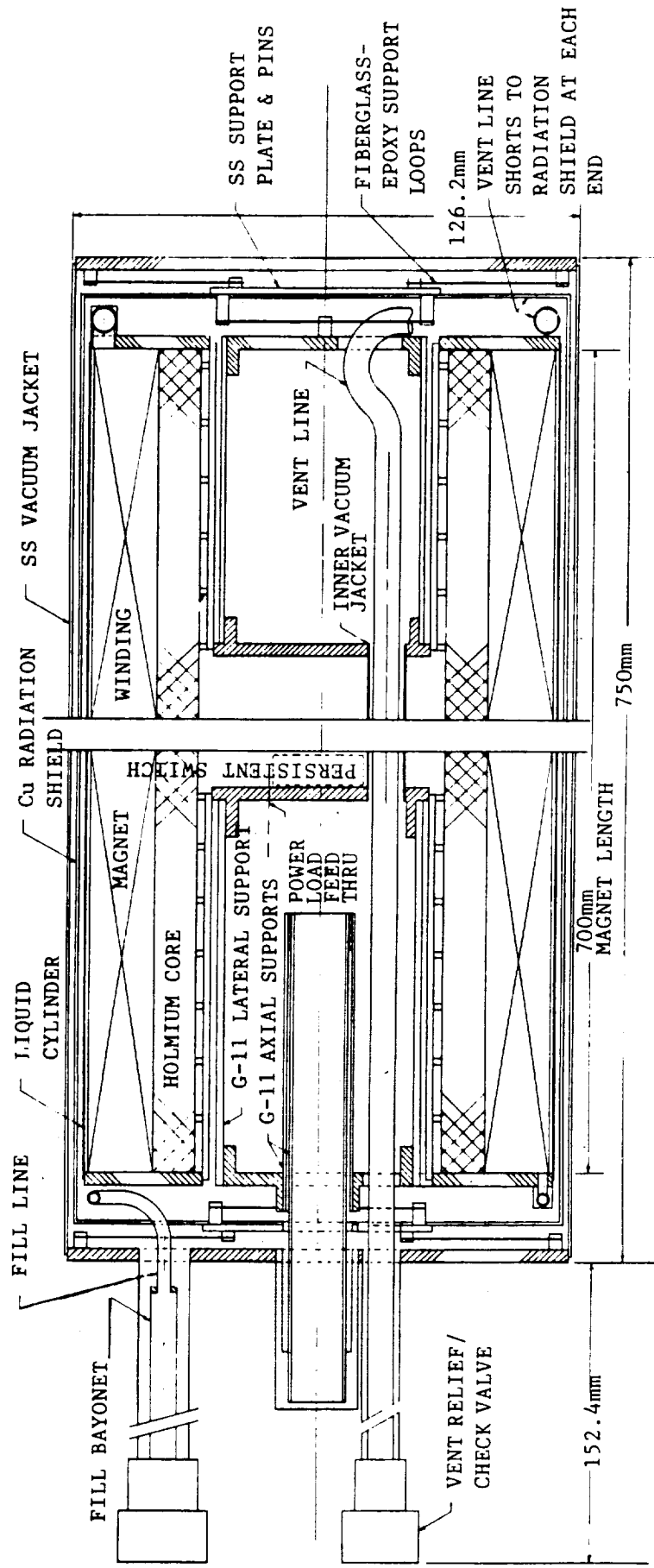
Figure 2.1-1. Core Magnet Cryostat.

7

The reason for permanently unitizing the coil form and coil winding is to minimize mechanical motion during 10 Hz oscillations. Epoxy should never crack from any cause.

Table 2.1-1

Initial Model Coil Specifications

	ID (cm)	OD (cm)	LENGTH (cm)	WEIGHT (kg)	MAGNETIC POLE STRENGTH (Am)
Winding	8.26	11.5	70	26.8	3.75×10^4
Mandrel	6.14	8.26	70	14.5	0.70×10^4
Total				41.3	4.45×10^4

The objectives for this solenoid are:

1. To achieve 6.1 tesla (T) at about 30 kA/cm^2 gross current density.

2. To limit ac losses for small external field change $\Delta B = 10^{-4}$ T at 10 Hz to less than 0.05 W.

3. To withstand 10 Hz mechanical oscillations.

Reliable performance of the model core magnet cryostat is necessary for effective utilization of the MSBS. The general operation of the components in Fig. 2.1-1 are given in Section 3.1.2. Essential requirements for the cryostat include:

▸   Mechanical integrity to withstand wind tunnel model aerodynamic loads.

▶ Low heat leak to support wind tunnel operations for several hours without re-supply of helium.

▶ Design for convenient, quick turn-around servicing.

The conceptual cryostat design in Fig. 2.1-1 embodies most of the required features. Supports are designed for the maximum lift force of 10^4 N plus 4g times the magnet weight for a total of 11.78×10^3 N with a safety factor of four. The calculated heat leak is 0.11 W resulting in a helium loss rate of 0.16 ℓ/h which provides a static hold time of 4.5 hours for the liquid level to drop from 90% to 50% full. The calculated full power operating time for 90% to 20% full is 5.6 hours, which conservatively supports a four-hour wind tunnel run.

Convenient operation means that the cryostat can be cooled down and filled in one to two hours by a skilled technician, even though hampered by the solid holmium core and potted magnet. The possible flow paths are milled radial grooves in the magnet retaining end plates and notches in the G-10 CR spacer rings. If needed, the fill point can be relocated to the center of the reservoir and the size of the vent port can be increased. Refilling with helium is through a special fill line with a bypass vent to prevent the introduction of warm vapor into the cryostat.

Several auxiliary devices not shown in Fig. 2.1-1 are required for safe operation of the cryostat. Most important is a power and instrumentation lead actuator, consisting of an

9

external bellows assembly and a mechanical latch attached to a guided thin wall G-11 CR tube with wires attached. When pushed in and latched, the circuits are completed for charging or discharging. In its normally retracted position there is a thermal gap in the wires to reduce heat leak. The cryostat has a combination vacuum pumpout-relief device for evacuation that protects the interior in case of a vacuum leak or helium shell rupture.

The objectives for the cryostat system are:

1. Mechanical fit and mounting for the solenoid

2. Adequate helium fill and vent tubes

3. Heat leak less than 0.12 W

4. Withstand 10 g.

2.2 High Current Density Solenoids

This second key objective is to investigate experimentally higher current density solenoids. There is evidence in the literature of solenoids with current densities higher than 30 kA/cm^2 which, however, is considered excellent. A recent publication of the Baoji Institute in China [7] lists characteristics higher than 60 kA/cm^2 for 10 to 20 cm long solenoids. The high current density is attributed to using epoxy windings and cores of similar cooldown contraction to limit stresses.

The MMI program is to use loaded epoxy with contraction coefficients similar to the stainless steel winding core and

the best available NbTi conductor. These two specifications might lead to higher current density solenoids.

Holmium insert core cylinders enhance the model core pole strength without increasing the field on the solenoid turns. A high current density winding would occupy less radial thickness and provide more radial space for holmium. An optimization procedure for maximum pole strength is to divide the available space between holmium, windings, and helium to produce a maximum pole strength for a required run time (helium volume). The ID of the core is fixed for a given helium volume and the OD of the winding is fixed by the size of the cryostat. The objectives for the high current density solenoid development are:

1. Develop a loaded epoxy with cooldown contraction similar to the coil form to limit differential stresses between coil and coil form.

2. Enhance the thermal conductivity and specific heat of the loaded epoxy by the selection of the loading additive for better local wire cooling.

3. Incorporate the best NbTi conductor and loaded epoxy into meaningful small test coils.

The objective of the experimental program is to produce coils with selected loaded epoxy impregnation, with the best NbTi conductor, and wound on the same winding ID as the full-scale solenoid in 2.1-1 for an assessment of training and reliability.

2.3 Permanent Magnet Wing Materials

The best new permanent magnet materials are iron-rare earth-boron which has a very high performance (high remanant magnetism B_r and high energy product B_rH_c) [8,9]. Nd-Fe-B compounds prepared by powder metallurgy show remarkable magnetic properties, high remanent magnetization (1.2 T) and high coercivity (>1T).

A typical method to manufacture a permanent magnet from these materials is to grind the alloy (which is prepared by arc melting) into a coarse powder of about 50 ~ 90 μm diam in a stainless steel grinding jar. Then the powder is ground finer in a vibrator mill, poured into a die in a magnetic field of 1.2 tesla, and compressed at 5 tons/cm^2. The compacts are sintered for 1 hour at 1200°C in argon gas and cooled rapidly to room temperature. A post-sintering heat treatment is the final step.

The objective is to test Nd-Fe-B materials to determine if the mechanical strength is satisfactory so that the F16 wings can be self-supporting without sacrificing 15% volume for a stainless steel skin. In that case a wing moment is 15% larger and roll coils can be 15% smaller.

2.4 Improved MSBS Design

The objective is improved MSBS designs based on Phase I design improvements and Phase II experimentally confirmed improvements.

12

The Phase I MSBS design by MMI includes design improvements which reduce the costs to $21 x 10^6 compared to $30 x 10^6 for the 1984 MSBS design by MMI and compared to $90 x 10^6 for the 1982 MSBS design by GE.

Some special features of the MMI-1984 design are:

► Superconductive persistent solenoid in the suspended airplane model instead of magnetized iron.

► Permanent magnet wings instead of magnetized iron wings.

► New race-track roll coils.

The special features of the MMI-1985 design are:

► Magnetic holmium core inserts in the test model superconductive solenoid.

► Better permanent magnet material, $Nd_{15}Fe_{77}B_8$, in the wings.

► Saddle roll coils and in-line smaller diameter drag coils.

► Fiberglass epoxy structure.

Some of the improvements in the PHASE I MMI-1985 design over the 1984 MMI design were not predicted and came as a result of better permanent magnet materials for the model wings, of holmium in the model core solenoid, and of new saddle R coils.

The ampere-meters and the energy stored in the R and Y

13

coils are strongly related to the average magnetization of the wing which is a function of the permanent magnet remanent magnetization and of the amount of stainless steel support in the wing. In the Phase I design, stainless steel occupies 15% of the wing volume. In Phase II, mechanical tests of the new magnetic material determine whether or not there is need for the stainless steel support. This shows that there is a potential improvement of up to 15% for the R and Y coils.

The ampere-meters of the X and Z coils are strongly related to the model core solenoid magnetic moment. As explained in 2.3, there is a possibility of increasing the magnetic pole strength of the model core solenoid by using higher current density windings and proper optimization of winding and holmium volumes in the model core solenoid.

3. Phase II Accomplishments

3.1 Full-Scale Model Solenoid and Cryostat

3.1.1   Full-Scale Model Solenoid

The full-scale solenoid construction and test for the F16 airplane model is a major Phase II achievement. The goal is to demonstrate that a high pole strength and high magnetic moment practical solenoid can be built to commercial specifications, and become certified as available for use. All avenues to improve the model solenoid are to be judiciously incorporated. One such new improvement is the holmium core; it enhances the pole strength in return for the complication of including the holmium. The result of this experiment should be a clear recommendation as to the value of holmium vs. the obvious loss of helium volume and reduction in projected running time.

In the same vein we choose an acceptable and moderately high 30 kA/cm^2 current density goal for a standard 1.35:1 Cu:NbTi ratio conductor at 6 tesla. The logic is that a much lower current density is unattractive and a much higher current density might better await the next step. The next step could be a solenoid incorporating all of the improvements herein for higher current density.

15

3.25 (82.55mm) DIA (REF)

13.78 (350mm)(REF)

15.03 (350.96mm)(REF)

GROOVE MICARTA FOR MAGNET LEADS
AS REQUIRED. LEADS MUST BE FLUSH OR
BELOW FACE BY (AMER MAG.)
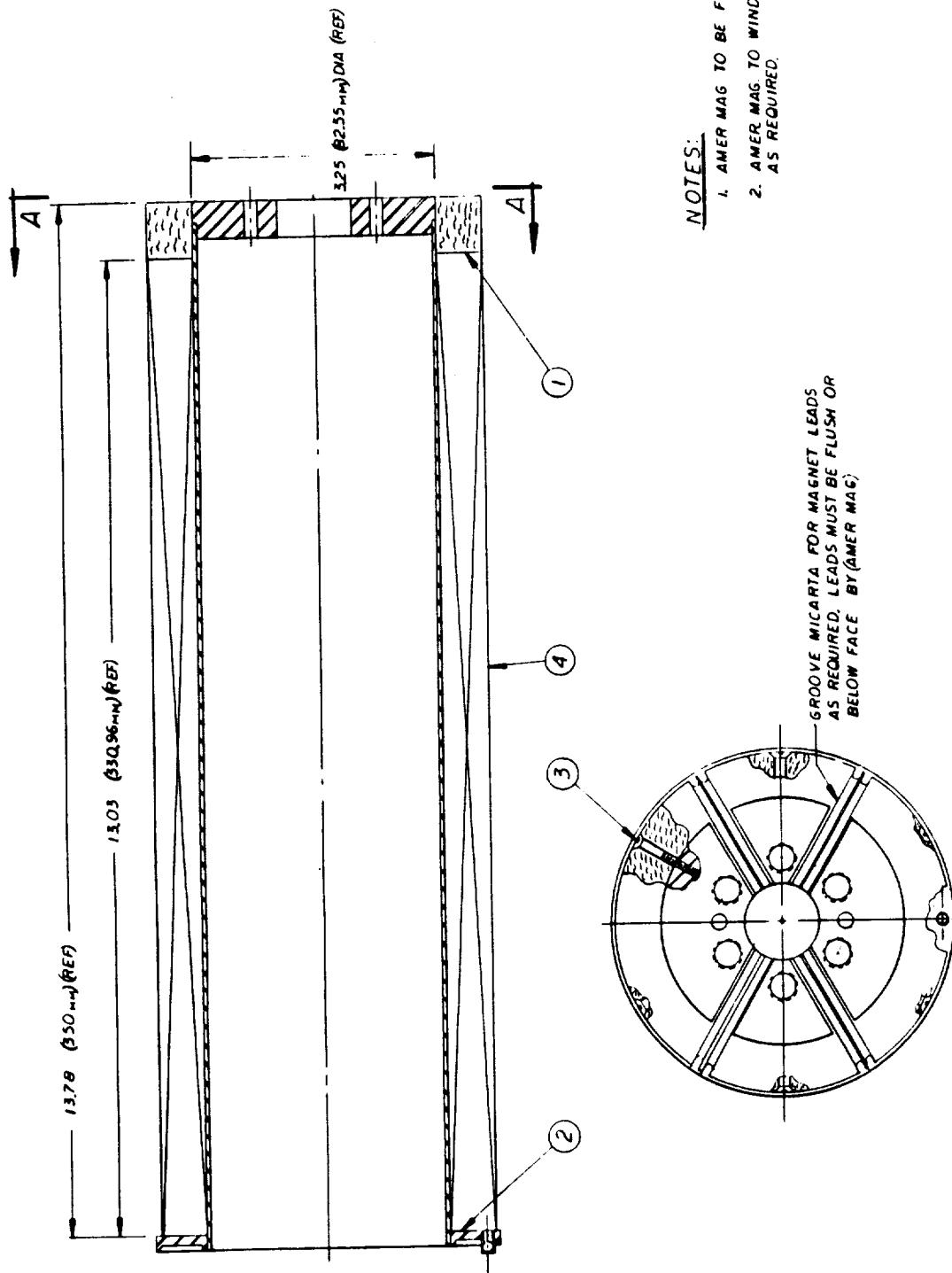
VIEW A - A

NOTES:
1. AMER MAG TO BE FURNISHED PARTS ①, ②, ③

2. AMER MAG. TO WIND COIL, ASSEMBLE AND WIRE
   AS REQUIRED.

Figure 3.1-1. Left Magnet Winding.

16

3.1.1.1 Design of the Model Solenoid

The general specifications and configuration of the model solenoid are shown in Section 2.1, Table 2.1-1, and Fig. 2.1-1. The external envelope is 30 in. (762 mm) long by 5 in. (127 mm) in diam. More details are seen in Fig. 3.1-1; the coil windings in Fig. 2.1-1 are actually two solenoids bolted together end-to-end with a substantial 0.75 in. (19 mm) thick micarta (Fig. 3.1-1) central flange on each coil. The windings are separated by 1.5 in. (38 mm) at the center. The winding window in Fig. 3.1-1 is between the 0.05 in. (1.27 mm) wall thickness mandrel, and (4), the 0.01 in. (0.25 mm) thick outer cold jacket.

Interconnections between the two halves are positioned in grooves in the center micarta flanges during assembly, view A-A, Fig. 3.1-1. The holmium cylinders mounted in the mandrel cores are 13.260 in. (336.8 mm) long, 2.30 in. (58.4 mm) ID, and 2.987 in. (75.87 mm) OD. The original holmium was 3.14 in. OD; it could be forced with difficulty into the assembly. However, as explained in Section 3.1.3, the holmium diameter is machined down to 2.987 in. in order to reduce cooldown stress on the windings.

The cooldown contractions are listed in Table 3.1-1. Good solenoids are commonly designed for NbTi/Cu conductors

17

Table 3.1-1
Thermal Contraction

Material	ΔT	ΔL/L %
NbTi	300 - 4.2 K	~ 0.175
Holmium	300 - 4.2 K	0.122
Copper	300 - 4.2 K	0.33
Stainless Steel	300 - 4.2 K	0.30
Epoxy	300 - 4.2 K	~ 1.10

potted in epoxy on stainless steel coil forms. We infer that epoxy is flexible enough and weak enough so that its contraction properties are secondary, except as a source for cracks and crack frictional motion. It is apparent that the similarity of ΔL/L between NbTi/Cu and stainless steel should lead to a low stressed winding after cooldown. In contrast, a winding on a massive piece of holmium would be strained to ~0.21% and stressed to about 100 MPa after cooldown. Some short samples of NbTi have carried rated currents up to the breaking strain of ~2%; a strain of 0.2% in itself might be acceptable. However, a permanent strain of 0.2% in the windings could eliminate or alter the training process to get highest currents.

In Fig. 3.1-2 is a detail of the current lead-in, persistent switch (7), and diode bank (3); the external plug into switch (1-2) is removed, which eliminates the lead heat leak whenever the solenoid current is carried by the

EPOXY ITEM ① INTO ITEM ②
AFTER WIRING IS COMPLETE
USE, EMERSON CUMMINGS 2850FT
EPOXY
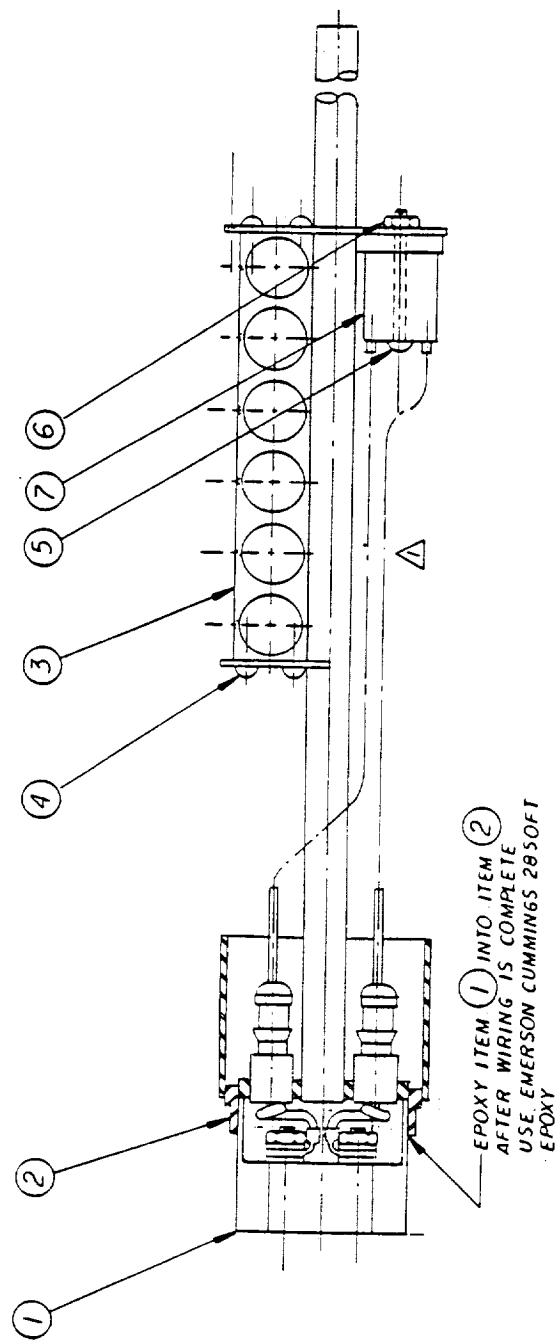
Figure 3.1-2. Current Leads and Persistent Switch

persistent switch. The electrical assembly in Fig. 3.1-2 is mounted permanently in the left solenoid to power both solenoids in series.

3.1.1.2 Holmium Procurement

The holmium core as designed in Section 3.1.1.1 was purchased at 13.260 in. (336.8 mm) long, 2.30 in. (58.4 mm) ID, and 3.14 in. (79.76 mm) OD, see Fig. 3.1-3. The Research Chemicals Co. cast the three cylinders in three graphite molds at 1461°C by using a vacuum induction melting and casting method that flows the metal smoothly into the mold. These were the largest castings made at that time in 1988. Machining was easy; care was taken to avoid ignition of the metal chips. American Magnetics machined the OD down to 2.991/2.987 in. to get a snug but low stress fit to the solenoid after cooldown.

Solenoid tests for very tight and for moderately loose fitting holmium cores are given in Section 3.1.3.2. This may be the first example of NbTi coils wound on very rigid mandrels.

3.1.1.3 Solenoid Manufacture

The solenoid manufacture is conducted according to ordinary commercial standards to demonstrate that such solenoids could be routinely available. The manufacturer, American Magnetics, was free to select the conductor, lead system, protection system and winding design details. The
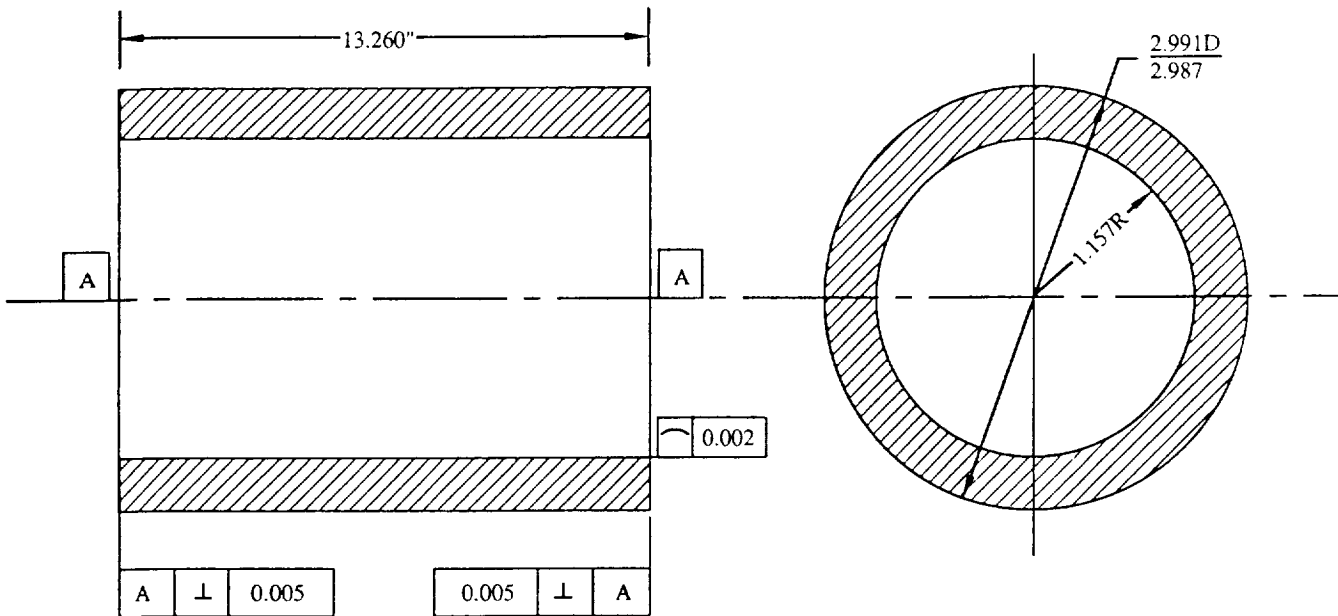
Figure 3.1-3. Holmium Magnet Core.

requirements to American Magnetics Inc. (AMI) are:

1. The solenoid is to be wound on a stainless steel
    mandrel 3.0 in. ID by 27.56 in. long to be provided
    by MMI.

2. The ampere-turns is to be 3,326,606.

3. The OD of the windings should be very close to the
    outer stainless steel helium reservoir shell, 4.630
    in.

4. The windings should be as long as possible within the winding window to increase the magnetic moment of the coil.

5. The current contacts should be breakaway contacts at one end of the magnet.

6. A persistent switch and diode protection are required.

Requirements 3 and 4 are so restrictive that there is no room on the outside of the magnet or at the ends to make reliable current contacts. For this reason AMI wound the coil in two half-coils with the current contacts being made in the center. Breaking the coil in the center also facilitates the assembly of the persistent switch and diodes which are located inside the magnet bore for lack of space to put them elsewhere. Each magnet half has current taps at the 12 and 24 layer points, breaking each magnet into 3 sections. Pairs of diodes are connected from each of the current taps to a common point (the center vacuum bore tube) for magnet protection. The persistent switch is also mounted on the center vacuum bore tube. All the diodes and the persistent switch are installed in the left-magnet half and are arranged such that after the halves are bolted together, the final solder joints can be made at the outside current lugs. High persistence joints are not needed because a small decay of the field is not considered critical. The completed magnet has 449,703 turns and thus requires 66.9 amperes operating current.

The diode protection circuit is shown in Fig. 3.1-4.
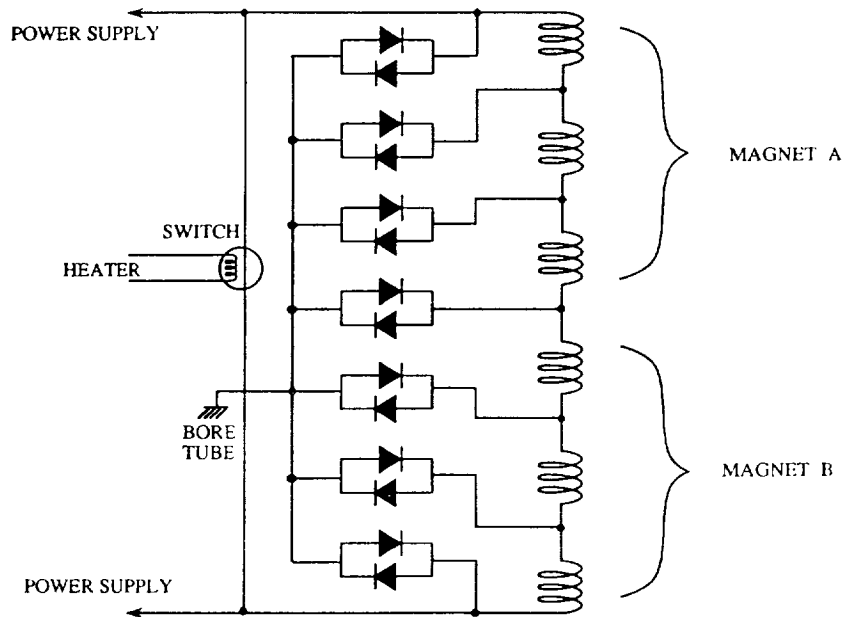
Figure 3.1-4. Diode Protection Circuit.

The principal mechanical features of this design are:

1. All internal wiring is tied down securely before assembly. This includes magnet and heater leads to the persistent switch in the lower part of Fig. 3.1-2, and the energy dump diodes attached to the top of the center tube.

2. Wires from internal circuits to the two half-solenoids are epoxied into milled grooves filled with G-10 CR insulating strips before the two mandrel halves are assembled to assure integrity of the leads.

23

3. The center flanges with alignment pins are thick enough to house six 3/8-inch diameter high strength cap screws for rigidity.

American Magnetics selected a 0.016 in. diam NbTi/Cu wire of 1.35:1 ratio Cu to NbTi. At 6T the short sample current is 120A which should be sufficient for a 6T solenoid at 60 to 70 A. The current level is somewhat arbitrary for heat leak purposes because after the persistent switch is closed the leads can be disconnected, thus removing concern about heat leak through large wires; smaller currents might be preferred if there were no disconnect.

The winding and assembly procedure is to:

1. Insulate the mandrel and install micarta end flange insulation sheets.

2. Wet wind the two solenoids to get continuous epoxy potting.

3. Mount input switch, persistent switch, and diode protection circuit within the left half-solenoid, Fig. 3.1-2.

4. Connect inter-coil leads and mount the two half-solenoids to form a single long solenoid.

5. External electrical and cryogenic connections exit from one end.

The winding and tests are conducted twice: once as described and once after the holmium cylinders are machined down to a smaller OD to prevent cooldown over-stressing the

24

windings. Table 3.1-2 lists the parameters as achieved after

winding.

<div align="center">

Table 3.1-2
Magnet Parameters

</div>

Magnet A	
(1) Winding inner diameter	3.263 in. (8.288 cm)
(2) Winding outer diameter	4.459 in. (11.326 cm)
(3) Winding length	12.904 in. (32.776 cm)
(4) Number of turns	24,849
Magnet B	
(1) Winding inner diameter	3.263 in. (8.288 cm)
(2) Winding outer diameter	4.459 in. (11.326 cm)
(3) Winding length	12.997 in. (33.012 cm)
(4) Number of turns	24,854
The parameters for the assembled system are:	
Total turns	49,703
Total ampere-turns needed	3,326,606
Current required	66.93 A
Field at the windings (no holmium)	6.16 T
Inductance (no holmium)	29 H
Persistent switch heater current	0.039 A
Magnet charge rate	4 A/min.

3.1.1.4   Solenoid Tests

The _first two_ half-solenoids are wound on mandrels with

holmium in place. The holmium cylinders are very tight fits

inside the stainless steel mandrels requiring a large pushing

force to seat in place. The preliminary tests on each mandrel

<div align="center">

25

</div>

show training to 65A. Training is not as permanent as for most coils; there is little "solenoid memory." "Solenoid memory" refers to training successive micromotions of turns to the final best locations which remain fixed, resulting in a "trained" magnet which always thereafter carries full current. The thin wall coil form might collapse a few milli-inches to rest on the heavy wall holmium cylinder during winding. Low temperature charging "might" achieve lift off at 15A, causing the first quench. After that, ordinary training of several quenches carries the current to 65A. After warming up to room temperature, the winding could again collapse onto the holmium and training would repeat again without any memory. This seems plausible.

Two sets of training currents are found. The first (highest) currents are found for undisturbed coils. The second set followed from efforts to mechanically adjust the holmium core vary widely, and are not significant. The significant results are:

$$I = 62.8 \text{ A} \qquad\qquad \pm 5\% \text{ variance}$$

$$B = 6.18 \text{ T}$$

$$J = 32,780 \text{ A/cm}^2$$

The variance refers to different runs and applies simultaneously to I, B and J.

It is seen that the contract goal of 30,000 A/cm^2 is exceeded. However, such model core solenoid magnet would always require training steps with excessive helium blow-off,

which is unacceptable. Permanent training is required.

The third half-solenoid is wound directly on the holmium core. The preliminary tests show training to 47A. The low current of 47A (60A is specified) can be due only to relative contraction of holmium vs. the winding. The previous experiment with an intervening stainless steel (S.S.) winding cylinder supplied two possible components sharing the cause for excessive training: the holmium and the S.S. cylinder. This third solenoid test isolates the unexpected training to the holmium and its small cooldown contraction.

In the final design, the magnets are wound on S.S. mandrels with holmium sized to easily slip-fit into the bore after cooldown. The two magnet halves are labeled "A" (right half) and "B" (left half). The plan is to first test each magnet half individually, second test the two halves as one complete assembly, and finally, to insert the two holmium cores for a final test. The magnet halves are tested individually at 4.2 K. In these tests, magnet A achieves 72 A and magnet B achieves 73.3 A. The magnet system is then assembled and tested as a unit. Tests are performed on four different days with the assembled magnets being warmed up to room temperature between tests.

June 24, 1988   Quench at 66 A on the first try. The second try achieved 70 A with no problem. In the persistent mode an attempt was made to pressurize the system to 5 psi (gauge).* Leaks developed that prevented pressurization, and the test was stopped.

June 28, 1988   The magnet was charged to 70 A with no transition, and then pressurized to 5 psi.* The persistent switch could not be locked in at 70 A with the system pressurized, leading to the installation of a new switch.

July 28, 1988   The first test went to 70 A without transition, and was pressurized to 5 psi. The switch was locked in and the magnet was left in the persistent mode for 20 minutes. While maintaining the pressure of 5 psi, the magnet was discharged and charged again to 70 A. The switch was locked in again, and the magnet remained in the charged condition for 1 hour without problem. After discharge, the pressure was released, and the system warmed up.

July 29, 1988   Holmium cylinders were installed in both halves of the magnet. The magnet then was charged to the desired current of 66.9 A. The switch was locked in and the system pressurized to 5 psi, and discharged and charged 5 psi pressure. The switch operated without trouble. Several cycles to 66.9 A followed without quenches.

Such performance is satisfactory and meets all requirements for commercial acceptance.

---

* 5 psi is the pressure for off-gassing after final assembly and is at 4.55 K.

3.1.2   Cryostat for Full-Scale Solenoid

3.1.2.1   Design of Cryostat for Full-Scale Solenoid

Design of the cryostat for the model core solenoid is nearly identical to the Phase I concept in Section 2.1. Supports are strengthened to cope with additional weight of the holmium core, the vent line is relocated for easier assembly, and volume displaced by holmium reduces helium capacity from 3.15 to 1.6 liters. For the loss rate of 0.16 ℓ/h, the idling time for the helium level to fall from 90% to 50% is 3 hours. Sustained idle should be possible by refilling with helium on a six-hour cycle. Holding time from 90% to 20% of capacity with a full load 10 Hz AC loss of 0.046 W is approximately 5 hours.

The concept cryostat design shown in Fig. 2.1-1 illustrates major construction details. The inner helium/magnet container consists of a 117.5 OD x 0.254 mm wall outer stainless steel cylinder, 3.18 mm thick end plates, and 57.15 OD x 1.59 mm wall inset tubes which double as cryostat support members and as magnet mounting cores.

Support of the inner shell starts with cantilever 50.8 mm OD G-11 CR epoxy-fiberglass tubes epoxied to internal end plates. Thicknesses of the two tubes are 1.27 and 1.79 mm front and rear to reflect their 70 and 95 mm moment arms. Exterior ends of the G-11 CR tubes are epoxied to support plates having a single pin at the front end and machined boss at the rear. The next support stage is from the pin/boss to

intermediate stainless steel plates by means of epoxy impregnated S-glass fiber roving. Support is continued to the warm end plates by another set of three glass fiber filament loops at each end. The intermediate stainless steel plates are attached to the copper vapor cooled shield both to support it and provide a heat intercept. Axial support of the inner shell assembly is provided by concentric G-11 CR tubes attached as shown.

Utilization of helium vent gas refrigeration is vital to thermal performance of the cryostat. This is accomplished by thermally shorting the vent line to the OFHC copper shield at both ends of the cryostat with copper wire or tabs. The front short is made just before the vent line turns toward the rear as shown in Figure 2.1-1, and the back short is made just as the vent tube emerges from the inner shell. To promote good heat exchange and reduce the possibility of convection currents or thermo-acoustic oscillation, the straight length of vent line includes a piece of thin, twisted stainless steel strip which makes helium vapor swirl as it exits the cryostat.

The outer shell is comprised of 3.18 mm thick end plates welded to a 126.2 OD x 0.711 mm thick stainless steel cylinder. The cylinder is designed for external pressure and will withstand careful handling. However, for wind tunnel loads the cryostat must either fit tightly into a mating cylinder or be supported from the ends which are structural hard points. Appropriate brackets or trunnions can be added

to each end to facilitate mounting.

Thermal design of the cryostat is dependent on the low heat leak support system and low emissivity radiation surfaces. Low support heat leak is achieved by using a combination of G-11 CR fiberglass-epoxy tubes and high strength uni-directional S-glass or Kevlar filaments. Low emissivity surfaces result from use of OFHC copper, specially coated to resist oxidation, for the shield and by gold plating the outer cylindrical surface of the stainless steel magnet containment. Gold plating reduces thermal radiation by a factor of three or four in comparison with stainless steel and requires negligible radial space. Actual emissivity of gold plated surfaces at 4.2 K range from less than 0.01 to about 0.015. Emissivity of carefully prepared OFHC copper at 70 K is between 0.015 and 0.02. With these values, radiation heat leak to the inner shell is only 2.44 mW compared to the support value of 6.71 mW. Shield heat leak is 1.28 W by radiation and 0.35 W due to supports. Vent gas refrigeration potential at 70 K is about 1.67 W.

Thermal and mechanical design calculations for the cryostat are made for the desired configuration and are to serve as a guide for subsequent preparation of fabrication drawings. For the most part, the actual and concept designs coincide but, as subsequently discussed, there are important

departures. Thermal design of the cryostat is based on the following principal elements:

- A gold-plated low emissivity inner container.

- Low emissivity copper radiation shield vapor cooled at each end.

- Lateral supports consisting of a cantilever G-11 CR tube and six fiberglass/epoxy loops at each end. The fiberglass loops are attached to shield end plates so that one set of three spans the temperature range of approximately 30 to 75 K, and the second set extends from the 75 K shield temperature to ambient. All supports are designed to hold the 45.4 kg (100 lb) cold assembly with a safety factor of four when exposed to the maximum aerodynamic loads.

- A single G-11 CR tension-compression tube for axial loads.

- Minimal heat leak through a 3.175 mm OD thin wall fill tube and 6.35 mm OD x 0.4064 mm wall vent tube.

- Zero allowance for electricals due to a thermal break and persistent switch combination.

Helium heat leak based on these assumptions is calculated as follows:

Thermal radiation	0.0025 W
Lateral supports	.0403
Axial support	.0353
Vent line (venting)	.0028
Fill line (static)	.0172
Misc.	.0131
Total	0.112 W

This is equivalent to a helium loss rate of (0.112 J/s) / (20.419 J/g) = 0.0055 g/s or 0.16 ℓ/h. Measurements given in section 3.1.3.2 present the actual results obtained.

Cryostat design drawings generally follow the conceptual design of Fig. 2.1-1. Modifications in the design reflect input from the magnet manufacturer and changes to accommodate the electrical components. The following manufacturing drawings illustrate the major features of the cryostat:

MMC - 1374
(Fig.3.1-1)

Part 2 is the stainless steel winding form furnished to American Magnetics. Not shown is a 3.18 mm Micarta ring against the end flange which is installed by American Magnetics to isolate the windings. This ring has matching helium circulation channels to those in the mandrel cylinder to provide helium circulation.

MMD - 1501
(Fig.3.1-5)

This drawing shows the complete inner assembly as built including the actual winding length of 327.8 mm (12.904 in) on each half. The support system features a re-entry cantilever G-11 tube at each end which supports a plate with three machined lugs which serve as the cold end attachment for three composite loop supports. The G-11 CR axial support tube is also identified in this drawing.

MMD - 1503
(Fig.3.1-6)

This drawing details the shield assembly and the two sets of epoxy/glass filament loop

33

supports at each end. Dacron string over wrap on the OFHC copper thermal shield is applied to create numerous cross over points. These points form soft, high resistance spacers between the shield and vacuum jacket.

The support loop arrangement shown in views A - A and B - B consists of three loops at each end which extend from lugs attached to inner cold assembly to lugs on the shield end plates. The second set of loops run from near the inner radius of the end plates to lugs machined into the inside of the two vacuum jacket end plates.

MMD - 1505
(Fig.3.1-7)

This final assembly drawing shows the cryostat as built except that the actual practical wiring is more complicated. The vent line thermal contact loop with the rear end of the shield is attempted in very limited space.

MMD - 1474
(Fig.3.1-8)

This drawing shows the magnet system operating set-up including a commercial supply dewar which is not part of the procurement. The valved flexible transfer line is designed specifically for the magnet cryostat and proves to be very convenient to use.
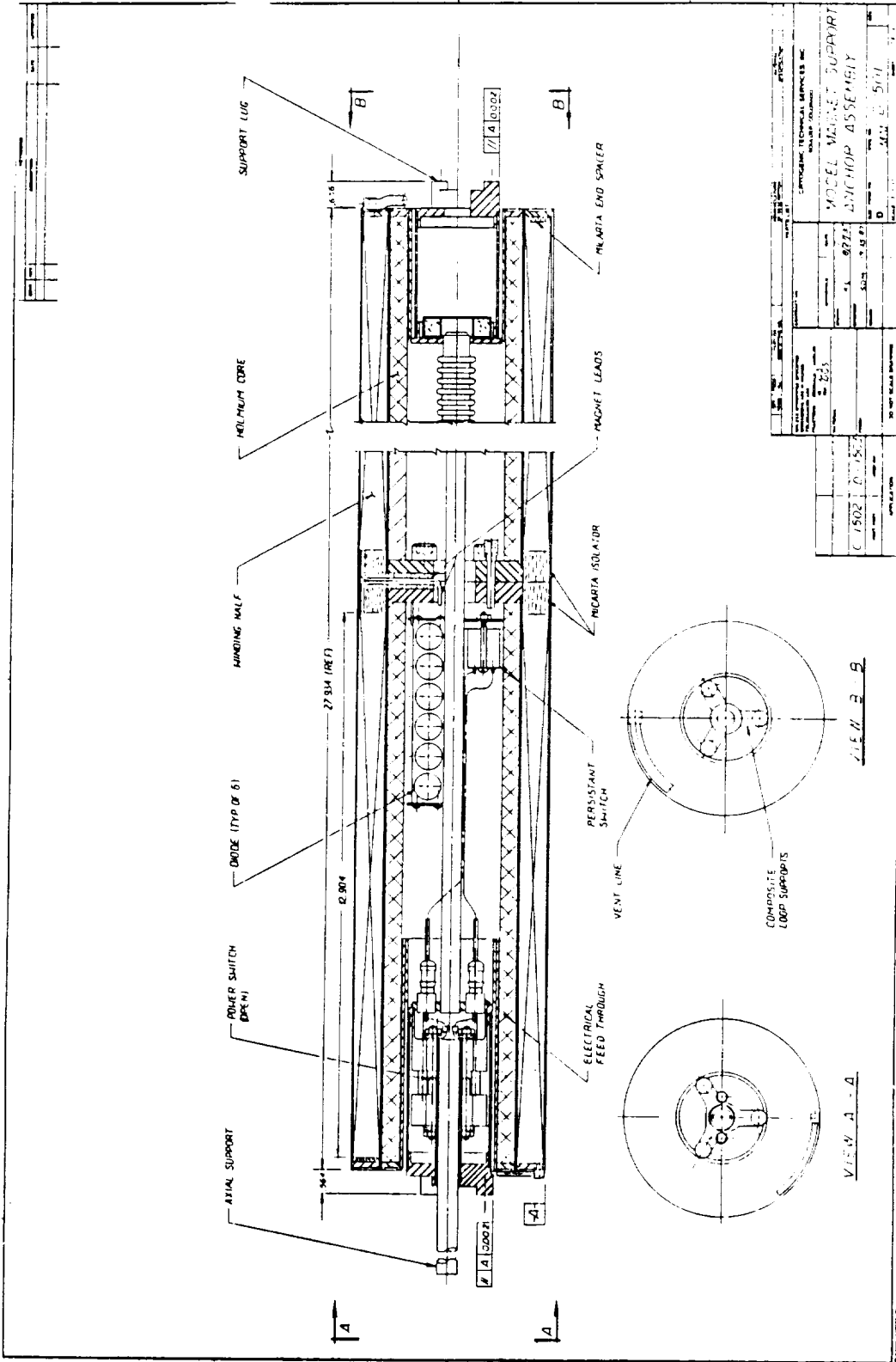
Figure 3.1-5. Model Magnet Support Anchor Assembly.
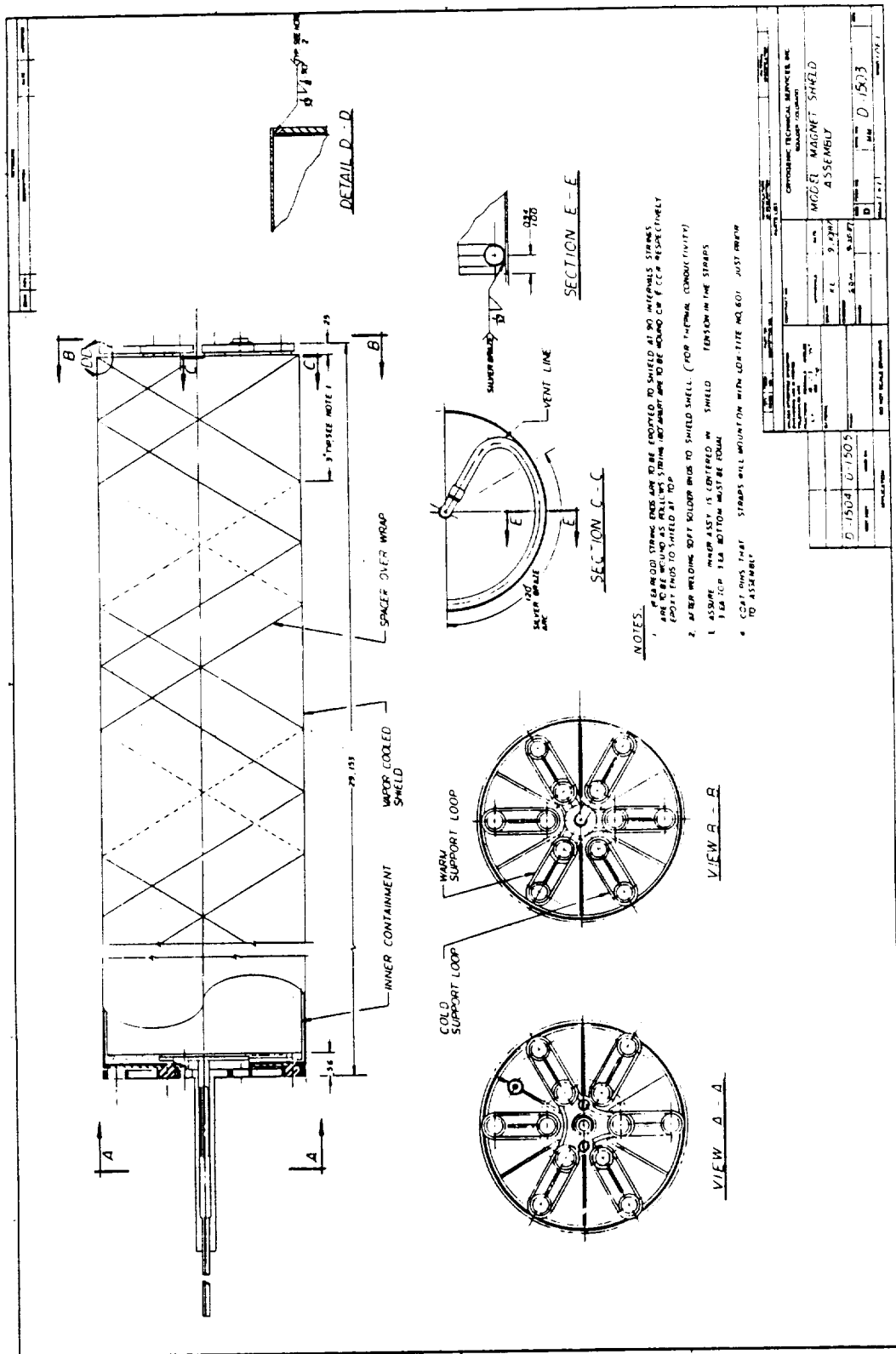
Figure 3.1-6. Model Magnet Shield Assembly.

Figure 3.1-7. Model Magnet Final Assembly.

Figure 3.1-8. Model Magnet Liquid He Transfer Assembly.

38

3.1.2.2 Cryostat Manufacture

Considerations for thin materials, close alignment, and tight spacing dominate the manufacturing process. A careful design and a high level of welding craftsmanship is required to deal with the thin materials and tight mechanical specifications. The close alignment requirements are intentionally severe in order to achieve a maximum magnetic moment.

The fabrication of the inner cold assembly, Fig. 3.1-5 is straightforward. Helium circulation channels are provided between the inner reservoir and the winding annulus in the metallic end flange region, see view A - A in Fig. 3.1-1. The helium fill path starts into the annular region, then through the above end channels, and finally into the inner reservoir. During the developmental phase of this project the helium fill scheme is changed to become a direct input into the inner reservoir.

The most difficult assembly operations are due to the tight spacing. However, these fabrication challenges are acceptable and do not require any redesign. The redesign of the next cryostat, based on the results of all experiments, would include the following key items.

1. The space between each end of the winding mandrel and the outer container would be 5 cm (increased from 2.5 cm).

2. The G-11 CR cantilevered re-entry support cylinders
    on each end would be much stiffer to limit
    deflection.

3. The coil would be wound with 20 to 30 A wire.

4. The helium annular region around the solenoid would
    be twice as wide.

5. Such redesign would simplify construction and
    repair, achieve the helium hold time of 5 hours,
    and provide a magnetic moment of 2.657×10^4 Am^2 for
    the core solenoid.

3.1.3 System Test of Solenoid and Cryostat

Successful electrical and cryogenic tests on August 3 and
4, 1989 used 200 liters of liquid helium air shipped to CDM in
Commerce City, Colorado. Several preliminary current ramps
had premature quenches in the 15-25 A range. After increasing
the helium flow-through, the quenches take place in the 60-67
A range. Each run is a slow current ramp-up at .05 to 0.1
A/sec and requires about 30 minutes for the sequence of warm-
up (quench) plus cooldown plus current ramp. The training
sequence was 63 A, 64 A, 66.9 A, 67 A, and 67 A. During all
runs, the helium flow rate and current charging rates are
varied. The solenoid meets specifications of 66.9 A.

The persistent current switching is easy to operate. The
power supply has a second built-in small power supply to heat
the persistent switch across the solenoid. By turning off the

heater power, the switch becomes superconducting and traps the existing current in the solenoid and, at the same time, is a short circuit on the leads from the solenoid power supply. A series of switching on-off steps and a long persistent hold at 60 A demonstrates that the system operates disconnected from the power supply. Thus, the system meets all specifications.

The cryostat and solenoid manufacture and tests are successfully completed and qualified per specifications. Recommendations for redesign follow in Section 3.1.4.

The following sections describe the system assembly, static tests, and dynamic tests that qualify the full-scale model for wind tunnel use.

3.1.3.1   <u>Static Tests of Solenoid in Cryostat</u>

The <u>first</u> cryostat test with installed solenoid was pumped out overnight August 29, 1988 and cooled down with liquid nitrogen, without any leaks. Only 0.2 liter of liquid nitrogen is captured and, later, only 0.2 liter of helium. Since 1.8 liters are expected, it is concluded that the liquid cryogens do not flow through the ventilation holes in the mandrel to fill the core volume. It is found that the holes at each end of the solenoid are inadvertently covered by micarta end flange spacers added during winding. Four new 3/32 in. holes are drilled in the mandrel at each end between the stainless steel flanges and the micarta winding rings without disassembling the major shells of the cryostat to

41

connect the inner and outer helium spaces. However, the liquid cryogens still do not flow to fill the core volume. The next step is to remove the holmium core and reduce the OD by 1/16 in. for a 3/16 in. axial length from the end. This forms a cylindrical helium channel. Eight V grooves 1/16" deep in the end connect the ID core volume with the OD coil volume. The mistake being corrected is that the holmium core fits too tightly in the mandrel for helium to flow from the outer to inner core volume.

In the second test in October 1988 the cryostat is set up with a keepfull on the vent to maintain a static head of liquid on the magnet and internal volume. After several tests over a period of hours it is found that for each cooldown the totalized gas flow is only about 6 cubic feet of room temperature nitrogen gas equivalent to only about 1/4 liter of liquid. Apparently the hydrostatic head of liquid nitrogen is unable to overcome the combination of flow resistance and thermal vapor generation between the holmium inside diameter and the concentric support reentry cylinder.

Subsequently, work is undertaken to move the fill connection from the bottom of the outer end flange to the inner end flange. This causes the liquid to fill against the holmium into the central reservoir. Holes communicating between the inner volume and cylindrical magnet space are enlarged for easier flow between them. The cryostat is reassembled with a new helium fill access channel in January,

42

1989.   Tests show a liquid collection of about 80% by volume of liquid nitrogen, which is satisfactory.   A vacuum leak in the cryostat inner container is repaired.   New fiberglass/epoxy support straps replace those removed for repairs.   By February 15 final reassembly is underway.

Thermal tests were performed on the magnet cryostat on March 31, 1989 at Cryolab.   Prior to filling with helium, the cryostat is cooled down and filled with liquid nitrogen.   Warm helium gas is injected into the vent line with the cryostat held vertical to ensure drainage of all liquid nitrogen and to sweep out essentially all vapor.

The first liquid helium fills and thermal tests are with the magnet vertical with the vent port at the top.   In the most representative run, the cryostat is topped off at 11:42 AM and the gas meter indicates liquid depletion shortly after 12:30 PM, for a nominal run time of 45 minutes. Totalized gas measurement reflecting retained saturated vapor is approximately 41.42 ft^3 at 60 F and 1 atm.   This is equivalent to 1.58 liter which is very close to the calculated capacity of 1.6 liter.   The average heat leak for the vertical run is about 1.334 W.

A similar thermal test with the cryostat horizontal gives the volume of gas and retained vapor at 42.39 ft^3, equivalent to a liquid volume of 1.62 liter.   Heat leak in the horizontal position is 1.85 W or about 39% higher than in the vertical position.   Apparently the deflection of supports in the

43

horizontal position causes increased thermal contact and higher heat leak. An electrical test shows continuity.

In May 1989 the cryostat was moved from Cryolab in San Luis Obispo to CDM in Commerce City, Colorado for more convenient access. X-rays of the cryostat show the following:

- The magnet and inner container are not centered in the vacuum jacket, possibly from broken or stretched supports.

- The supports are satisfactory but the magnet is off center from the vacuum jacket.

- The vapor-cooled shield makes a hard thermal contact with the inner cylinder, which renders the shield almost totally ineffective and with a large heat leak.

- The gold-plated radiative surface of the inner cylinder is in good condition.

- The surface condition of the inside of the copper radiation shield is poor.

In July 1989 the following repair parts are installed with a new assembly fixture.

- Six of the twelve end supports.

- Four new holes in each end of the magnet winding mandrel for better helium circulation.

- A new copper cylinder and new S.S. vacuum jacket.

- A new silver-plated jacket.

The electrical and thermal magnet and cryostat tests took place on August 3 and 4, 1989 at CDM in Commerce City,

44

Colorado. All tests are with the major axis of the cryostat horizontal.

Internal circulation is improved and the magnet cryostat fills readily. During thermal tests, the cryostat can be refilled in less than five minutes after running dry. During electrical tests, the magnet recovers from a 60-67 A quench and is ready for charging again in less than ten minutes. The electrical tests are reported in Section 3.1.3 above.

Rework of the cryostat to improve thermal performance is only marginally successful. The average heat leak in the horizontal position is 1.45 W compared to the previous average of 1.87 W, an improvement of 22.5%. The full to empty duration is 47 minutes compared to the earlier 36.4 minutes. Cryostat recommendations to increase the helium hold time follow in Section 3.1.4.

3.1.3.2 Dynamic Assembly Tests

Design loads for the magnet cryostat are specified as follows:

Lift (Vertical)	9790 N =	2201 lb_f
Side (Lateral)	1380 =	310
Drag (Axial)	4180 =	940

The most convenient way to impose these loads is by means of a centrifuge. Thus, a heavy steel fixture is fabricated to safely contain the cryostat for a series of mechanical tests at the maximum specified loads. Specifications for these tests are developed as discussed below.

For centrifuge testing assume that a concentrated load is

at the center of gravity, then the radius/rotational speed combination for the required force is given by

$$F = W R \omega^2/g$$

where,

F = force, lb_f
W = weight of the assembly, lb_m
g = gravity acceleration, in/s^2
R = swing radius to center of gravity, inches
ω = rotational speed, rad/s.

The above equation is used to calculate centrifuge radii and rotational speeds for the required loads and a magnet assembly weight of 95 lb.

Loading	Radius	ω	RPM
Lift	44 in	14.264 rad/s	136.21
Side	44	5.353	51.119
Drag	32.5	10.846	103.574

Different modes of loading the cryostat supports are achieved by rotating the cryostat with respect to the swing axis for lift and side forces. The cryostat and its fixture are oriented radially for the drag force test.

On August 31, 1988 the cryostat was taken to Phoenix Laboratories, Inc., Garden Grove, California. Centrifuge tests were performed at Phoenix under the direction of Mary M. Merrick, Quality Control Manager. The test results are:

Date	Time	Test Radius (inches)	G level	RPM	Axis	Duration (minutes)
08/31/88	11:59 AM	44	23	136	Lift	10 Min.
	12:53 PM	44	3.3	51	Side	10 Min.
	1:17 PM	32-1/2	9.9	104	Drag	10 Min.

There is no evidence of distress or failure during the centrifuge tests. A follow-up thermal test indicates that the vacuum level is not affected by the loads imposed. Finally, when the cryostat is later disassembled for rework, all of the supports are observed to be in good condition. Thus the supports are mechanically acceptable for their intended use.

3.1.4   Recommendations for Redesign

Despite the high boiloff values obtained, it appears that only a few significant changes need to be made to the magnet and cryostat to achieve thermal performance close to that originally predicted. Recommendations for these changes are discussed in context with the present design and magnetic characteristics.

Radial clearances between the inner container and shield and between the shield and vacuum jacket are very close in the present design. However, there is no evidence that these small clearances pose a fundamental problem provided that end support rigidity is improved. Therefore, it is possible to preserve the present magnet radius with appropriate changes in the support system. Reducing the magnet radius by 2 mm to add an extra millimeter of space on each side of the thermal shield would be helpful insurance but is not considered essential.

Length of the magnet in relation to the overall envelope length is a more serious problem than radial clearance. A

good part of the mechanical/thermal problems can be traced to the lack of space at each end. More space is needed for support clearance and attachment, for vent line contact with the shield, for efficient arrangement of electrical connections, and for shield end clearance. The amount of shortening needed requires a new design layout. However, we believe that the clearance at each end must be increased by as much as 25 mm, especially at the rear where lines, electricals, supports, and the switch actuator compete for space.

The most radical suggested change relates to the magnet windings. The present design requires 66.9 A to reach design field. With this configuration and size of components, the only feasible location for the power leads and electrical disconnect is in the vacuum space. With no cooling except for liquid helium at the cold end (a very costly solution), large copper leads and beryllium copper tapered disconnects are required. This results in the largest heat leak to the cryostat by a substantial margin. We propose that lower current windings be used. Downsizing to something on the order of 20 to 30 A would be helpful. This smaller wire could be threaded out through the vent line. Another possibility is to locate the smaller disconnect at the front end of the cryostat to provide a lengthy gas cooling path for the leads and switch actuator rod.

The support system in the present cryostat has high

resistance heat paths. However, flexibility of the main G-11 support tubes and very small clearance between the inner assembly and shield allows them to make thermal contact. A more rigid inner support configuration will maintain high thermal resistance and avoid thermal shorting. More space at the ends for support installation will contribute to improved support heat leak. Increased support tube rigidity can be achieved by using specially made high modulus material and by making the tube wall thickness slightly greater to raise its section modulus. This, plus relocation of potentially shorting surfaces will assure maintenance of the design thermal circuit with an overall heat leak only a little higher than the present design.

Cleaning up the emissive properties of the shield and inner container end pieces is primarily a function of available end space. With just a few millimeters more space at each end, it is possible to install smooth, low emissivity surfaces which will improve performance.

Finally, additional end space will permit routing the vent line so that both the front and rear of the shield can be effectively cooled by venting vapor. This will improve performance significantly.

In summary, we propose to shorten the magnet by 50 mm and reduce full field winding current to 20 to 30 A from the present 66.9 A, which requires smaller wire and more turns. These changes facilitate other modifications which will bring

down the heat leak. These improvements should bring actual performance to within 10 or 15% of that originally calculated or about 0.125 to 0.13 W resulting in a helium loss of about 0.18 to 0.25 ℓ/h.

3.2 High Current Density Solenoids

The high current density solenoid program, as explained in Section 2.2, is to produce coils with selected loaded epoxy impregnation, with the best NbTi/Cu conductor, and wound on the same winding ID as the full-scale solenoids in 3.1 for an assessment of training and reliability. The design of the high current density test solenoid, the epoxy program, the NbTi/Cu program, the test solenoid construction and the solenoid test program are described in subsequent sections.

The objectives for developing a high current density solenoid listed in Section 2.2 are to develop a better loaded epoxy for solenoid potting and a better NbTi/Cu conductor. "Better" refers to be better than commercial standard practice as used in Section 3.1, the full-scale solenoid construction and test. The final proof is to compare two solenoids wound with the same new NbTi wire, that are potted with a clear epoxy and with a loaded epoxy. The loading is high thermal conductivity ceramic SCIA, as described below.

3.2.1 Design of High Current Density Test Solenoids

There are electromagnetic and thermal design principles for a potted solenoid. The electromagnetic conditions for solenoid current density capacity are that sufficient NbTi cross-section must be present to carry the design current density in the solenoid winding window in the self-generated field at 4.2 K, the bath temperature of interest here. A simple series-wound solenoid finds its current density limited by the highest field, the field on the median plane inner turn, and by an ill-defined practical process named "training." Training refers to a thermal-electromagnetic process that results in successive charging cycles leading to successively higher current densities and higher produced fields. In general, training seems to involve two kinds of limiting events. In the first case a physical frictional movement of wire turns while increasing the current density, fields, and forces causes a small temperature rise in the NbTi which causes a quench. A "quench" refers to the rapid transition of conductor turns from superconductive to normal resistance leading to a resistive coil with a rapid current decay accompanied by internal resistive heating. Successive charging steps asymptotically reach the maximum current (I) and current density (J_c). Presumably, the wire turns finally become wedged stationary into final location and train (move) no further. The training process also occurs for epoxy potted magnets. Here the presumption is that there might be: motion

51

from inelastic epoxy reactions, epoxy micro-cracks and epoxy inter-surface friction, and even a more basic stress sensitivity by the NbTi.

In all discussions of training and ultimate magnet current density the quenching mechanisms involve a sudden temperature rise ΔT which drives the NbTi locally normal ($4.2K+ \Delta T > T_c$). The basic premise for the high current density solenoid project is that a high conductivity-high specific heat loaded epoxy should improve the cooling and internal local enthalpies and provide significantly higher quench current densities and higher model core magnetic moments.

The test coil design dimensions are half-scale on length 6-3/8 in. and full-scale on diam 3-1/2 in. compared to the solenoids in the full-scale model, Section 3.1. The coil form, Fig. 3.2-1, is divided by a center flange so that one-half can be wound with loaded epoxy and one-half with unloaded epoxy. Winding on the same mandrel ensures identical performance tests and simultaneous competitive evaluation of the two different epoxy potting systems during identical tests.

The experimental wire size is selected at 0.0152 in. diam which is comparable to the 0.0159 in. diam wire used in the full scale solenoid, Section 3.1. The experimental wire is coated with about one mil of insulation and is wound to about the same turn density. Formvar and Formvar loaded with SCIA

52

ceramic powder are the two insulations applied by multiple passes through the Formvar bath.

The principal goals of the high current density solenoid program are to achieve a more stable, high current density solenoid. The high current density comparison is between the two test coils with and without epoxy loading. Comparison with the two full-scale commercial solenoids, Section 3.1, is indirect because American Magnetics designed to meet specifications most conservatively. The coil winding is "wet winding" achieved by brushing on the epoxy and inserting porous paper insulating sheets between layers.

3.2.2   Epoxy Program

The second key objective in Section 2.2 and a goal of this research is to explore the enthalpy-stabilization that can be achieved by adding ceramic powders to Formvar and epoxy for use in "wet" winding high current density test coils. The ceramic powders here are chemically stable and have enormous specific heats below 10 K. As proposed, this program concentrates on spinel ceramics CCN (9/1) and CCN (1/0) developed by CeramPhysics, Inc. However, a third ceramic, SCIA, is introduced by CeramPhysics into this program primarily because some limited data on an SCIA + epoxy composite are available from a previous Air Force sponsored program Section A-1.

The research program here involves the fabrication of ceramic + epoxy composites by California Fine Wire Co. and the

53

measurement of specific heat, thermal conductivity, and thermal contraction at low temperatures by CeramPhysics, Inc. In addition, specific heat and magnetocaloric phenomena are measured by Ceram Physics, Inc. in intense magnetic fields at the National Magnet Laboratory.

A convenient epoxy is selected by California Fine Wire for composite fabrication (Envirotex epoxy). The previous data for SCIA composites involved a different epoxy (R12142), and the ultimate dielectric wire insulation will most probably be Formvar. Fortunately for this program, the low temperature properties of <u>all</u> <u>amorphous</u> materials are the <u>same</u> (e.g., epoxies, resins, glasses, etc.).

Although this research is based primarily on specific heat considerations, the <u>thermal conductivity</u> of the composite can also play an important role. First, it is recognized that a spectrum of thermal disturbances can arise in the NbTi wire, and the combination of wire insulation plus potting epoxy serves two complementary thermal roles: (1) to absorb thermal energy produced within the winding; and (2) to transmit this energy to the helium coolant.

At one extreme, if the volumetric specific heat of the dielectric system is large enough to absorb the maximum thermal disturbance with a minimal temperature rise, then stabilization is achieved regardless of the thermal conductivity of the dielectric system. At the other extreme, if the thermal disturbance is so large that the enthalpy of

the dielectric system is overwhelmed, then the emphasis shifts to the thermal conductivity. In fact, in this case the specific heat should be as _small_ as possible to maximize the thermal diffusivity.

There is an intermediate case for thermal disturbances shorter in time than the thermal relaxation time. In this case, the important thermal parameter is

$$\eta = \sqrt{\kappa C,}$$

where κ is the thermal conductivity and C is the volumetric specific heat of the dielectric system. In view of the parameter η, κ and C are on an equal footing in the intermediate case.

The research on composites here is aimed at a recommendation(s) for a ceramic + epoxy system that optimizes the above considerations. The full report, included as _Appendix A_, is organized into experimental methods, measurements in zero magnetic field, measurements in intense magnetic fields, data analyses, and conclusions and recommendation with the later presented below.

3.2.2.1   CONCLUSIONS AND RECOMMENDATIONS (SEE APPENDIX A)

The research results clearly favor SCIA over CCN (9/1) or CCN (1/0) spinel ceramics for additions to amorphous materials used either as dielectric insulations applied to the NbTi wire

or as potting media, for the following reasons:

1. The SCIA powders enter into composites with lower resultant porosity levels (Table A-2), thus leading to improved thermal conductivities (e.g., Fig. A-21).

2. At comparable vol.% filling ratios, the SCIA powder additions lead to smaller thermal contractions (Fig. A-9), thus resulting in improved thermal shock resistance and in a closer thermal-contraction match to copper and S.S.

3. The SCIA powder additions result in a larger enthalpy stabilization relative to 4.2 K, taking into account the H-field dependence of the specific heat (Fig. A-31).

4. Assuming that stabilization on up-ramp is more important than stabilization on down-ramp, the SCIA powder additions contribute a significant magnetization-cooling stabilization component (Table A-8). However, on down-ramp this same mechanism contributes a deleterious, reversible, de-stabilization heating effect.

5. In the intermediate case of thermal disturbances, the η-parameter for SCIA powder additions is optimal up to about 7 K.

Finally, it should be clearly understood that for a large (ΔQ) heat input which overwhelms the system it would be much better to have no SCIA powder at all, since its thermal conductivity is less than the thermal conductivity of epoxy.

3.2.3 NbTi Conductor

3.2.3.1 NbTi Wire Procurement

Teledyne Wah Chang Albany (TWCA) produced a special NbTi alloy superconductor wire with two major design objectives: to use state-of-the-art fabrication techniques to maximize the critical current density of the NbTi at B = 6T; and to maximize the current carrying capacity of the wire at 6T.

The first objective is achieved by employing high homogeneity grade Nb47 wt.% Ti alloy rod and incorporating an Nb diffusion barrier around each filament. The use of high homogeneity grade NbTi allows TWCA to take full advantage of proper heat treatments for Alpha-Ti precipitate formation [10] while the Nb diffusion barrier prevents intermetallic formation and enables uniform filament deformation [11].

The second objective is achieved by maximizing the NbTi alloy content of the wire. The copper to superconductor ratio is 0.9:1 as opposed to the 1.3:1 ratio for the commercial wire used in the full-scale solenoid, Section 3.1. Although the copper to superconductor ratio is low, it is still dynamically stable since the filaments are small and the current versus voltage traces are well defined, showing no unusual noise. The flux flow resistivity behaves in a normal fashion.

Using the stacked rod method, only one billet is designed and assembled. This billet is extruded on a 3500-ton Lombard press. The resulting rod is drawn and heat treated both at TWCA in Albany, Oregon, and Teledyne SC in Huntsville, Alabama. Final wire drawing and twisting produces a single continuous length at the final diameter of 0.0152 in (0.386 mm) with 187 filaments each 20 μm diam and a twist pitch of 0.9 in (23 mm).

Short samples of the wire carry critical currents (I_c) = 151 A at 6T, 4.2K, 10^{-14} Ω-m, giving a critical current density (J_c) of 2427 A/mm^2 in the NbTi alloy. I_c and J_c at magnetic

fields (B) from 1T to 9T are given in Table 3.2-1.

J_c for this wire might be further increased as much as 10-15% by optimizing the duration and temperature of the heat treatments and optimizing the final cold strain on the wire. Nevertheless, J_c at 6T is approximately 23% greater than the standard wire used in Section 3.1.

Table 3.2-1

TWCA NbTi Wire Tests at 4.2K, 10^{-14} Ω-m

B (T)	I_c (A)	J_c (A/mm^2)
1	478	7678
2	354	5679
3	283	4546
4	232	3720
5	191	3067
6	151	2427
7	113	1812
8	75	1206
9	38	605

3.2.3.2   NbTi Wire Insulation

The NbTi/Cu wire is coated by a 0.001 in. (25.4 microns) thick layer of Formvar insulation. The Formvar is applied in 14 passes of 1.8 μm thickness each, which sets an upper limit on the size of the dissolved SCIA ceramic powder.

The first task is to grind the SCIA powder from the 20 μm size, as received from CeramPhysics, to submicron size. The small size is needed so that the SCIA powder can pass through the Formvar dies without being filtered out. Ball mill grinding is accomplished by mixing the SCIA 20 micron diam ceramic powder with Formvar solvent GE-75024. Continuous grinding for 28 days produces a product in the 1/4 to 1/2 micron size. The product, still in a solvent mixture, is then combined with Formvar in ratio 2 lbs SCIA to 4 lbs Formvar for wire coating.

In the coating process the Formvar solvent in both ingredients disappears leaving an insulator that is about 35% by volume SCIA. The volumetric estimate is determined optically. The SCIA percentage is the maximum which could be accomodated by the Formvar coating process. Throughout the process prior to curing, the small SCIA particles remained completely in solution in the solvent and remained evenly spaced in the final product. Wet grinding the solvent is the enabling step by California Fine Wire to make SCIA coating possible.

Two lengths, each 4500 meters long, are insulated; one with Formvar and the other with SCIA loaded Formvar. The time at temperature must not heat treat the NbTi. The heated zone to cure the Formvar is 3 ft. long at 315°C to 482°C with a 1

ft warmup zone and a 1.5 ft cooldown zone to 25°C. For 14 passes the total time at temperature is 5 min. which is insignificant according to Teledyne and, in any case, is similar to the standard Formvar insulation for NbTi/Cu commercial wire.

Initially, it was planned to coat all wire with Formvar and to use the SCIA powder only in the potting epoxy. However, it is felt that the local specific heat and thermal conductivity of the insulation directly on the wire would have the most effect on short time thermal instabilities which might or might not cause quenches. Thus the SCIA powder is added to the Formvar for wire coating as well as to the epoxy for magnet wet-winding potting.

3.2.4   Solenoid Manufacture and Test

The coil form is a cylinder of the same diameter 3.5 in. as the wind tunnel model coil form in 3.1.1, so that comparisons in operations can be made. The coil form in Fig. 3.2-1 is divided by a central flange; one end will hold Formvar coated turns of NbTi-Cu wire while the other half will hold the same number of turns coated with SCIA loaded epoxy.

The coils are wound with identical 0.0159 in. wire of 0.95 to 1.0 ratio of copper to superconductor. One coil is wet wound with Envirotex epoxy; the second coil is wet wound with Envirotex epoxy saturated with SCIA powder. The coils had slightly different turns (5620 and 5874) in order to wind full layers.

60

EPOXY   SCIA-EPOXY
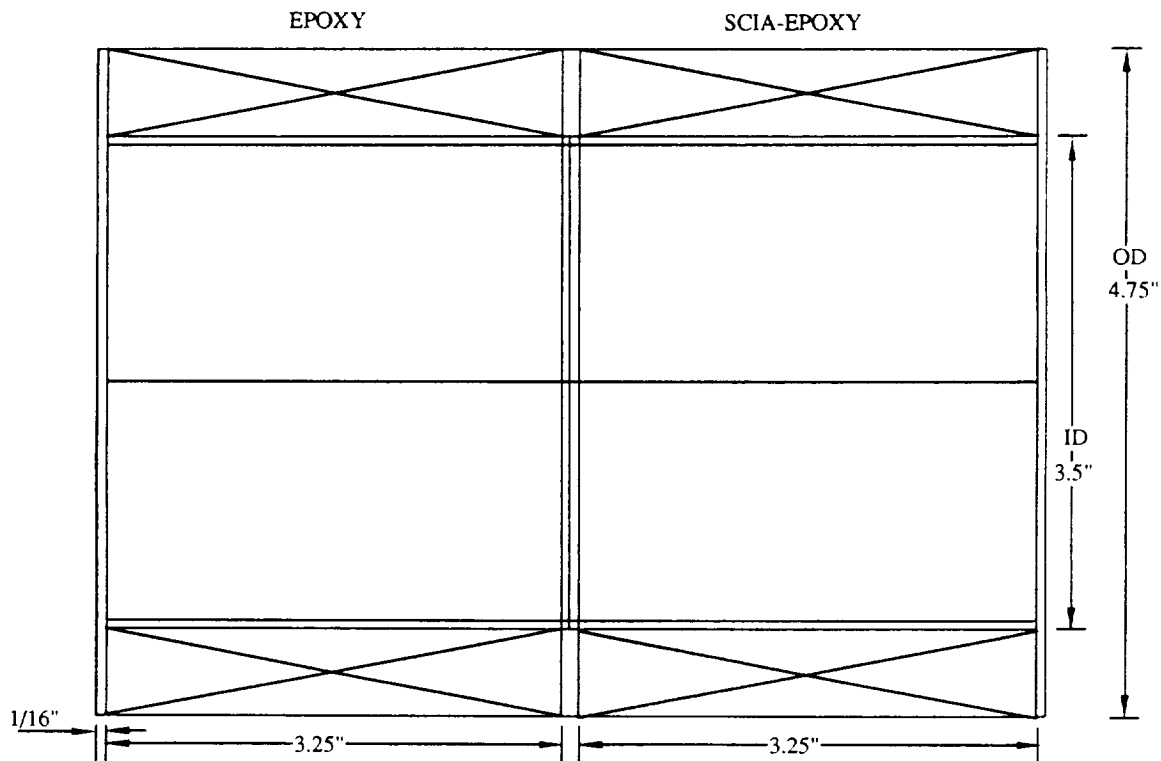
Figure 3.2-1. High Current Density Solenoids

The short sample critical current of the wire is 150 A at
6 T. Solenoids tend to carry about 50-75% critical current
after training, which is somewhat a measure of the temperature
rises during training.

The SCIA coil has 5620 turns and the epoxy coil has 5874
turns. The quench currents are I_q = 92 A ± 4 A (SCIA coil)

and I_q = 87 A ± 4 A (Epoxy coil). The quench fields at the turns, 6.05 T (SCIA) and 5.98 T (Epoxy), are identical within 1%.

Twenty training and quenching runs of the separate coils demonstrate that the quench performances of the coils are quite reproducible. The ramp time to quench is varied by applying 0.5 V to 10 V from the power supply to get charging rates of 0.25 A/sec to 5 A/sec. At the maximum charging rate the coils are powered to full field and full current in 18 sec, which is much faster than required for any potential wind tunnel use of the model coil. However, rapid charging does not cause more premature quenches. It had been hoped that rapid charging would cause more distributed heating and lower the quench current, I_q.

A cursory analysis of the quenching process is that: heat input from flux motion, eddy currents, friction, or transport current diffusion through the copper in the Cu/NbTi composite conductor, and heat absorption balance off to an allowable ΔT temperature rise above the ambient 4.2 K. The current sharing temperature for 90 A in a 6T field is T_{cs} = 5.4 K for a 150 A conductor at 4.2 K -6T. The quench measurements of I_q~ 90 A indicate that heat inputs equivalent to about ΔT ~ 1.2 K must be routinely present in both coils.

The SCIA potted coil quenches at 92 A which corresponds to a slightly higher wire temperature than for the Epoxy coil at 87 A. This difference may be only marginally meaningful

62

because of basic uncertainty in quench measurements; however, if the SCIA coil could survive rapid charging to a higher current then higher current densities with SCIA might be possible, in this case by 5.7%. It is possible to estimate the temperature difference between the two coils for quenching as follows from the linear relation of I_c vs. T at a fixed field. For this conductor we have:

$$T_o - T_c \text{ (6 tesla)} - 7K \text{ where } I_c - 0$$

$$I_c(T) - I_c(4.2K) + \frac{dI_c}{dT} (T-4.2K)$$

$$\frac{dI_c}{dT} - \frac{I_c(7K) - I_c(4.2K)}{T_o - 4.2} - -\frac{150}{2.8} - -53.6\frac{A}{K}$$

and

$$\Delta I_c - 5A$$

implies

$$\Delta T - 0.09°K \quad .$$

Thus it is possible that the Epoxy coil apparently survives heat pulses that raise the conductor temperature by ΔT ≈ 1.2K and that the SCIA coil may survive a ΔT ≈ 1.3K.

3.3 Wing Material

An MSBS magnet system must be capable of rolling the airplane model around its longitudinal axis. Roll is achieved by exerting a magnetic torque on the magnetic model wing. In this design the wings are fabricated from permanent magnet

material, $Nd_2Fe_{14}B$. The mechanical bending strength of the wing at ambient and liquid nitrogen temperatures determines if the wing is self-supporting or must be supported by an extra stainless steel skin as shown in Fig. 3.3-1. A steel skin is undesirable because it occupies space that could have been magnetic material. The purpose of this test is to measure the ultimate bending strength of the wing magnet material.
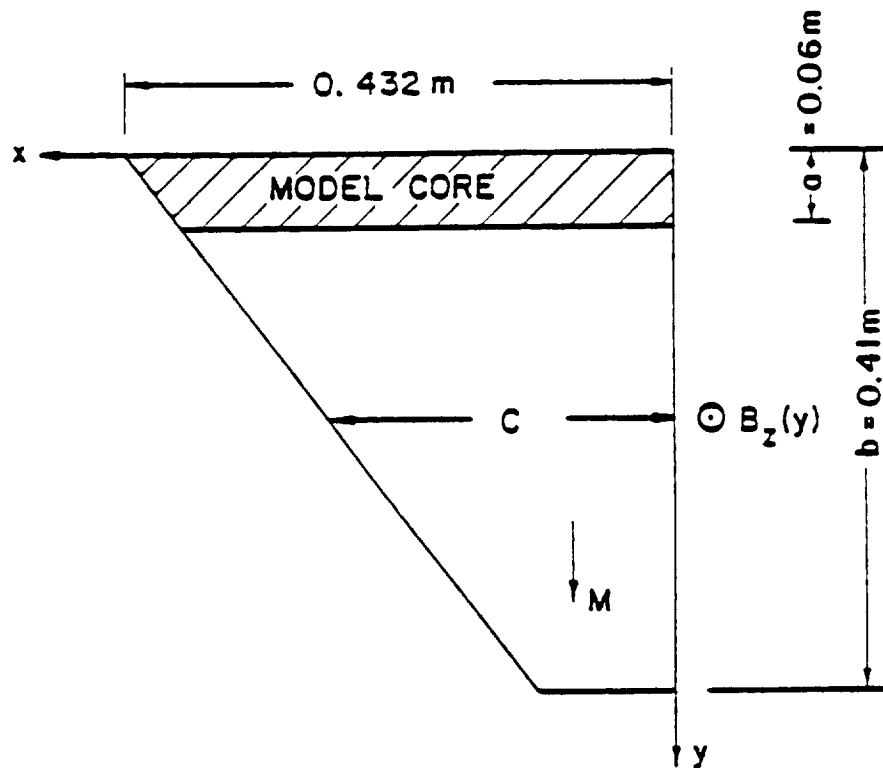
Figure 3.3-1a. F16 Fighter Wing.

NACA 64A204 AIRFOIL SECTION
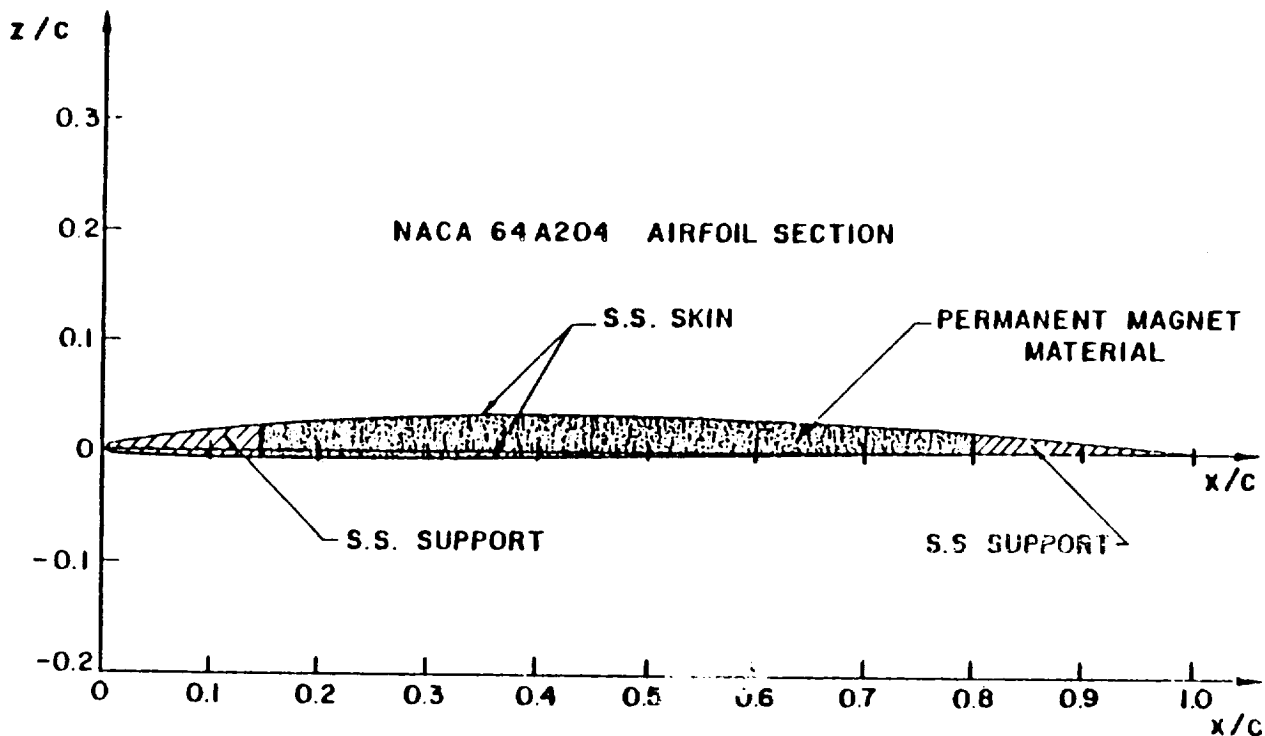
Figure 3.3-1b. Wing Cross-Sectional Area at any Chord C
Showing Stainless Steel Support, Skin, and Permanent
Magnet Material

3.3.1   Experiment Design

A three-point load test fixture, shown in Fig. 3.3-2, is used with a hydraulic testing machine. The load is measured with a calibrated load cell. A continuous flow of liquid nitrogen keeps the sample immersed in LN_2 during the low temperature test.

For the low temperature test, the sample in the test fixture is held in place with adhesive tape inside the empty

3 Point Loading Apparatus

Use stainless steel
cantilever use beryllium copper

End View

0.850"

load
0.375"
rod

support
0.375"
rods

Side View

Screws

Cantilever
beams

Top loading rod

Screw

3/8" dia. Specimen

0.170"

0.350"

0.385"

0.730"

1.00"

support rods

1.460"

0.938"

1.835"

0.455"

3.375"

Top View

0.25" hole

0.385"
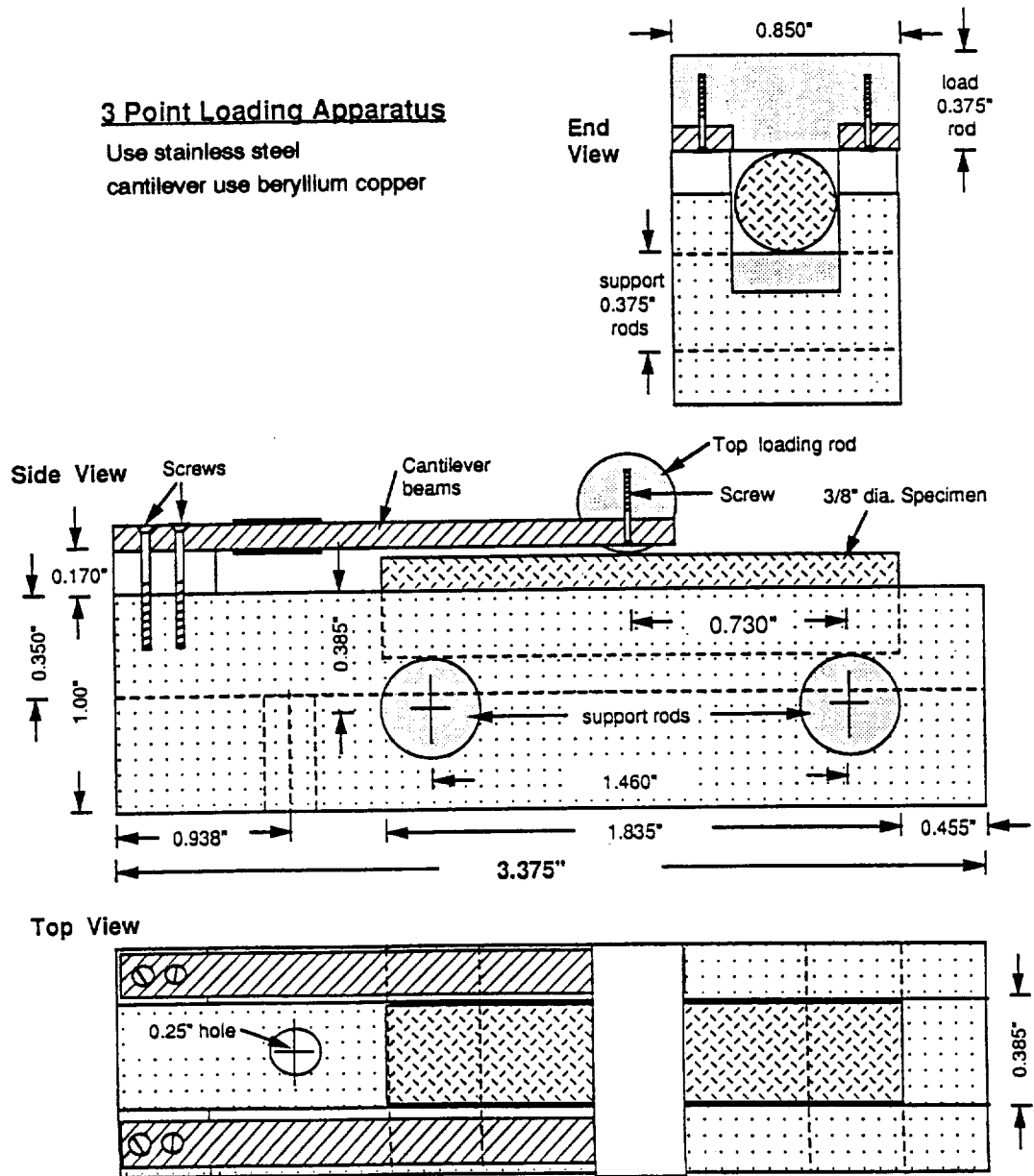
Figure 3.3-2. 3 Point Loading Flexure Apparatus.

nitrogen container. The crosshead is lowered gradually until
the loading cylinder touches the specimen and loads the
specimen to about 15-20 lb. At this point LN_2 is transferred
to the dewar. Once the liquid covers the specimen completely,
load is gradually increased until failure. The same procedure
is followed at ambient temperature without the nitrogen.

3.3.2   Neomax-35 Samples

$Nd_2Fe_{14}B$ material is available in various shapes and
dimensions from Sumitomo Special Metals Co. under the
commercial name Neomax. It is available in both magnetized
and non-magnetized states. The samples are 0.375" diam x
1.375" long rods with aspect ratio (L/D) = 3.93. Although
this is less than the recommended aspect ratio for flexure
testing, it was the closest commercial size available in the
U.S. At this aspect ratio the shear deformation is important.
However, because there is no need to measure the material
modulus, the shear effect is neglected. Physical and
mechanical properties of Neomax are listed in Table 3.3-1.
Magnetic properties of Neomax as tested by the vendor are
shown in Fig. 3.3-3.

Table 3.3-1

**Physical and Mechanical Properties of the
Neomax Wing Material**

Density (g/cm^3)	7.4
Electrical resistivity ($\mu\Omega$cm)	144
Vickers hardness (H$_v$)	600
Flexural strength (MPa)	250

Coefficient of thermal expansion
  Parallel (10^{-6}/K)
  Normal (10^{-6}/K)
	5.8
	-1.3

Specific heat (cal/kgK)	120
Thermal conductivity (cal/mK)	7700
Young's modulus (GPa)	160
Rigidity (GPa)	64
Poisson's ratio (υ)	0.24

3.3.3   Test

Three specimens are tested to failure in liquid nitrogen
and one is tested to failure at ambient temperature and
compiled in Table 3.3-2. The ambient temperature bending
strength is in good agreement with the typical material
strength quoted by the manufacturer. The average ultimate
strength at LN$_2$ is 50% higher than the room temperature
strength. However, there is no difference in the typical
brittle failure mode at the two temperatures. Tension cracks

NEOMAX-35 減磁特性曲線
(Demagnetization Curve)

向先 (User)
品名 (Item)

No.	寸法(Dimensions) (mm)	Br (kG)	Hc (kOe)	(BH)max (MGO)	iHc (kOe)	HK (kOe)
438		12.30	11.21	34.8	14.83	11.95

単位換算 (Conversion Factors)
B : 1 (kG)=0.1(Tesla)
H : 1 (Oe)=79.6(A/m)
(BH) : 1 (MGO)=7.96kJ/m³

測定 (Date) 62年 09月 25日
測定温度 (Temperature) 21.0(℃)
備考 (Memo)

住友特殊金属株式会社 技術開発部
SUMITOMO SPECIAL METALS CO.,LTD.

62.11-28

−H (kOe)

Performance Coefficient

エネルギー積 Bd·Hd (MGO)
[Energy Product]
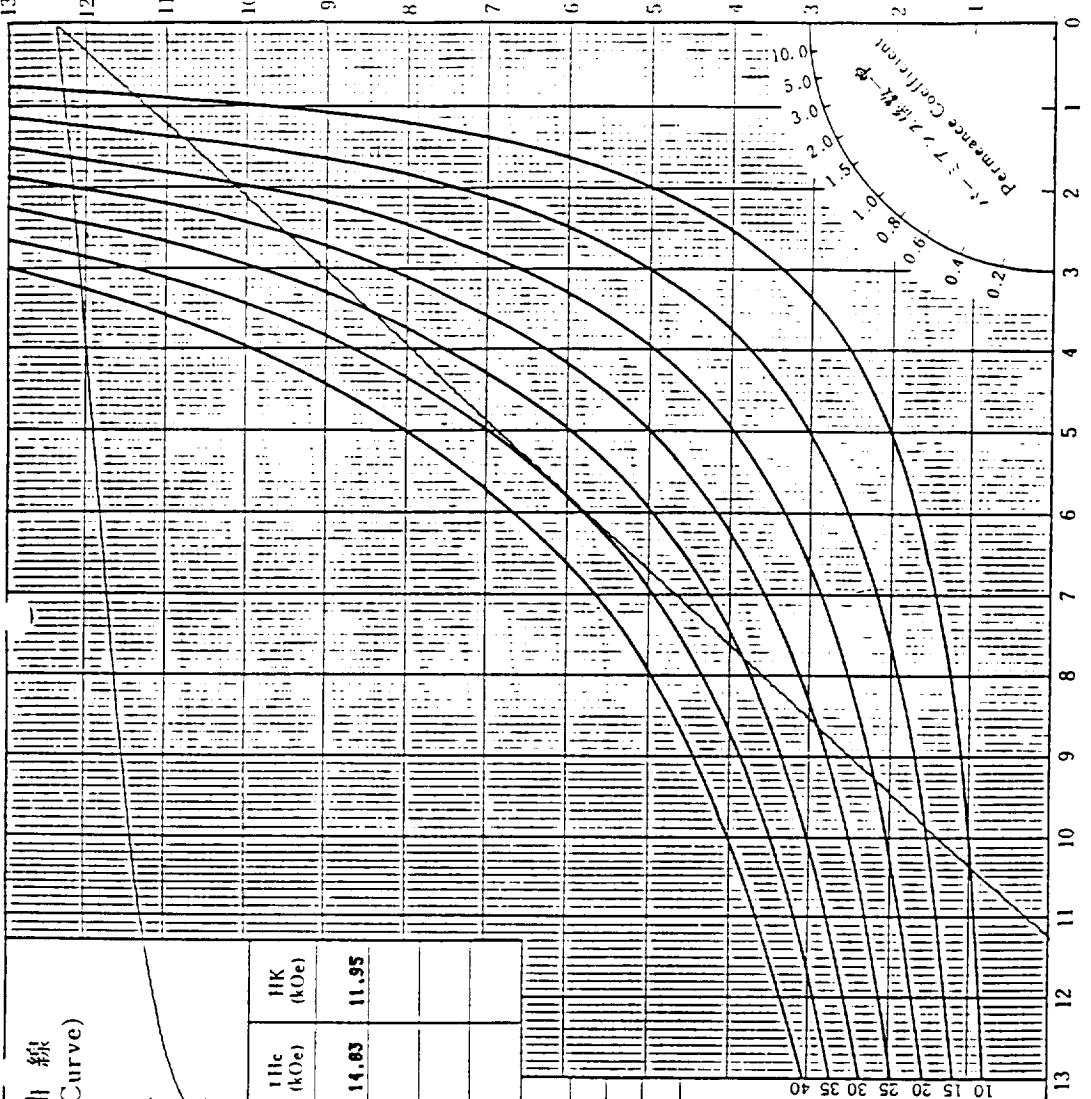
Figure 3.3-3. Magnetic Properties of the Tested NEOMAX-35 (Nd Fe B Material)

69

are initiated in the most stressed fibers and then propagate perpendicular to the sample axis.

Table 3.3-2

**Ultimate Bending Strength of NEOMAX-35
at 300 and 77K**

Sample #1 at 77K	412 MPa
Sample #2 at 77K	417 MPa
Sample #3 at 77K	368 MPa
Average strength at 77K	397 MPa
Sample #4 at 300K	264 MPa

The wing material is strong enough to be self-supporting. The Neomax can fully occupy the wing volume. Therefore, the wing can provide 15% higher volume magnetization than used in the MMI-1985 design of the wind tunnel MSBS.

3.4 MSBS Redesign

3.4.1 Background

The 1984 [2] and 1985 [3] MSBS designs by MMI include design improvements which reduce the costs to less than 25% of the earliest estimates [1]. The major improvements for the 1984 system, sketched in Fig. 3.4-1 are:

▸ A 70 cm long potted persistent superconducting solenoidal coil, 11.5 cm O.D., and 6.1 tesla is the model core. A superconducting coil produces higher

DIMENSIONS (m)	
A	0.643 r
B	1.248 r
C	0.400
D	0.715 r
E	1.352 r
F	1.25
G	0.650
H	1.025
J	4.000
K	0.400
L	1.750
M	0.400
N	2.300
P	3.700
Q	0.400
R	1.301
S	1.410
T	1.970
X	0.300

TOP VIEW

DRAG
Y GRADIENT
ROLL
Z GRADIENT

DRAG

RACE TRACK (Roll)

FRONT VIEW
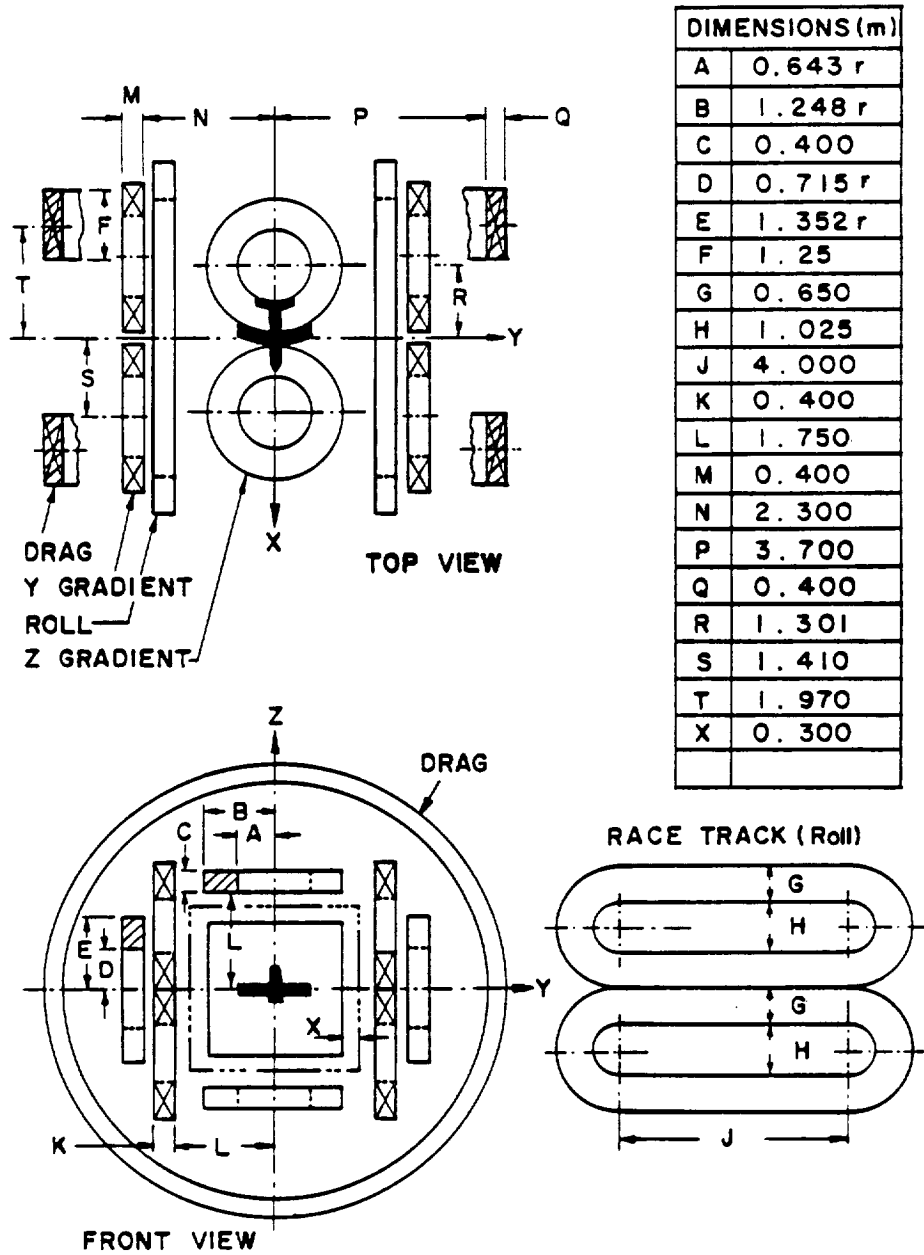
Figure 3.4-1.   1984 MSBS Magnet System.

71

magnetic moments and pole strengths than a magnetized iron core or a permanent magnet core.

- ▸ The model wings contain permanent magnets that occupy 85% of the wing volume; 15% of the wing volume is high strength stainless steel.

- ▸ Z and Y gradient coils in Fig. 3.4-1 are symmetric arrays of four bipolar solenoid to control and manipulate the model. The superconductor composite-conductor for all coils is an 11-kA low-loss cryostable conductor.

- ▸ The drag coils to counterbalance wind drag forces are large diameter solenoids.

- ▸ The roll R coils are four race-track coils optimized for minimum ampere-meters.

The 1985 MSBS design (Fig. 3.4-2) added four major improvements:

1. A holmium coil mandrel in the suspended model to increase the core pole tip magnetic moment by 18.7% from 3.75×10^4 Am to 4.45×10^4 Am.

2. A new permanent magnet material $Nd_{15}Fe_{77}B_8$ in the suspended model wings which reduces the external roll magnet size by about 25%.

3. New roll and drag coils shown in Fig. 3.4-2 for a more economical and compact design.

4. Fiberglass-epoxy slabs as the principal structure to reduce ac losses.

72
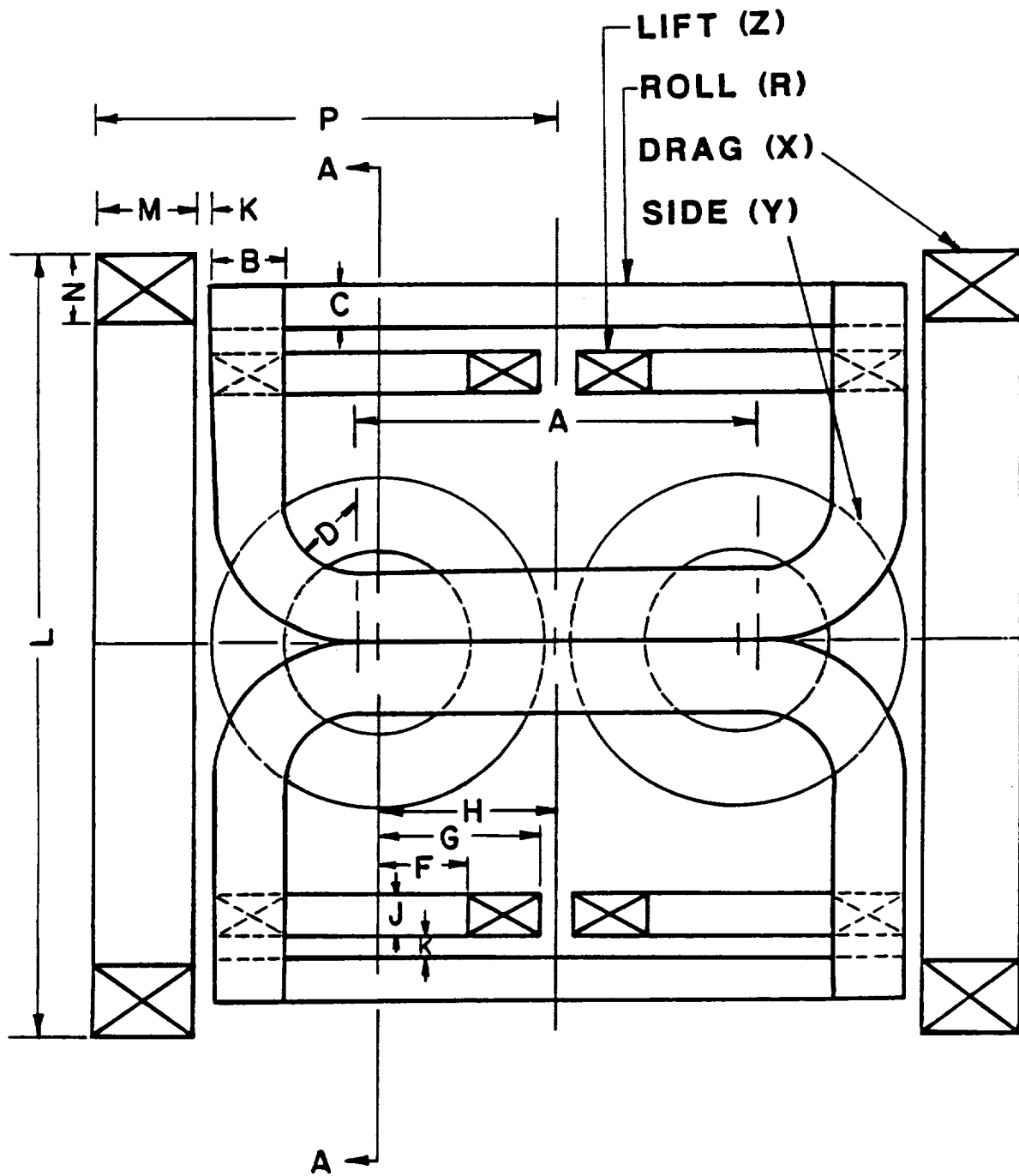
Figure 3.4-2a.   1985 MSBS Magnet System (Side View)

DIMENSIONS (m)	
A	2.800
B	0.500
C	0.300
D	0.500
E	1.200
F	0.644
G	1.153
H	1.250
J	0.300
K	0.152
L	5.514
M	0.700
N	0.500
P	3.252
Q	2.505
R	1.005
S	1.219
T	0.305
X	0.076
Y	1.753
Z	2.205

VIEW A-A
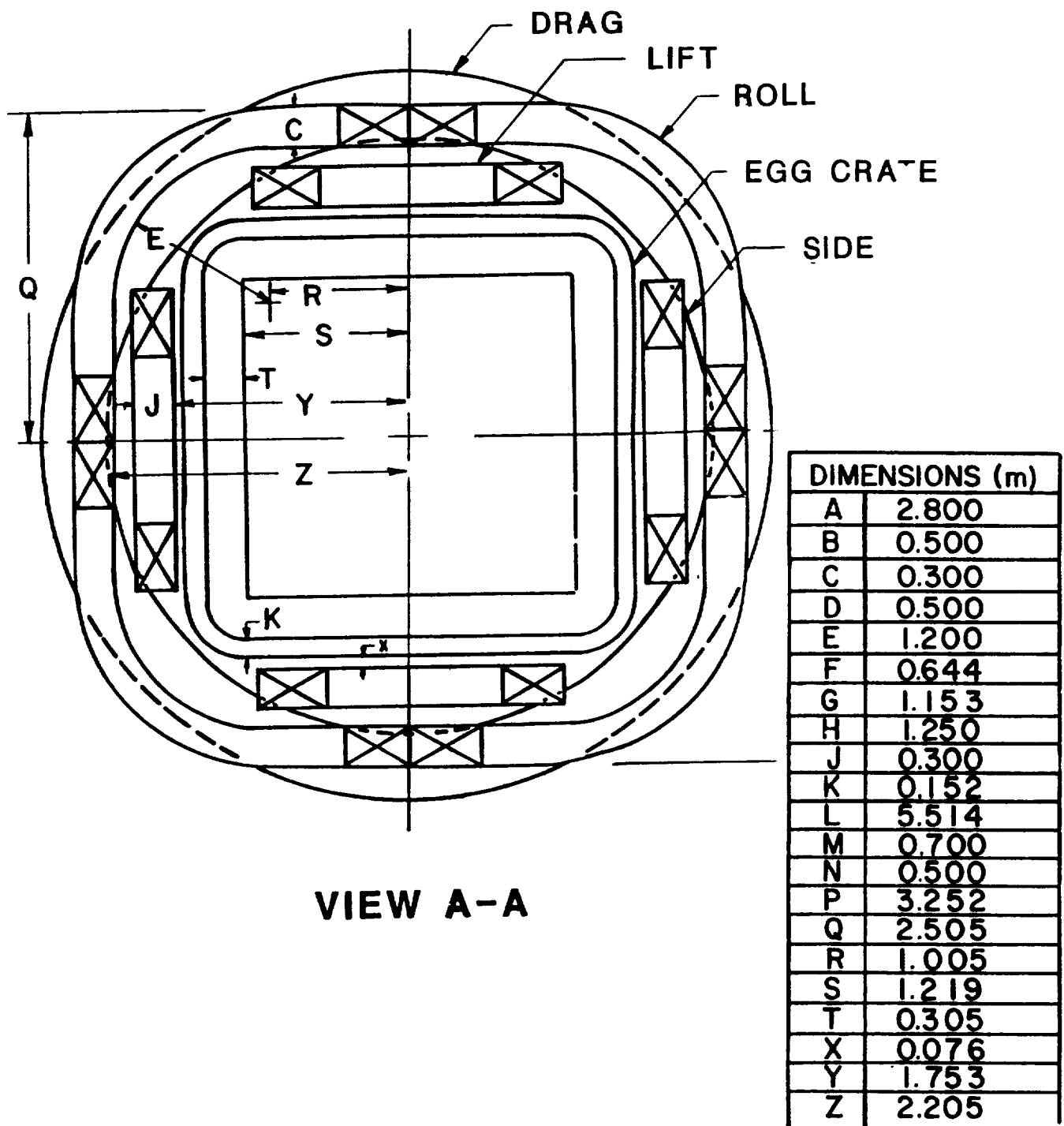
Figure 3.4-2b.   1985 MSBS Magnet System (Front View).

74

These four improvements reduced the ampere-meters and energy stored in all 14 external magnets as shown in Table 3.4-1.

3.4.2   1989 MSBS Design

In 1989 further improvements are based on tests of a full-size superconductive solenoid model coil; tests of wing materials; and with design improvements. These improvements yield 30% ampere-meter savings over the 1985 MSBS design. The 1989 MSBS design changes are:

1. Elimination of stainless steel support in the wings, which occupied 15% of the wing volume. Mechanical tests of wing materials show that the Neomax is strong enough to be self supporting to withstand maximum magnetic and lift forces.

2. The tested model core solenoid achieves 92% of the projected magnetic moment assumed in 1985.

3. Smaller roll R coils result from the 100% volume of magnetic material in the wing and allow a more optimum rearrangement (see Fig. 3.4-3).

The 1989 improvements in ampere-meters and energy stored are seen in Table 3.4-1.

Table 3.4-1

Madison Magnetics MSBS 1984, 1985 and 1989 Designs

COILS	X	Y	Z	R	TOTAL	%
1984 Design						
Ampere-meters (MAm)	362	100*	86	207	755	100
Energy Stored (MJ)	656	60	50	140	906	100
1985 Design						
Ampere-meters (MAm)	172	71**	71	154	468	62
Energy Stored (MJ)	216	38	38	116	408	45
1989 Design						
Ampere-meters (MAm)	106	53	74	108	341	45
Energy Stored (MJ)	93	25	44	58	220	25

* The Y coils in the 1984 design are recalculated for this table to correct an earlier error.
** Actual ampere-meters needed for Y coils are 63 MAm. For simplicity of design and to have a complete symmetry, the Y coils are sized the same as the Z coils.

The ampere-meters of conductor in the 1989 design decrease to 45% and the stored energy decreases to 25%, with comparable system savings as shown in Table 3.4-1.

3.4.3   Magnetic Properties of the Model Coil

The model coil solenoid with a holmium core has been constructed and tested, as explained in Section 3.1.1. The achieved magnetic moments of the winding and the holmium (67.36 cm long cylinder) are shown in Table 3.4-2. The achieved magnetic moment is 92% of the original target specification, which was 3.115×10^4 Am^2, and it is
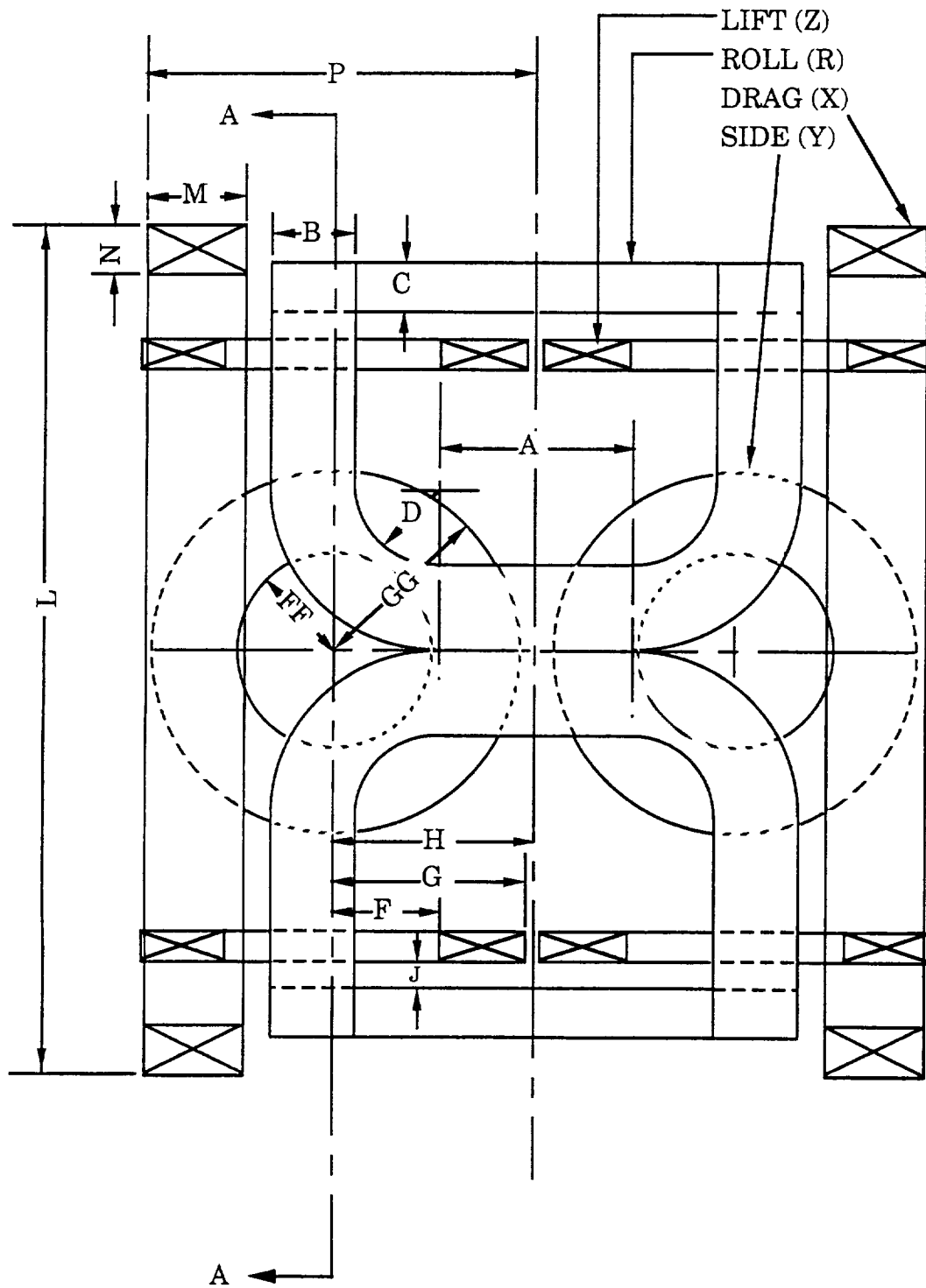
Figure 3.4-3a. 1989 MSBS Magnet System (side view).

VIEW A-A

DIMENSIONS(M)	
A	1.200
B	0.500
C	0.300
D	0.500
E	1.200
F	0.650
FF	0.600
G	1.175
GG	1.100
H	1.200
J	0.180
JJ	0.120
K	0.152
L	5.200
M	0.600
N	0.300
P	2.352
Q	2.385
R	1.005
S	1.219
T	0.305
X	0.076
Y	1.753
Z	2.025
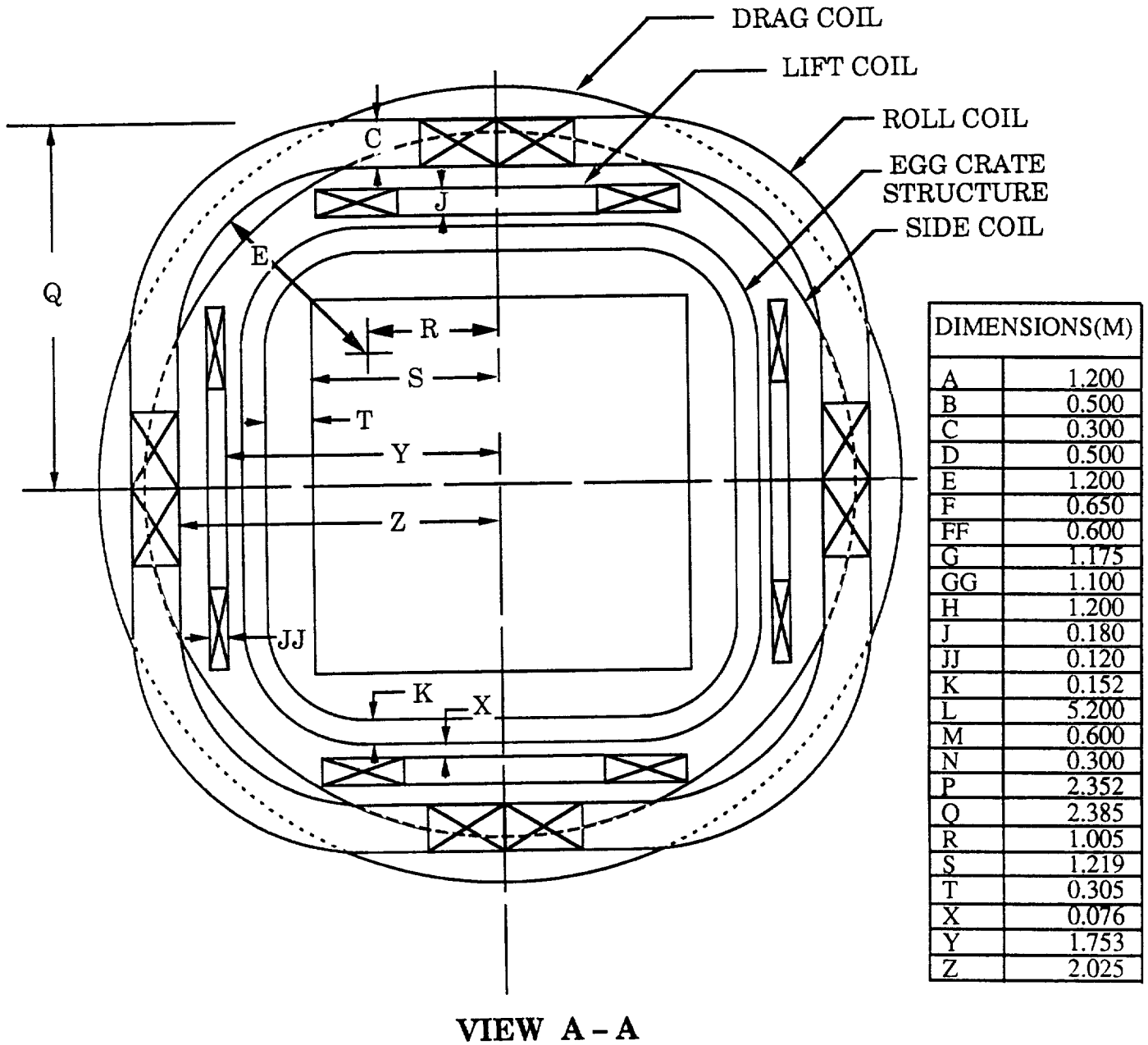
Figure 3.4-3b. 1989 MSBS Magnet System (Front View).

78

satisfactory since the target specification was based on a challenging compactness of the cryogenic system.

Table 3.4-2

Model Solenoid Data

	Ri (cm)	Ro (cm)	No. of Turns	I (A)	Magnetic Moment (Am)
Winding	4.144	5.663	49,703	66.9	2.53×10^4
Holmium	2.939	3.793	---	---	0.358×10^4
Total					2.888×10^4

A holmium core increases the total coil magnetic moment. Holmium has superior magnetic properties at 4.2 K with a saturation magnetic moment of 3.9 tesla; see Table 3.4-3 for magnetization of holmium at 4.2 K [5,6].

Table 3.4-3

Holmium Magnetization vs. Applied Field at 4.2 K

Magnet- ization Force (T)	0	0.1	0.52	1.0	1.5	2.5	3.5	4.5	6.5
Magnet- ization (T)	0	1.6	2.48	2.9	2.98	3.12	3.25	3.35	3.7

Eddy current losses in the model coil are mainly
hysteresis losses in the superconductor filaments. For two
micron filaments, the expected hysteresis loss is 0.046 watt
(4.6×10^{-3} J/cycle) with $\pm$ 0.1% field variation at 10 Hz for
all X, Y, Z and R coils at full current. The holmium mandrel
resistivity of 3×10^{-8} Ω-m at 4.2 K results in eddy current
losses of about 5.1×10^{-4} watts under the same 10 Hz current
control conditions; this is two orders of magnitude less than
the superconductor hysteresis loss.

3.4.4   Wing Permanent Magnet Material

Permanent magnet material $Nd_2Fe_{14}B$ is planned for the
wings [8,9]. The magnetic properties of some commercial
alloys are listed in Table 3.4-4.

Table 3.4-4

Magnetic Properties of $Nd_2Fe_{14}B$ Magnetic Material*

	M_r (T)	H_t (T)	(BH)max (kJ/m^3)	Temp. Coeff. of B_r (20-140°C) (%/K)
NEOMAX-37	1.24	1.18	288	-0.12
NEOMAX-35H	1.21	1.16	272	-0.12
NEOMAX-32H	1.16	1.11	248	-0.12

*Data obtained from Sumitomo Special Metals Co.

As shown in Fig. 3.4-4, M_r (residual magnetism) and H_c
(demagnetization critical field) are large. M_r stays well
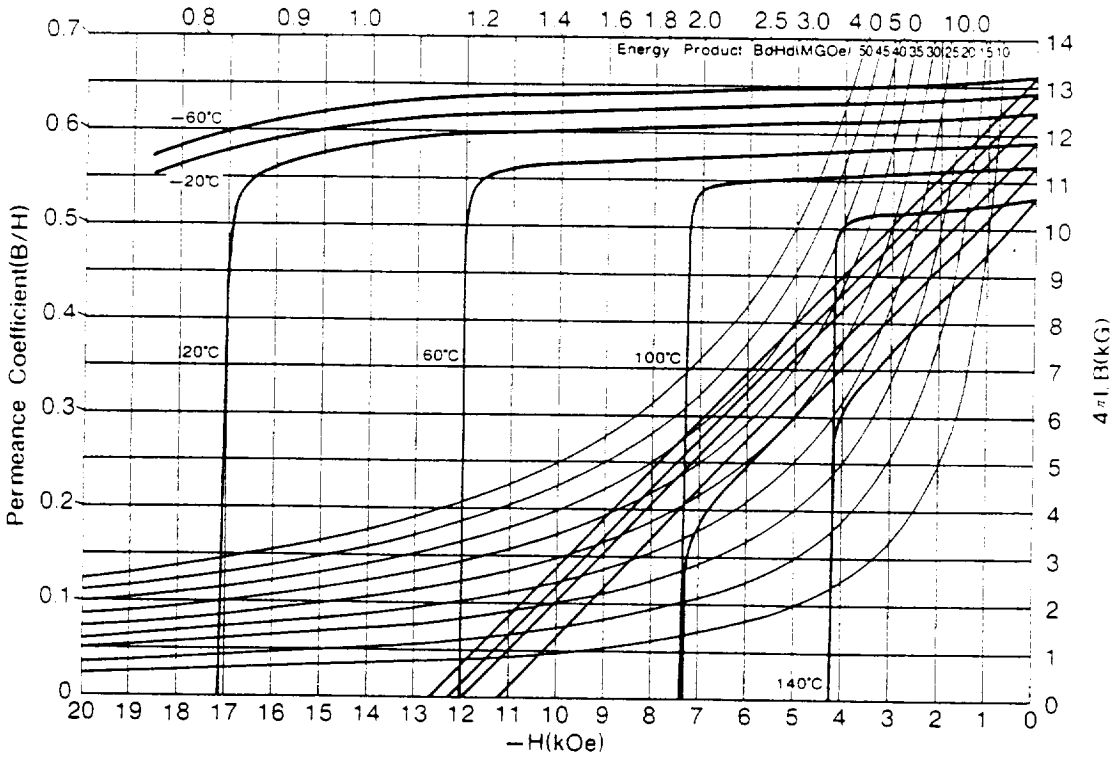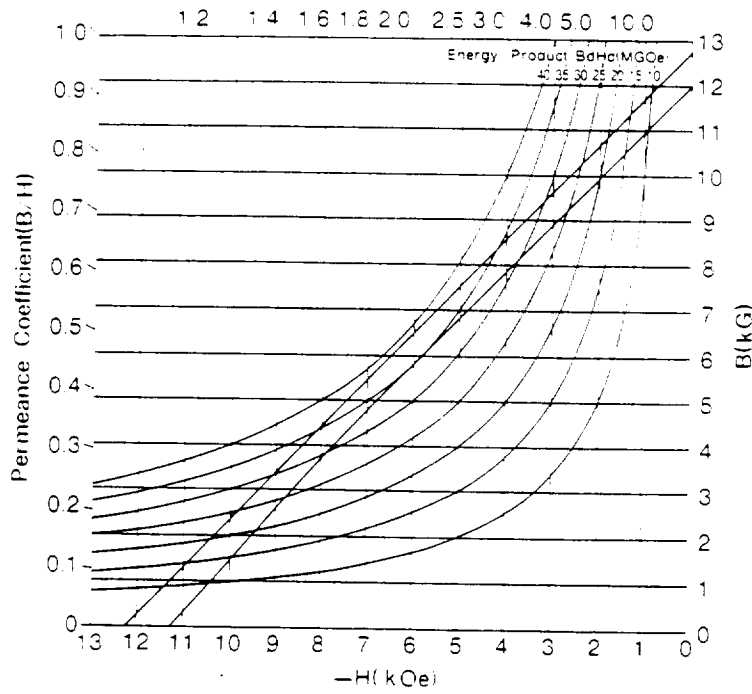
Figure 3.4-4. Demagnetization curve of NEOMAX-37. Data obtained from Sumitomo Special Metals Company.

81

above 1.2 tesla for most of the demagnetizing field and well over 1.15 up to H_c = 9.60 kA/m (1.21 tesla).

Elimination of the stainless steel skin support used from the 1985 MSBS study increases the permanent magnet wing volume to 100%. A 100% wing volume and M_r = 1.2 instead of 1.15 reduces the needed B_{zr} from the R coil at the wing tips to 0.193 T from 0.24 T, which is a reduction of 20% in R coil ampere-meters. Mathematical relations between the roll field required at the wing tips and the average magnetization are given in Appendix B of ref. [3] [MMI 1985].

3.4.5   Magnet System Design

3.4.5.1   Magnetic Field Requirements

Maximum external field requirements at the model pole tips during maximum pitch and yaw are listed in Table 3.4-5 for the above improvements in the model magnet and in the wing magnetic moment. The fields determine the size of the 14 external magnets. Appendix C of ref. [2] lists the force and torque requirements and their relation to the field from external magnets.

Table 3.4-5

Field Requirements* in Tesla at Model Coil Pole Tips for 1989 Study

	LIFT	LATERAL	DRAG	ROLL
Field Component*	B_z	B_y	B_x	B_{ZR}
Field Location**	$\alpha = 30°$ $\beta = 10°$	$\alpha = 30°$ $\beta = 10°$	$\alpha = 30°$ $\beta = 10°$	$\Phi = 0$ zero roll
Field Required to Produce Force	0.1186	0.0167	0.0510	
Field Required to Produce Torque	0.0167	0.0048	--	0.193
Total Field	0.135	0.0215	0.510	0.193
Margin for Control	2%	2%	2%	2%
Total Field Required	0.138	0.0219	0.052	0.196

*Fields B_x, B_y, B_z and B_{ZR} are fields required to produce maximum forces and torques at maximum angles of pitch, yaw and roll. These fields are produced by all four coil systems collectively.

**α is the pitch angle, β is the yaw angle, and Φ is the roll angle.

3.4.5.2   Cross Coupling

From the cross coupling relations discussed in ref. [3], the required B_{xo} , B_{yo} , B_{zo} , B_{ZR} , all at zero pitch, yaw, and roll angles are calculated and listed in Table 3.4-6. These are the maximum values of fields that can be used to design the X, Y, Z and R coils independently.

Table 3.4-6

**X, Y, Z and R Coil Fields (T) at Zero Angle of Pitch,
Yaw and Roll for the 1989 MSBS Design**

B_{xo}	B_{yo}	B_{zo}	B_{zR}
0.187	0.1053	0.146	0.196

3.4.5.3 System Configuration

The magnet system configuration for the 8' x 8' test section presented here (Fig. 3.4-3), is similar to that presented in ref. [2] (Fig. 3.4-2), except:

1. The four saddle R coils are shorter in length.

2. The two drag X coils are placed around the Z and Y coils to reduce the ampere-meters and to minimize structure. The present arrangement simplifies and reduces the X and R coils in size, energy, and weight; there is 30% volume reduction in cryostat and structure.

3.4.5.4 Magnet System Requirements

The magnet system remains the same as the 1985 design with a 30% reduction in ampere-meters and 45% reduction in energy stored compared to the 1985 design. It consists of one epoxy impregnated superconductive model coil with holmium insert, 4 Z gradient coils, 4 Y gradient coils, 2 X drag coils, and 4 R saddle coils. The Z, Y, and R coils are fully bipolar while the X coils are monopolar. The symmetry of the

84

coil array enhances the reliability of the magnet system.

All system requirements for static forces and torques plus the 10 Hz dynamic control forces are met with the system configuration described in Section 3.4.1. Other magnet requirements such as peak magnetic field strength, peak voltage at the magnet terminals and the structure requirements are within the state of the art.

3.4.5.5 Coil Shapes

All coils are solenoids except the saddle R coils. The use of a short saddle R coil in 1989, instead of the 1984 race track or the 1985 long saddle R coils minimizes ampere-meters and stored energy [2,3].

3.4.5.6 Coil Terminal Voltages

The requirement for dynamic control is ± 0.1% of any magnet current at 10 Hz. Accordingly the maximum voltage across any single MSBS coil is about 352 V on the X coil.

The power supply maximum voltage and power is determined for I = 11 kA in all coils and for the maximum amplitude 10 Hz correction applied to each coil continuously. The power supply voltage for the initial charging of all coils to full current in 25 sec is less than for the 10 Hz load. The 2 min charging powers are smaller, as seen in Table 3.4-7. The total power requirement is 42% less than in 1985 [3].

Table 3.4-7

Voltage and Power Requirements per Coil
(1989 MSBS Design)

Coil	10 Hz at 0.1% of max current		2 min charge specification	
	Voltage V	Power MW	Voltage V	Power MW
Z	86	0.95	18.1	0.20
Y	48	0.54	10.2	0.11
X	352	3.87	74.0	0.81
R*	120	4.62	88.2	0.97
Total Power** (1989) Total Power (1985)	18.3 MW 31.2 MW		3.83 MW 7.22 MW	

* Four saddle coils in series and considered as one coil.
** For all coils simultaneously.

3.4.5.7   Magnet Control Requirements

The control requirement is ± 0.1% of the static forces at 10 Hz. Each R, Y and Z coil has a 3-phase Graetz bridge SCR bipolar power supply with sufficient voltage to provide 10 Hz current variation for control (see Table 3.4-7). The X coils are monopolar and require only monopolar power supplies. In all cases the power supply voltage must be sufficient to overcome any unwanted voltage pickup from any other coil undergoing control current correction in addition to providing its own dI/dt.

3.4.6   Magnet Design

3.4.6.1   Configuration

The magnet system configuration shown in Fig. 3.4-3 consists of 14 superconducting coils arranged around the tunnel test section.   The function and arrangement of these coils is discussed in Section 3.4.5.   All the coil forms are slotted stainless steel with epoxy plate reinforcement.   The forces and torques between the coils are contained by cold non-metallic structure to minimize eddy current losses. Details of the dewar and structure are in Sections 3.4.7 and 3.4.8.

3.4.6.2   Conductor

The conductor in all X, Y, Z and R coils is the ANL 11 kA cable conductor discussed in the MMI 1985 design [12].

3.4.6.3   System Analysis

The maximum self and total field in each coil is listed in Table 3.4-8.   It is seen that 5.9 T on the Z coils is maximum.

Table 3.4-8

Maximum Winding Fields in Tesla

Coil	Self Field Maximum	Total Field Maximum
R	2.94 T	4.05 T
X	3.55	4.00
Y	4.31	5.30
Z	4.99	5.90

In the MMI 1985 study [3], magnetic forces were calculated for all coils in the system under maximum static forces and moments for different modes of operation. In this MMI 1989 report, forces and moments are scaled for the new ampere-meters in the X, Y, Z and R coils, see Tables 3.4-9 and 3.4-10. As before, rigid, bi-directional coil supports are planned.

Table 3.4-9

Approximate Forces and Torques on Z, Y, and X Coils*

Coil	F_x (MN)	F_y (MN)	F_z (MN)	T_x (MN·m)	T_y (MN·m)	T_z (MN·m)
Z	± 2.5	± 8.4	± 1.8	± 3.0	± 5.4	0
Y	± 1.9	± 1.4	± 6.3	± 7.0	0	± 4.0
X	± 1.3	± 1.8	± 1.8	0	± 2.6	± 2.6

*Scaled from the MMI 1985 study [NASA CR-3937]

The self and mutual inductance matrix of the MSBS coil system are listed in Table 3.4-11. The mutual inductances between coils are relatively small compared to self inductances.

Table 3.4-10

Forces on the R-Coil (half of the top left coil)

Section	Type	Axis	Length	F_x (MN)	F_y (MN)	F_z (MN)
1	Straight	x-axis	0.3 m	0	± 0.34	± 1.87
2	Straight	x-axis	0.3 m	0	± 0.30	± 1.27
3	Straight	x-axis	0.3 m	0	± 0.30	± 1.27
4	Straight	x-axis	0.3 m	0	± 0.34	± 1.87
5	Arc	y-axis	90°	± 3.45	± 1.40	± 4.31
6	Arc	x-axis	90°	± 7.0	± 1.35	± 1.00
7	Arc	z-axis	90°	± 1.4	± 1.59	± 3.10

The operational effects of maximum field, force and inductance are determined. For example, the forces on a drag coil are due to each of the four roll coils as listed in Table 3.4-12. The maximum force in the x-direction on the drag coil from the roll coils is approximately 30 MN. To produce this force, the current in two of the roll coils flows in the opposite direction from the current in the other two R coils. This is not realistic, because in all modes of operation, the current in each of the roll coils will be equal and in the same direction since the four roll coils operate in series. Thus these large forces cancel each other. A similar situation, but on a smaller scale, occurs for the X, Z, and Y coils. Every coaxial pair of these magnets carries almost the same current in the same direction during operation. It is desirable to connect each pair of these coils in series.

Table 3.4-11

Inductance Matrix in Milli Henries for the 1989 MSBS Design

Coil	Z-1	Z-2	Z-3	Z-4	Y-1	Y-2	Y-3	Y-4	X-1	X-2	R
Z-1	184										0
Z-2	6.9	184									0
Z-3	2.3	0.8	184								0
Z-4	0.8	2.3	6.9	184							0
Y-1	+ 2.7	+ 0.7	- 0.7	- 0.7	104						0
Y-2	+ 0.7	+ 2.7	- 0.7	- 2.7	4.0	104					0
Y-3	- 2.7	- 0.7	+ 2.7	+ 0.7	1.3	0.8	104				0
Y-4	- 0.7	- 2.7	+ 0.7	+ 2.7	0.8	1.3	4.0	104			0
X-1	+18	+18	-18	-18	+14	+14	-14	-14	764		0
X-2	-18	-18	+18	+18	-14	-14	+14	+14	27	764	0
R	0	0	0	0	0	0	0	0	0	0	953
	194	194	194	184	110	110	110	110	791	791	953

However, this puts some restriction on the control requirements of these coils. Two possible solutions are considered. The first is to separate the control function of the coil from the magnetic field requirements by adding an extra separate winding to each coil to perform the control function. In this case each pair of coils is connected in series and the control windings are separate. The other solution, the one we adopt, is a control system which can't pass large currents in non-operational combinations. This makes the structural, power and material requirements more economical.

Table 3.4-12

Forces and Torques on the Drag Coil Due to the Roll Coils

Coil	F_x (MN)	F_y (MN)	F_z (MN)	T_y (MN-m)	T_z (MN-m)
R-1	4.7	0.86	− 0.86	5.24	− 5.24
R-2	− 4.7	0.86	0.86	− 5.24	− 5.24
R-3	4.7	− 2.86	0.86	− 5.24	5.24
R-4	− 4.7	− 0.86	− 0.86	5.24	5.24

3.4.6.4   Model Core Solenoid

The model core solenoid as tested has a total magnetic moment of 2.89×10^4 Am^2 of which 0.361×10^4 Am^2 is due to the holmium insert. The potted solenoid is 70 cm long and 11.3 cm OD. The volume of contained liquid helium is less due to the holmium volume. Coil parameters are listed in Table 3.4-13.

91

Table 3.4-13

Model Coil Parameters

Length (cm)	70.0
Winding OD (cm)	11.326
Winding ID (cm)	8.288
Holmium insert OD (cm)	7.597
Holmium insert ID (cm)	5.877
Holmium insert length (cm)	67.36
Winding current density (A/m^2)	$3. \times 10^8$
Operating current (A)	66.9
Peak winding field (T)	6.1
Holmium magnetization (T)	3.7
Number of turns	49703
Conductor diameter (cm)	0.406

Details of the model solenoid and its cryostat are included in Section 3.1.

3.4.6.5   X, Y, Z and R Coils

The specifications for the X, Y, Z and R coils are listed in Tables 3.4-14, 3.4-15 and 3.4-16. Note that most of the energy is stored in the X coils where it is contained by internal structure bifilar stainless steel strip. The cabled conductor is the well qualified ANL 11 kA conductor [12] that is cryostable and low loss for 9 T/s pulsing in 4.2 K liquid helium baths [3].

Table 3.4-14

X Drag Coil Parameters

Number of coils	2.0
Operating current (kA)	11.0
Winding current density (kA/cm^2)	1.916
O.D. (m)	5.8
I.D. (m)	4.6
Height (m)	0.6
Number of turns	313
Inductance (H)	0.764
Energy stored/coil (MJ)	46.2
Ampere-meters (MAm)	53
Bifilar S.S. strip width (cm)	0.262
Voltage for 10 Hz (V)	352
AC losses/coil at ± 0.1% I at 10 Hz (W)	59

Table 3.4-15

Z/Y Coil Parameters

Number of coils	4
Operating current (kA)	11.0
Winding current density (kA/cm^2)	3.825/4.13
O.D. (m)	2.35/2.2
I.D. (m)	1.3/1.2
Height (m)	0.16/0.12
Number of turns	292/225
Inductance (H)	0.184/0.104
Energy stored/coil (MJ)	11.1/6.31
Ampere-meters (MAm)	18.50/13.25
Bifilar S.S. strip width (cm)	0.224/00
Voltage for 10 Hz operation (V)	86/48
AC losses/coil at 0.1% I at 10 Hz (W)	19.0/13.4

Table 3.4-16

R Coil Specifications

Saddle coils in series (number of coils)	4
Operating current (kA)	11
Winding current density (kA/cm^2)	1.584
Turns/saddle coil	215
Total turns (4 coils)	860
Inductance (4 series coils) (H)	0.95
Energy stored (MJ) (4 coils)	58
Ampere-meters (MAm) (4 coils)	108
Bifilar stainless steel thickness (cm)	0.1
Voltage for 10 Hz operation (V)	420
Ac losses at 0.1% dynamic force at 10 Hz (W)	126

The coil weights are divided between the interleaved stainless steel strip, 0.42 cm to 0.19 cm thick, and the conductor which includes a 0.1 cm strip of internal steel. The weights are listed in Table 3.4-17.

Table 3.4-17

Coil Weights, kg
(1989 MSBS Design)

Coils	R	X	Y	Z
Conductor	11,186	5,464	1,256	1,745
S.S. trip (width cm)	2,705 (0.10)	3,514 (0.26)	--	1,000 (0.22)
Total	13,891	8,978	1,256	2,745
No. Coils	1*	2	4	4
Total weight (kg)	13,891	17,956	5,024	10,980
Sum (1989 design) Sum (1985 design)	47,851 80,836			

*Four series saddle coils treated as one coil

94

The ac losses in the coils and stainless steel structural interleaved strip at 10 Hz for full and quarter load are listed in Table 3.4-18. Hysteresis for the 6.7 μm filaments of NbTi is the major loss item. At quarter load hysteresis is only about half the value at full load while the eddy current losses are reduced to 1/16.

The eddy current losses into the liquid helium from 10 Hz ac induced currents in nearby cold S.S. structures (Table 3.4-19) are small compared to the losses in the 1984 design because the structure is mostly non-metallic with only minor stainless steel in the X coils.

Table 3.4-18

Coil AC Losses at 10 Hz in W
(1989 MSBS Design)

Coil	R	X	Y	Z	Sum
Hysteresis	96.6	46.7	11.0	15.5	
Conductor	18.9	9.2	2.2	3.2	
S.S. strips	10.5	3.1	0.2	0.3	
Total	126	59	13.4	19	
No. coils	1	2	4	4	
Total, full load	126	118	53.6	76	374* W
Total, quarter load	55.6	52.8	24.4	33.6	166.4+

* ,+ These numbers were 522 and 213.4 in the 1985 study [3].

Table 3.4-19

Eddy Current Losses in Structure and Helium Vessel

Power loss at full load	120* W
Power loss at 1/4 load	30⁺ W

* ,+ These numbers were 200 and 50 in the 1985 study [3].

3.4.7   Structural Design

3.4.7.1   Structure Concepts

There are four structural design drivers:

1.   Size and location of the magnets.

2.   Magnet forces and torques.

3.   Choice between individual or one common magnet cryostat.

4.   Design and material selection to minimize eddy current losses.

In the 1984 design there were significant structural and thermal advantages to having all of the magnets in a common cryostat. That arrangement allowed the magnets to be as close as possible to the wind tunnel and to each other and eliminated the thermally inefficient transfer of forces from cold to warm and back to cold structure. It was also learned that metallic structure eddy current losses had the major impact on the size and cost of the cryogenic system.

The 1985 structure design retained the above features and incorporated several improvements which are:

1. A low heat leak load-bearing "egg-crate" thermal-vacuum enclosure immediately around the wind tunnel to get the magnet array as close as possible to the tunnel with only a 2 mm thickness stainless steel sheet between the magnets and the model coil. This thin sheet is essentially transparent for 10 Hz control field penetration.

2. The separation of magnet structure from helium containment (see Chapter V. of ref. [3] for details).

3. Except for longitudinal corners and end assemblies, the structure is epoxy-fiberglass which produces no eddy current heating. Both the inner and outer cold walls of the cryostat have longitudinal electrical breaks and the combination end plate/drag coil containment assemblies each have radial breaks. These features reduce full load structural eddy current losses from 1560 W to 200 W.

The new 1989 structure design remains the same as the 1985 design except for the following improvements. It is 30% shorter as shown in Figs. 3.4-2 and 3.4-3 of Section 3.4.1. Forces between coils and torques are about 40% to 50% lower. There are no new drawings or detailed design calculations in this study because of the similarity between 1985 and 1989 design. The 125,000 kg weight of the cryostat assembly and

magnet attachment for the 1985 design is scaled down for the 1989 design to 90,000 kg. Costs are reduced proportionally.

3.4.7.2 Weight Summary

Estimated weights of MSBS system components are scaled from the 1985 design and are given in Table 3.4-20. The total weight is 140,000 kg ± 15%, which is 35% less than the 1985 MSBS design.

<div align="center">

Table 3.4-20

1989 MSBS System Estimated Weight

</div>

Component	Weight
Cryostat total	75,000
Helium -- 20,000 ℓ	2,500
Magnets	47,900
Bolts, magnet clamp plates, miscellaneous	15,000
Total weight	140,400 kg

3.4.8 Thermal and Cryogenic System

This is an update for the thermal and cryogenic system of the 1985 design [3]. The update is based on: 1) 25% reduction in cryostat length. The diameter stays unchanged. 2) Reduced ac losses due to 30% reduction in magnet ampere-meters and 50% reduction in magnet structure. The text of this chapter stays mostly the same as it is in ref. [3] except for the thermal and cryogenic calculations for the new design.

3.4.8.1   Cryogenic Concepts

A schematic of the proposed cryogenic system is shown in Fig. 3.4-5.   Major elements of the system include the magnet cryostat, helium liquefier, helium storage dewar, helium recovery compressor, 18 atm. helium gas storage, and a cooldown loop.   Design of the system is based on the following criteria:

- ▶   Reasonable cooldown time of seven to eight days.

- ▶   Adequate liquid storage to fill the magnet cryostat with reserve to meet daily operating deficits.

- ▶   Available liquid storage capacity sufficient to empty the cryostat without loss of helium.

- ▶   Liquefaction capacity to maintain scheduled operations on a continuous basis.

- ▶   Sufficient compressor capacity to handle the maximum planned rate of gas evolution without helium loss.

- ▶   Helium gas storage for all of the helium in the system to permit an indefinite shutdown.

Considerations relating to the design and operation of each part of the system are discussed in the following sections.

3.4.8.2   Cryostat Heat Leak

Static heat leak of the cryostat is given in Table 3.4-21.   Over half of the heat leak, 19.0 W, is due to the egg crate assembly which is relatively thin, 0.152 m, and utilizes

Perlite insulation which is much less efficient than multilayer. However, multilayer insulation is not feasible for the cellular structure of the egg crate so the major concern is to make certain that a good fill of Perlite is obtained to avoid radiation heat shorts. Projected accuracy of the static heat leak calculations are -10, +30% for the egg crate and ± 15% for the 13.9 W balance of the system making the plus side range, about twice the projected contingency.

3.4.8.3   Magnet Power Leads Heat Leak

Each magnet has a pair of leads including one pair for the series roll coils, for a total of twenty-two 11 kA leads. Since there is excess helium vapor available in all operating conditions, the leads are designed to reduce no-load losses. Thus, the leads are twice as long as normal and the vapor cooling rate at full load is 0.08 g/s, nearly double the 0.046 g/s/kA optimum rate for standard leads. Without increased cooling, full-load lead losses would be twice normal instead of 46% normal. Reductions in lead losses realized with increased vapor flows are not free because the cold vapor could otherwise return to the refrigerator to increase its capacity. However, at full load more vapor is produced than the refrigerator could accept so excess flow through the leads is the most efficient way to utilize the available vapor cooling. Lead losses presented in Table 3.4-22 reflect use of all available vapor for the leads at zero and one-fourth load and for flows limited to 0.08 g/s/kA at full load.

MSBS CRYOGENIC SCHEMATIC

Figure 3.4-5.

LEGEND

PSV - SAFETY RELIEF VALVE
BD - BURST DISC
TC - TEMPERATURE CONTROLLER
TE - TEMPERATURE SENSOR
LC - LEVEL CONTROLLER
LE - LEVEL SENSOR
LN₂ - LIQUID NITROGEN
PCV - PRESSURE CONTROL VALVE

Table 3.4-21

Static Heat Leak and Cryogen Consumption

Item	Heat Leak (W)	
	Helium	Nitrogen
Egg Crate Assembly	19.0	322.0
Lead/Vent Stack	6.0	24.0
Outer Cylinder	3.8	67.9
Legs and Braces	2.4	16.8
End Bells	1.7	30.5
Contingency (10%)	3.3	51.9
Totals	36.2 W	571.0 W
Helium Consumption -- 51.1 ℓ/h		
Nitrogen Consumption -- 12.74 ℓ/h		

3.4.8.4 Operating Losses

Combined loss values for magnets, cryostat and leads are given in Table 3.4-23. These losses determine the size of the cryogenic support system.

Table 3.4-22

Lead Losses

Magnet Load	Heat Input (W)	Helium Loss (ℓ/h)
Zero	53	74.8
1/4	59.3	83.7
Full	110	155.2

Table 3.4-23

Magnet and Cryostat Operating Losses

Source of Loss	Zero Load (W)	1/4 Load (W)	Full Load (W)
Magnets	0	166.4	374
Structural eddy current	0	30.0	120
Leads	53	59.3	110
Static heat leak	36.2	36.2	36.2
Conductor joints	0	2.2	35.7
Totals (W)	89.2	294.1	675.9
Helium Consumption (ℓ/h)	125.8	414.9	953.5

The cryogenic system cost decreases only about 3% if the MSBS is designed to operate on a five-day week cycle in which the weekend is used to catch up on the liquid helium supply [2]. Thus continuous operation seven days per week is chosen.

Assumptions used in sizing the cryogenic system include:

1. Cryostat liquid capacity is 20,000 liters.

2. 3000 liters of helium are required for final cooldown of the cryostat from 20 K to 4.2 K.

3. Daily operating sequence includes 2 hours at full load, 8 hours at one-fourth load, and 14 hours at zero load.

Size of the refrigerator/liquefier is based on the operating sequence:

Full load -- 953 ℓ/h x 2 =	1,906 ℓ
One-quarter load -- 415 ℓ/h x 8 =	3,320
Zero load -- 126 ℓ/h x 14 =	1,764
Total daily requirement	6,990 ℓ
Liquefier size = 6,990 x 1.026*/24h =	299 ℓ/h

(* 2.6% allowance for storage and transfer losses)

The storage dewar is sized by the daily operating deficit and the storage requirements listed above. The daily liquid deficit is:

Full load == (953 - 299/1.026)(2) =	1,323 ℓ
One-quarter load -- (415 - 299/1.026)(8) =	989
Total daily liquid deficit	2,312 ℓ

The required dewar size is:

Final cooldown	3,000 ℓ
Fill empty cryostat	20,000
Daily liquid deficit	2,312
Subtotal	25,312
Contingency	5,062
Helium storage dewar size	30,374 ℓ

It is assumed that all of the helium in the system may be converted to gas and stored for an indefinite shutdown. Storage capacity is taken as 10% more than the dewar capacity gas equivalent and 1 atm of the 18 atm storage is considered unavailable. Thus, the volume of gas to be stored, measured at 1 atm and 294.3 K, is

$$V_g = (30,377\ell)(1.1)(0.7576 \text{ m}^3/\ell) = 25,312 \text{ m}^3$$

and the 18 atm physical storage capacity is

$$V_g = 25,312/(18-1) = 1,488.97 \text{ m}^3 = (52,580.7 \text{ ft}^3)$$

Sizing of the recovery compressor is based on the maximum liquid deficit which occurs at full load.

$$V_R = (953 \text{ } \ell/h - 299/1.026) = 661.6 \text{ } \ell/h \times 0.7576 \text{ m}^3/\ell$$
$$= 501.2 \text{ m}^3/h.$$

The recovery compressor size is

$$V_R = 501.2/60 = 8.35 \text{ m}^3/min = (295 \text{ cfm.})$$

This defines the major components of the cryogenic system which are listed in Table 3.4-24 and illustrated on Figure 3.4-5.

Table 3.4-24

Components of MSBS Cryogenic System

Liquefier (ℓ/h)	299
Storage dewar (ℓ)	30,377
Recovery compressor (m^3/min) (cfm)	8.35 (295)
System helium charge (m^3) (1 atm, 294.3 K)	25,312
Gas storage at 18 atm (m^3)	1,489

3.4.8.5 Cryogenic Component Review

All of the cryogenic system components utilize existing technology and commercial experience and there should be no difficulty in locating multiple sources of supply.

Liquefier. The 299 ℓ/h liquefier may not be a catalog size for any manufacturer but it is not large by industry standards and there are three or four American suppliers. Although not analyzed for this study, the helium liquefier is expected to utilize two or possibly three gas expanders with final expansion accomplished in a positive displacement wet expander. Overall efficiency of this size of liquefier should be in the range of 17.5 to 20% of Carnot.

Dewar. The helium dewar will probably be a vertical unit with multilayer insulation and an intermediate shield cooled with liquid nitrogen. Loss rate should be in the range of 0.1% to 0.15% per day. Three or four American companies have the technical background and facilities to build this dewar.

Gas Handling. The gas handling system includes the recovery compressor, gas bag and 18 atm storage. The compressor will be a three-stage oil lubricated machine equipped with oil removal components and a small cryogenic purifier so that only high purity helium is stored. The commercially available 354 m^3 gas bag provides a low pressure buffer volume for both the liquefier and recovery compressor. When the liquefier is down, the gas bag collects dewar boil-off for periodic pumping into storage by the recovery

106

compressor.

Eighteen atm storage consists of 13 commercial ASME coded propane tanks, each 2.74 m diameter and 20.12 m long. Although space required for this tank farm is appreciable, storage at 18 atm approximately matches the liquefier operating pressure which permits interchangeable use of the recovery and liquefier compressors.

Cooldown System. Only helium is used to cool down the cryostat to avoid the possibility of contamination. The system is designed (see Fig 3.4-5) so that both the liquefier and recovery compressors work in parallel for cooldown. Helium flow for cooldown is approximately $26.46 + 8.35 = 34.81$ m^3/min and is directed to a special cooldown heat exchanger and liquid nitrogen bath which provide the major refrigeration for cooldown. Liquid nitrogen level in the bath is adjusted for a maximum gas to cryostat temperature difference of 100 K initially to limit thermal shock. As the cooldown proceeds the temperature difference is reduced until it is less than 5 K at the end. A blower-type vacuum pump is used to reduce the final bath temperature to 65 K in order to get maximum cooling from nitrogen.

Cooling below about 70 K is accomplished by using the liquefier as a cold gas refrigerator. The liquefier is used in this manner until the cryostat is cooled to about 20 K where its enthalpy is only 0.04% of the room temperature value. Cooling from 20 K down to 4.2 K and filling the

107

cryostat is performed in a continuous liquid transfer from the storage dewar. About 3,000 ℓ of liquid helium is required for the final cooldown and 20,000 ℓ used to fill the cryostat.

<u>Liquid and Cold Gas Transfer Lines</u>. Vacuum jacketed helium lines are indicated on Fig. 3.4-5. The principal VJ line runs from the dewar to the cryostat with a cold gas extension beyond the dewar to the liquefier cold box. This co-axial line consists of a 51 OD x 0.89 mm wall inner liquid line, 5.5 mm radial insulated vacuum space, 63.5 OD x 0.89 mm inner cold gas tube, 101 OD x 1.24 mm outer cold gas tube and a 152.4 OD x 2.77 mm wall (6 IPS, Sch. 5 pipe) warm vacuum jacket. In normal liquid service this line will function as follows:

1. Liquid flows in the inner line at 0.07 to 0.136 atm above the cryostat pressure causing the liquid to be 0.1 to 0.15 K warmer than liquid and gas in the cryostat.

2. Liquid is throttled to cryostat pressure by the flow control valve which drops the temperature with production of a small percentage of flash vapor.

3. Slightly colder vapor returns to the liquefier in the annular gas passage. This cold gas intercepts heat and creates an essentially zero heat leak environment for the inner liquid line. The purpose

of the insulation space between the lines is to prevent the two passages from forming a heat exchanger whenever the return gas is warmer as during cooldown.

Controls and Safety Devices. Since design work to date has been on major functional components, neither the control systems nor safety devices are worked out in detail. As shown in Fig. 3.4-5, the cryostat is equipped with a level indicator and controller to maintain liquid above the magnets. Because the pressure rating of the egg crate structure is limited, the helium reservoir will be protected by a sensitive pilot-operated relief valve and a parallel burst disc. Each of the 22 magnet leads will be equipped with a flow controller and an overall flow controller will balance lead flows when flows are less than rated 0.88 g/s per lead. Compressors are equipped with bypass circuits and standard over and under pressure switches for automatic unattended operation. As the system detail design evolves, care will be taken to protect all potential isolated cold volumes with thermal relief valves.

Cryogenic System Cost Estimate. Estimated cost of the cryogenic system described in Table 3.4-25 is $2,646,000.

Table 3.4-25

Cryogenic System Cost Estimates
(1989 Design)

299 ℓ/h helium liquefier	$1,358,000
Dewar -- 20,500 ℓ	318,000
18 atm gas storage -- 1,500 m³	424,000
Recovery compressor -- 8.35 m³/min	136,000
LN₂ cooldown system	140,000
VJ pipe and valves	120,000
Balance of plant*	150,000
Total	$2,646,000

* No buildings or civil work.

3.4.8.6 Cooldown Analysis

Cooldown is based on the estimated 26.46 m³/min flow from the liquefier compressor plus 8.35 m³/min from the recovery compressor for a total of 34.81 m³/min. This flow rate limits cooldown of the cryostat and it is important to keep the gas to cryostat temperature difference close to 100 K for as long as possible. The estimated time for the three cooling phases is:

300 -- 70 K	130 hours
70 -- 20 K	36
20 -- 4.2 K	4
Total	170 hours, 7.1 days

3.4.8.7   General Operating Plan

The operating plan for the cryogenic system from a warm start includes the following steps:

1. Purge and fill the entire system with helium gas.

2. Start flow of liquid nitrogen to the storage dewar shield and to the cryostat shields.

3. Start the liquefier and fill the storage dewar. With a 24-hour allowance for cooldown, it will take about six days to fill the dewar.

4. Cooldown and fill the magnet cryostat.   Allow a week for this step.

5. Operate the cryostat as scheduled:

    a. Whenever gas flow exceeds liquefier capacity the recovery compressor will cycle on to pump gas back to 18 atm storage.

    b. Liquefier is sized to run continuously when there is liquid in the cryostat and the test regime is followed.   For five-day week operation the liquefier would shut down or idle over the weekend.

6. At the end of a wind tunnel operating cycle or at any time the system is to be down more than two weeks, liquid should be transferred back to the dewar and the cryostat allowed to warm up to 78 K by continuing to supply liquid nitrogen to the shields.   Restart from this point can be accomplished in about three days.

3.4.9   8' x 8' Wind Tunnel Magnet Accuracy Analysis

An additional task is to estimate the contingencies in the 8' x 8' magnet system sizes due to inaccuracies in calculating the magnetic properties of the wings and solenoid core. The variations in the ampere-meters requirement in all coils for a 1% inaccuracy in calculating the wing and model solenoid magnetic moments are listed in Tables 3.4-26 and 3.4-27.

Table 3.4-26

**Ampere-meter Contingencies for a 1%
Change in Wing Magnetization**

	X (drag)	Y (side)	Z (lift)	R (roll)
A-m	± 0.198%	± 0.893%	± 0.165%	± 1.01%

Table 3.4-27

**Ampere-meter Contingencies for 1% Changes in Wing
Magnetization and Model Solenoid Magnetic Moment**

	X (drag)	Y (side)	Z (lift)	R (roll)
A-m	± 1.004%	± 2.03%	± 2.03%	± 1.01%

The ampere-meter contingency for inaccuracy analyses is +2% for Y and Z coils and +1% for X and R coils. These contingencies are to be added to all other contingencies, tolerances, and allowances.

3.4.10   1989 Design Cost Estimate

The 1989 MSBS cost estimate is $19,142,000 for a system equivalent to Case 1 -- Alternate G of NASA CR 165917 [1]. The control power supplies are rated to provide ± 0.1% of I_{max} to all coils simultaneously at 10 Hz. The cost estimates are consistent with costs in NASA CR 165917 but updated for new,

different designs. However, several topics have not been addressed by MMI, notably the position sensor and control system estimates are carried forward from NASA CR 165917, adjusted for inflation, and marked with an asterisk (*) in Table 3.4-28.

The estimated system cost of $19,142,000 is a reduction of $10,800,000 or 36.1% from NASA CR 3802 prepared by MMI in 1984 and $2,300,000 or 10.7% from NASA CR 3937 in 1985. This significant cost reduction is attributed to the following factors:

- ► Experimental confirmation of the increased pole strength of the model core magnet by use of a holmium mandrel.

- ► The $Nd_2Fe_{14}B$ permanent magnet material can occupy 100% of the wing volume (not the previous 85%).

- ► Overall reduction in magnet sizes due to improvements in model core and wings and more efficient saddle roll coils.

- ► Improved understanding of the MSBS system.

- ► Better power supply utilization.

- ► Structural design to minimize eddy current heating.

Costs in Table 3.4-28 are not contingent on additional analytical or experimental efforts but assume and predict that such work can be accomplished as required. Future design and development work would not necessarily further reduce MSBS costs, but could improve the accuracy of the estimates and validate technical feasibilities.

Estimates include 3% per year escalation of all items
listed in the 1985 design cost estimates.

Table 3.4-28

1989 MSBS Cost Estimate (Costs in Thousands $)

1.0	Complete MSBS System		19,127
1.1	Preliminary Design Phase		985
1.1.1	System Engineering	112	
1.1.2	Magnet Preliminary Design	169	
1.1.3	Cryogenics Preliminary Design	68	
1.1.4	Power Supply and Protection Preliminary Design	34	
1.1.5	Position Sensors Preliminary Design	146*	
1.1.6	Control System Preliminary Design	101*	
1.1.7	Support Structure Preliminary Design	158	
1.1.8	Manufacturing Engineering	23	
1.1.9	Quality Control Plan	45	
1.1.10	Preliminary Design Phase Program Management	129	
1.2	Final Design Phase		3,105
1.2.1	System Engineering	169	
1.2.2	Magnet Final Design	337	
1.2.3	Cryogenics Final Design	303	
1.2.4	Power Supply and Protection Final Design	112	
1.2.5	Position Sensors Final Design	473*	
1.2.6	Control System Final Design	394*	
1.2.7	Support Structure Final Design	501	
1.2.8	Manufacturing Engineering	197	
1.2.9	Quality Control and Testing	197	
1.2.10	Final Design Phase Program Management	422	

1.3	Manufacturing, Installation and Checkout Phase		15,037
1.3.1	Engineering Support for Manufacturing, Installation and Checkout	535	
1.3.2	Special Machines and Tooling	675	
1.3.3	Manufacturing Z Gradient Coils	446	
1.3.4	Manufacturing Y Gradient Coils	317	
1.3.5	Manufacturing Roll Coils	818	
1.3.6	Manufacturing Drag Coils	560	
1.3.7	Model Core Magnet and Cryostat	169	
1.3.8	Cryogenic System	2,250	
1.3.9	Power Supplies and Protection Systems	1,369	
1.3.10	Position Sensors	1,202*	
1.3.11	Control System	1,177*	
1.3.12	Support Structure and Cryostat	1,484	
1.3.13	Quality Control and Testing	197	
1.3.14	Not Used		
1.3.15	Packing and Shipping	281	
1.3.16	Assembly and Installation	900	
1.3.17	Checkout and Acceptance Testing	1,138*	
1.3.18	Manufacturing, Installation, Checkout Phase Program Management	1,519	

* These values scaled directly from NASA CR 165917 for Case 1, Alternate G.

3.5 MSBS Integrated Design

The integrated design philosophy for magnetic suspension and balance systems promises simpler and less expensive magnets. The main principle of the integrated design is that

115

all of the model's degrees of freedom are treated and controlled simultaneously by an integrated suspension system in contrast to the conventional approach of "assigning" separate sets of coils for each degree of freedom.

In conventional design a principal set of coils is responsible for providing the required forces in a specific degree of freedom. It would have adequate ampere-meters to provide specific extreme force and additional ampere-meters to overcome any and all negative cross coupling forces from all other coils. Each coil would have a maximum ampere-meters for the worst case. The integrated design approach may utilize the same system of coils and coil locations; the difference is that secondary coil current solutions are sought which, in aggregate, assist the principal system. An example is the 14 coil design discussed later. In principle, all coils would require less ampere-meters. The mathematical problem becomes more complicated; the search now is for optimized sets of coil currents that minimize the coil system and still meet all requirements.

This is one aspect of the integrated design approach. The second aspect departs from the conventional approach in that it is possible to design MSBS system with a set of coils that do not necessarily correspond one on one with each degree of freedom requirement. An example is the 18 coil compact system in Section 3.5.5.

Each approach has advantages. The obvious advantage of the conventional non-integrated system is the ability to

associate each system function with its specific set of coils. For example, Z-coils provide lift, X-coils provide drag, R-coils provide roll, and Y-coils provide lateral forces. The standard approach leads to good designs, for example the MMI 1985 MSBS design, but does have two drawbacks: additional constraints on the magnet system, and penalizing cross coupling. Cross coupling occurs for model off-zero positions in any degree of freedom because symmetry is violated and coils interfere with each other by imposing forces on the model in directions other than their own associated force directions. Such stray forces are overcome by extra turns in the principal coils. For example, if R-coils produce stray forces in the y-direction, then Y-coils must produce the undisturbed y-forces plus the extra forces to cancel the stray forces. The extra ampere-meters for cancellation are typically about equal to the ampere-meters required at zero position and typically double the ampere-meters.

The integrated system eliminates the artificial one-on-one requirement. This new integrated design approach has several major advantages: cross coupling is not necessarily a penalty, there are more magnet configurations to choose from, and there is a possibility of achieving a larger angle of attack and a larger roll angle. Consequently, a simpler system with more capability is possible. Two favorable design options are worth investigating. The first is to eliminate the saddle roll coils, thus allowing the MSBS to be composed

117

entirely of simple solenoids. The second option is to eliminate the large size drag coils. In this study we consider only the first option for an 8' x 8' wind tunnel MSBS that is composed entirely of simple solenoids.

3.5.1   System Description

The magnet system consists of solenoids only. It is possible to produce all the required forces and torques on the model from solenoids mounted on and around the walls of the wind tunnel structure. A variable number of coils in several arrangements are possible. Two systems are considered in this integrated design study: one is a 14 coil system and the other is an 18 coil compact system. Both systems eliminate the need for saddle-type roll coils. This is a major achievement since solenoids are the simplest most standard coil configuration and the easiest one to wind.

3.5.2   Magnetic Modeling of the F16 Model

The magnetic elements of the F16 model are the superconducting solenoid in the fuselage and the two permanent magnet wings. The model solenoid is an epoxy impregnated solenoid with gross current density of 30 kA/cm^2 at 6.1 tesla. For the specifications listed in Table 3.4-2, the solenoid can be represented by a 44.5 kAm magnetic pole at each of its two ends.

For the wings the same permanent magnetic material, $Nd_2Fe_{14}B$, in the same F16 wing shape used in the MMI 1985 study

118

is used for this study. In a conventional design, each wing is modeled as two permanent magnetic pole tips. The pole tip strength is such that a linearly varying z-field (B_z) with a zero value at the center line produces the exact torque on the wing. This is accurate enough in the conventional design because of the linearity of the magnetic field across the wings. This linearity results from the symmetry constraints on the support magnets. However, in the integrated design the external fields are not required to be symmetrical or linear across the wings. Modeling of the wing is more complex. Each wing is represented as a distribution of magnetic charges on all surfaces. The intensity of the magnetic charge at a surface point is a function of the magnetization magnitude and inclination angle to the surface. The charges are integrated into a finite number of charges on the wing mid-plane, which accounts for the wing thickness. By this procedure a wing is represented by a distribution of + charges (for example) at the tip and - charges at the fuselage. For mathematical convenience the charges are located on the two-dimensional mid-plane of the wing. This is equivalent to a staggered stacking of different length bar magnets to approximate the shape of a wing, with all north poles pointing toward the wing tip. The other wing can be identical or opposite polarity.

The wing is divided into an n_x by n_y grid by two sets of planes, Fig. 3.5-1. The first set is parallel to the z-x plane. The second set is parallel to the z-axis and contains
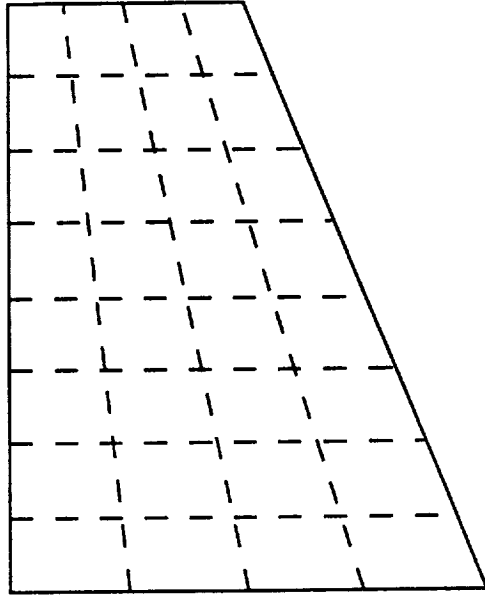
Figure 3.5-1.   Magnetic Charges on Wing Material.

lines connecting equi-distance points on the y = o and y = 0.41 m sides. Any degree of accuracy can be achieved by sufficient subdivision. This is an improvement over previous studies where only one bar magnet per wing was used.

The F16 wing is subdivided into a 2 x 4 grid to get 18 magnetic poles distributed along the plane body and the wings. Table 3.5-1 lists pole strength Q_m in ampere-meters and the distribution of magnetic poles. The first and second poles represent the model magnet, while the other poles represent the wings. These pole strengths are used to calculate magnetic forces and torques on the model.

Table 3.5-1

Magnetic Pole Distribution of the F16 Model

IQ	A(kAm)	X (mm)	Y (mm)
1	44.5000	350.00	0.00
2	-44.5000	-350.00	0.00
3	-1.3960	86.87	103.70
4	0.5654	69.05	191.20
5	0.4195	51.23	278.80
6	0.4115	33.41	366.20
7	-0.9404	260.60	103.70
8	0.3808	207.20	191.20
9	0.2825	153.70	278.80
10	0.2771	100.20	366.20
11	-1.3960	86.87	-103.70
12	0.5654	69.05	-191.20
13	0.4195	51.23	-278.80
14	0.4115	33.41	-366.20
15	-0.9404	260.60	-103.70
16	0.3808	207.20	-191.20
17	0.2825	153.70	-278.80
18	0.2771	100.20	-366.20

3.5.3   System Analysis

The design of the integrated MSBS system is based on minimizing the magnet system cost. The general procedure is to choose subsets of identical cylindrical solenoids mounted on and around the tunnel walls. All coils cross-couple to satisfy the force and torque requirements of the wind tunnel. The degree of each coil participation is governed by the cost function and the coil-model force interaction matrix.

Cost optimization of the coils concerns the cost function

$$Z \propto \sum_{i}^{N_s} N_i \, (1/2 \; L_i \; I_i^2)^{3/4}$$

here L_i is the self inductance of each coil in the ith subset of identical coils

I_i is the maximum current in the ith subset

N_i is the number of coils in the ith subset

N_s is the number of subsets of identical coils

I_i is the maximum current in the ith set determined by searching through all coil currents in this set required to hold the model in any position with the required torques and forces. The set of maximal currents I_i do not in general occur simultaneously.

The energy $1/2 \; L_i \; I_i^2$ is the maximum energy encountered in each coil under its own extreme currents. The exponent 3/4 in the cost function is an empirical replacement for cost = $aE^{2/3}$ + bE, where "a" is the ampere-meter associated cost term and

123

"b" is the structure cost term. The utilization of the cost equation is to select between the most economic coils that still satisfy all model balance and control requirements.

The cost function cannot be used directly to get the current in the different coils. The following analysis obtains an objective function that can be used directly to get currents in the different magnets.

An objective function could be

$$\phi \propto \sum_{i}^{N_s} a_i \, N_i \, I_i^{k_i} \quad ,$$

where a_i and k_i are parameters. At any particular model position, the relationship between a subset maximum current at this position $I_{max,i}$ and its absolute maximum current I_i is

$$I_i^{k_i} = b_i \, I_{max,i}^{k_i}$$

where b_i varies from one model position to another. The maximum current in a subset at a particular position is related to the average absolute current in this set at this position by

$$I_{max,i}^{k_i} = \sum_{i}^{N_i} |I|^{k_i} / \eta_i \, N_i \quad ,$$

where η_i is a pseudo-efficiency factor that measures the degree of utilization of the coils in the ith subset at this

model position. This varies from one model position to another. From the above equations, the objective function is written as

$$\phi - \sum_{i-1}^{N_s} C_i \sum_{j-1}^{N_i} I_j^{2m_i}$$

where C_i and m_i vary in general among different subsets and different force and position constraints. To simplify the analysis, we will assume that all m_i are equal to m, all C_i vary only among coil subsets, and each C_i is independent of the force-position constraints.

This objective function is used to calculate for each specific position, force and torque requirement the current in each coil that collectively satisfies the constraints. The set of currents in the coils for a specific position, force, and torque are in general functions of the parameters C_i and m.

To undertake the cost optimization, the single case maximum current for each of the coil subsets is determined. For example, consider an MSBS system composed of 3 subsets of coils mounted on the X, Y and Z walls. The maximum current for the X-coil subset is determined, for a set C_1, C_2, C_3 and m, by searching through all the X-coil currents required for all model positions, torques and forces. The maximum currents in the Y and Z-coil subsets are determined similarly. The three maximal currents in general do not occur simultaneously for any one model position. These three maximal currents are used to calculate one point of a cost grid.

125

3.5.4   Fourteen Coil MSBS

A new magnet system design for the 8' x 8' wind tunnel MSBS is optimized using the above optimization procedure, and satisfies the NASA specifications of the MMI-1985 MSBS design and matches its capabilities with 30% less ampere-meters and with simpler solenoidal coils.   The system consists of 4 subsets of coils, first level Z-coils, second level Z-coils, Y-coils and X-coils, Fig. 3.5-2.   Each Z1, Z2 and Y subset consists of 4 fully bipolar superconductive solenoids while the X-coils consist of 2 monopolar superconductive solenoids.

This symmetric coil set satisfies all system requirements for simultaneous maximum static forces and torques at zero, intermediate, and maximum rotations in addition to the 10 Hz dynamic control forces.   Magnet requirements such as current density and field strength are within the current state of the art.

The specifications for the X, Y, Z1, and Z2 coils are listed in Tables 3.5-2, 3.5-3, 3.5-4 and 3.5-5.   The total Am of the system is 328 MAm.   This includes a 2% allowance for dynamic control.

Table 3.5-2

X-Coil Parameters

Number of coils	2
Operating current (kA)	11.0
Winding current density (kA/cm^2)	1.58
O.D. (m)	5.2
I.D. (m)	4.52
Height	0.4
Number of turns	195
Inductance	0.32
Energy stored/Coil (MJ)	19.5
Ampere-meters (MAm)	32.8
Maximum Self Field (tesla)	2.39

Table 3.5-3

Y-Coil Parameters

Number of coils	4
Operating current (kA)	11
Winding current density (kA/Cm^2)	2.0
O.D. (m)	2.4
I.D. (m)	1.7
Height (m)	0.3
Number of turns	191
Inductance (H)	0.096
Energy stored/coil (MJ)	5.8
Ampere-meters (MAm)	13.5
Maximum self field (Tesla)	3.05

Table 3.5-4

Z1 - Coils Parameters

Number of coils	4
Operating current (kA)	11.0
Winding current density (kA/cm^2)	2.09
O.D. (m)	2.3
I.D. (m)	1.15
Height (m)	0.35
Number of turns	382
Inductance (H)	0.246
Energy stored/coil (MJ)	14.86
Ampere-meters (MAm)	22.8
Maximum self field (tesla)	5.08

Table 3.5-5

Z2 - Coils Parameters

Number of coils	4
Operating current (kA)	11.0
Winding current density (kA/cm^2)	2.12
O.D. (m)	2.70
I.D. (m)	1.70
Height (m)	0.40
Number of turns	385
Inductance (H)	0.37
Energy stored/coil (MJ)	22.47
Ampere-meters (MAm)	29.3
Maximum self field (tesla)	4.76
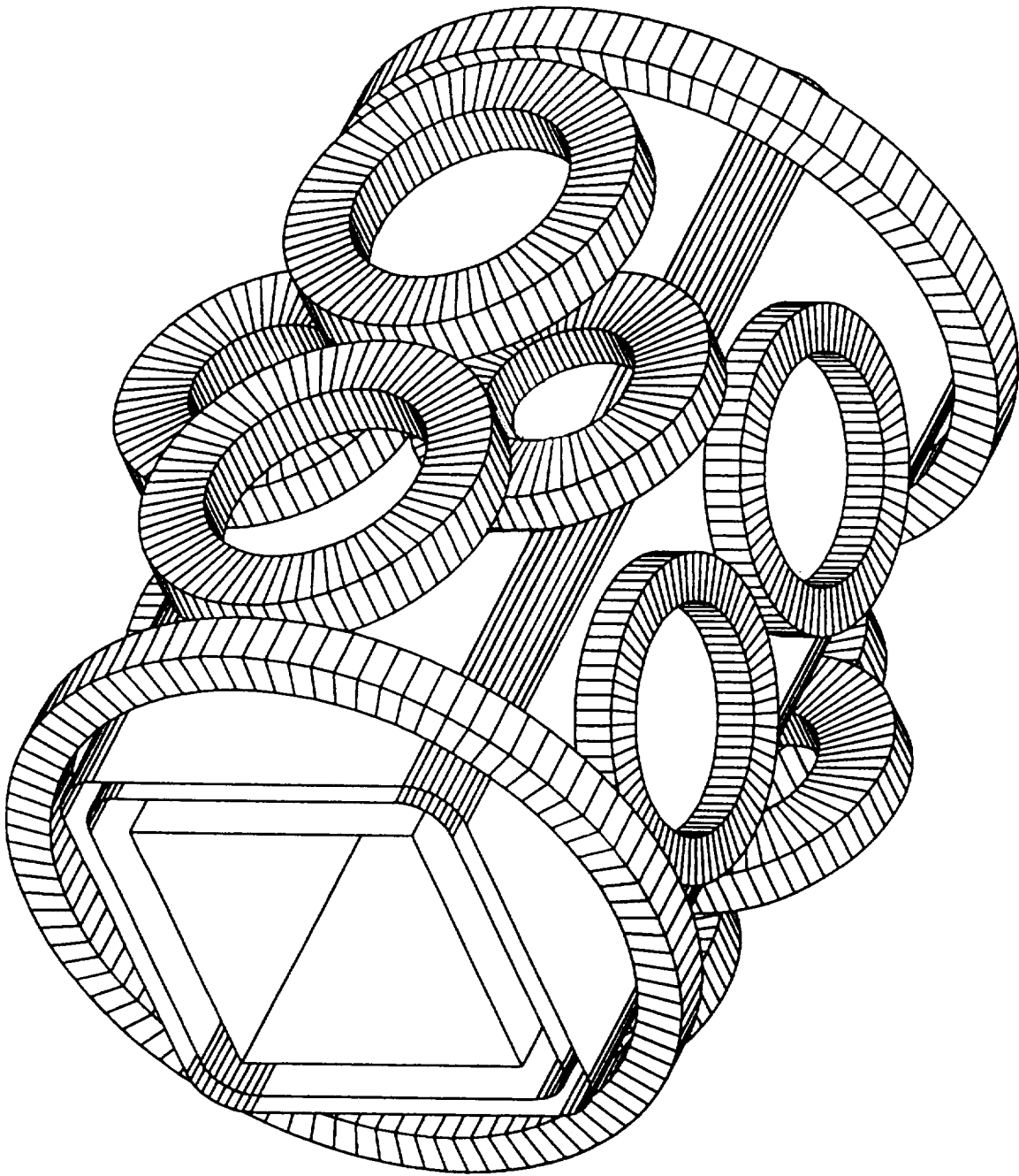
Figure 3.5-2a.   14 Coil Set.

129
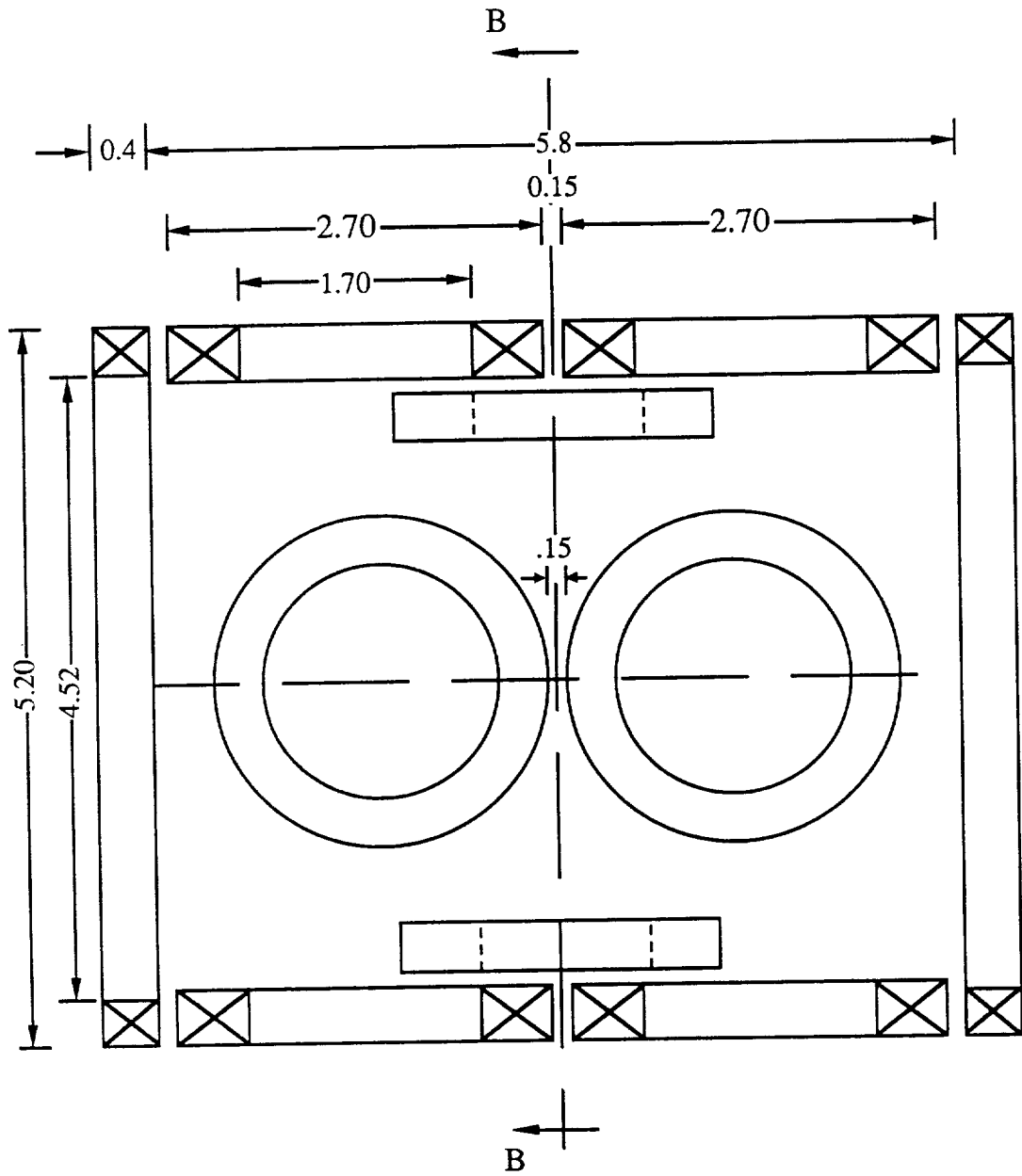
SECTION A-A

Figure 3.5-2b. 14 Coil Set (Side View).
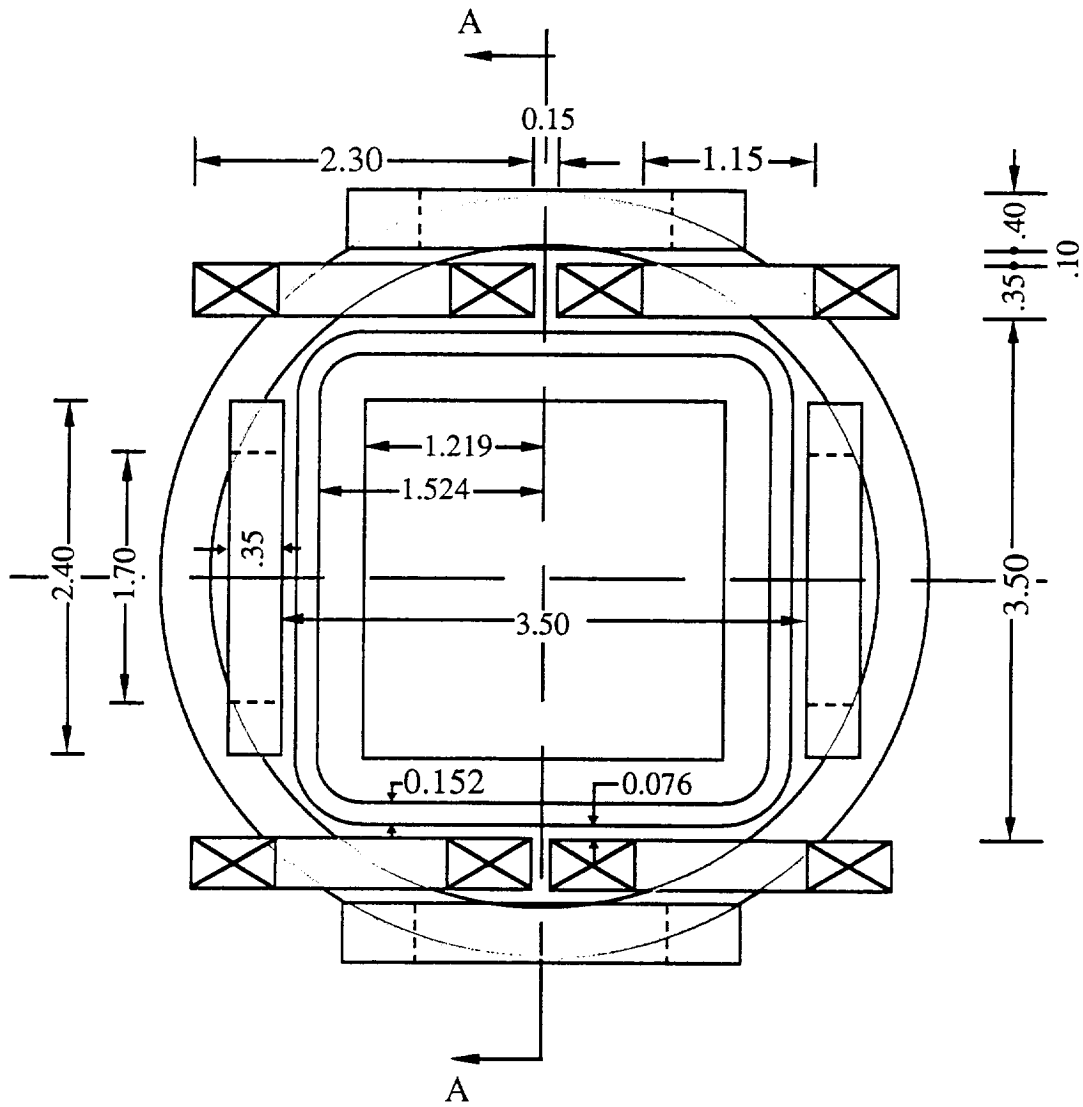
SECTION B-B

Figure 3.5-2c. 14 Coil Set (Front View).

131

3.5.5   Eighteen Coil Compact MSBS

An alternative eighteen coil compact MSBS system is investigated. The system consists of 8 Z-coils, 8 Y-coils and 2 X-coils, Fig. 3.5-3. The Z-coils are mounted symmetrically on the top and bottom walls of the tunnel, the Y-coils are mounted symmetrically on the left and right walls of the tunnel, while the X-coils are mounted one around each of the front and back of the tunnel. This configuration does not render itself easily to the conventional design approach because the system does not include specific roll coils. It is easy to see that roll, at zero position for example, is produced by all the 8 Z-coils and all the 8 Y-coils.

The specifications for the X, Y and Z coils are listed in Tables 3.5-6, 3.5-7 and 3.5-8. The total ampere-meters of the system is 385 MAm, which is 82% of MMI 1985 design. This allows for 2% extra capacity for dynamic control.

The system consists of three sets of identical cylindrical solenoids. All coils are wound with ANL 11 kA superconductor cable. The current density and self magnetic field are within the state of the art.

While the 14 coil configuration presented in section 3.5.4 consists of a fewer number of coils with a less total ampere-meters, the 18 coil system is more compact and the solenoids are smaller in size. This aspect may have a favorable impact on the cost of the structural support. Investigating the structural aspect of both designs is beyond the scope of this effort.

132

Table 3.5-6

X-Coil Parameters (18 Coil Design)

Number of coils	2
Operating current (kA)	11
Winding current density (kA/cm^2)	1.73
O.D. (m)	5.32
I.D. (m)	4.52
Height (m)	0.4
Number of turns	252
Inductance (H)	0.598
Energy stored (MJ)	36.2
Ampere-meters (MAm)	42.78

Table 3.5-7

Y-Coils Parameters (18 Coil Design)

Number of coils	8
Operating current (kA)	11.0
Winding current density (kA/cm^2)	2.14
O.D. (m)	1.60
I.D. (m)	0.64
Height (m)	0.4
Number of turns	374
Inductance (M)	0.119
Energy stored (MJ)	7.18
Ampere-meters (MAm)	14.46

Table 3.5-8

Z-Coils Parameters (18 Coil Design)

Number of coils	8
Operating Current (kA)	11.0
Winding current density (kA/cm^2)	2.14
O.D. (m)	2.10
I.D. (m)	1.00
Height (m)	0.4
Number of turns	428
Inductance (H)	0.255
Energy stored (MJ)	15.4
Ampere-meters (MAm)	22.92
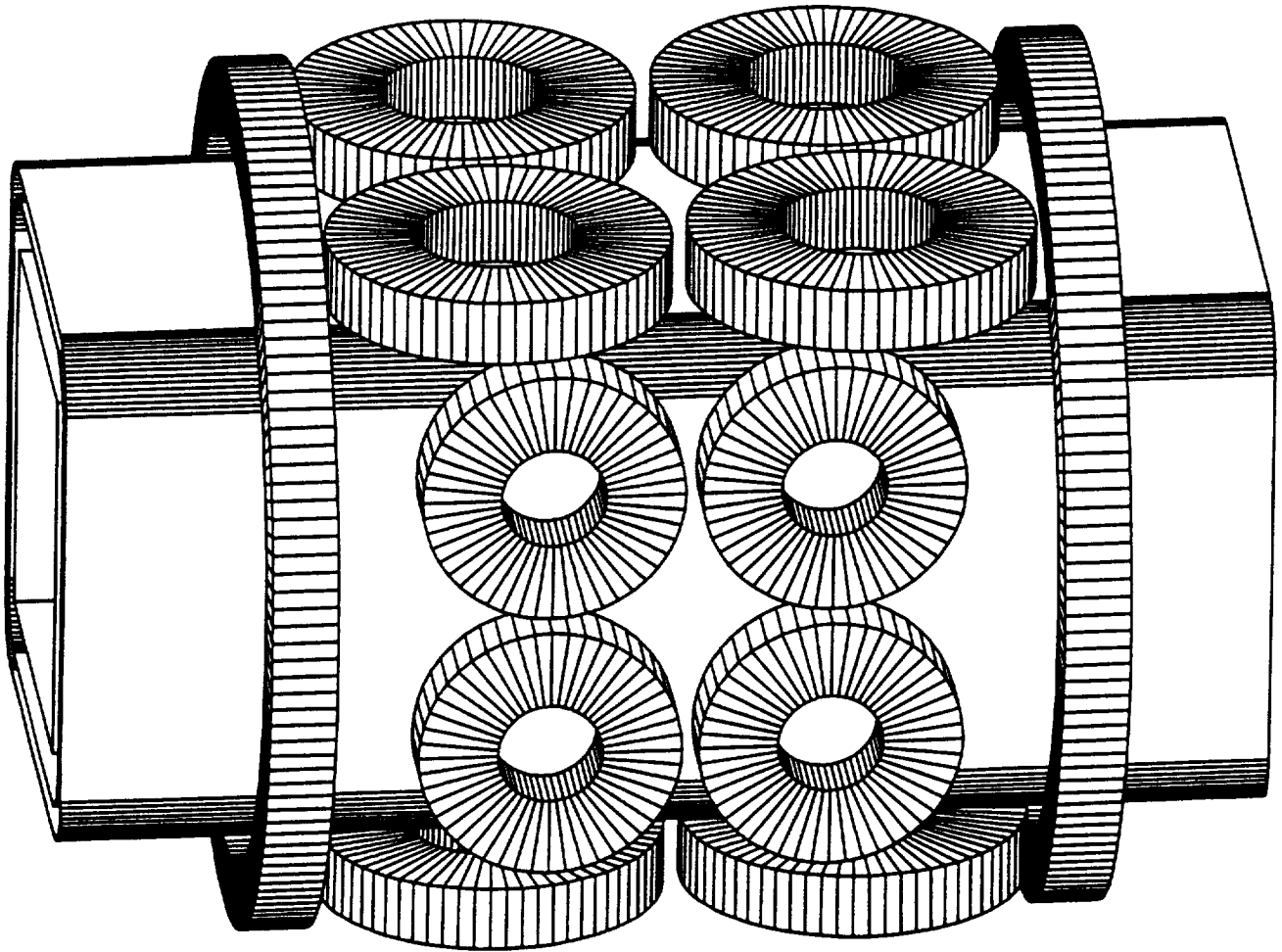
Figure 3.5-3a.   18 Coil Set.
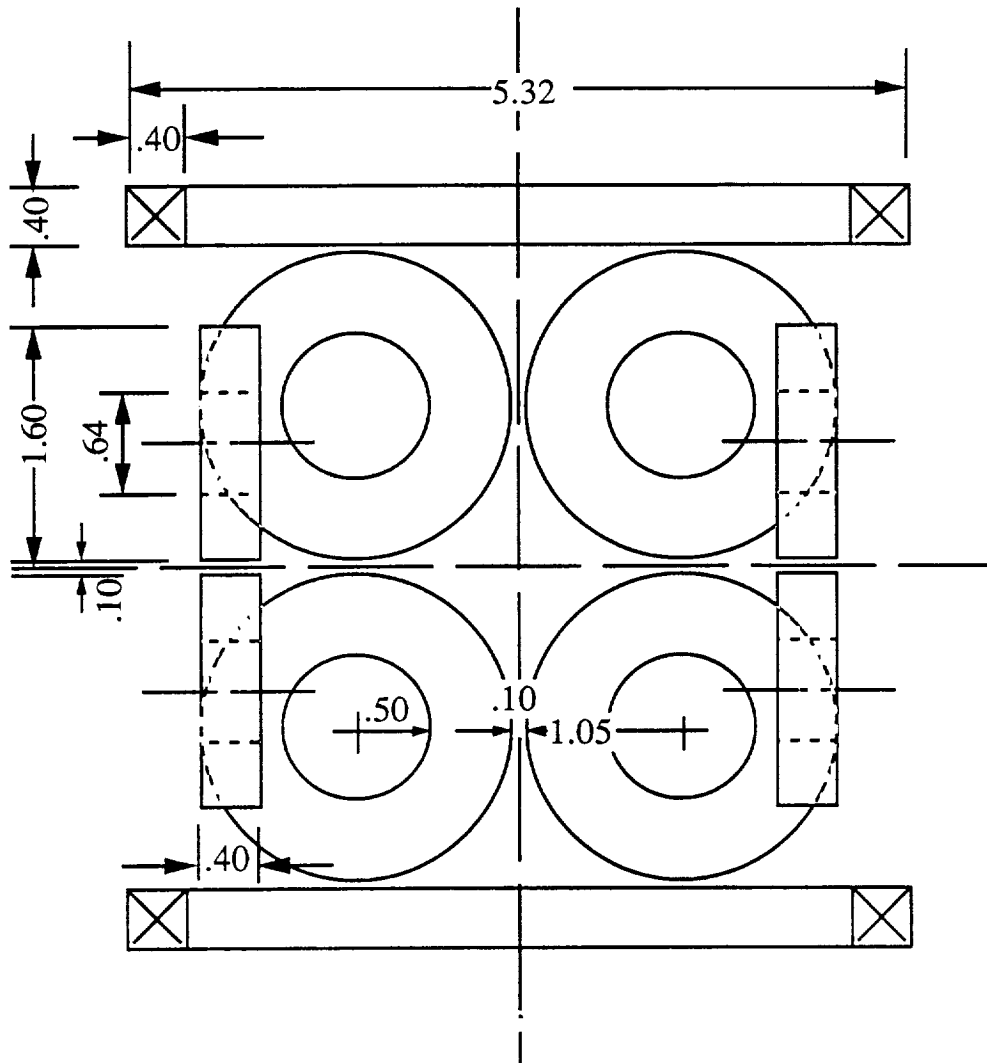
Figure 3.5-3b.   18 Coil Set (Top View).
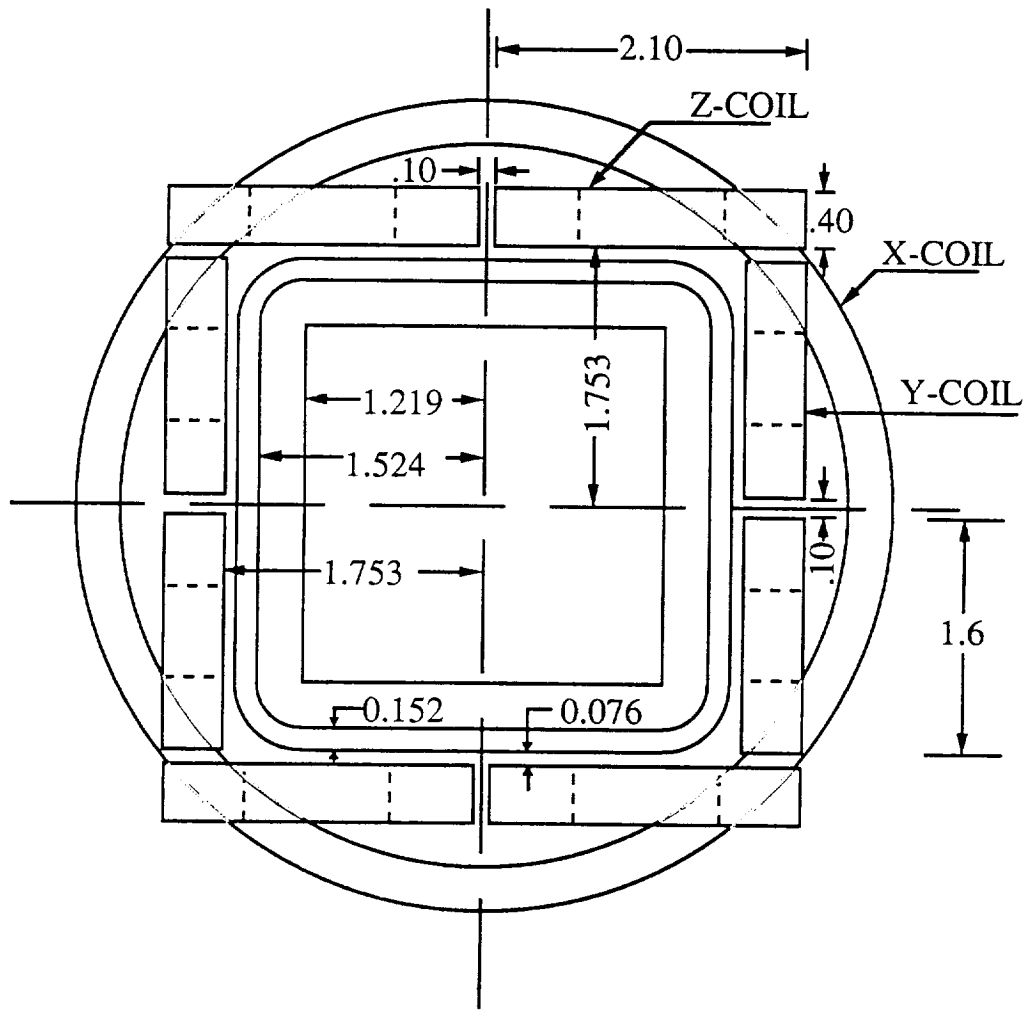
Figure 3.5-3c. 18 Coil Set (Front View).

137

3.5.6   Conclusions for Integrated Design

The applicability of the integrated system design philosophy is demonstrated for simple cylindrical solenoids: the 14 coil and the 18 coil systems. The 14 coil system demonstrates the application of the integrated system design to a conventional configuration in which each set of coils is responsible for a particular degree of freedom. The 18 coil system demonstrates the application of the integrated system design to a new non-conventional configuration in which there is no one-on-one correspondence between magnets and the model degrees of freedom.

The integrated design of the 14 coil system, Fig. 3.5-2, starts with a magnet configuration. The Y-magnets are located as close as possible to the model. The Z-coils are located in two layers with a gap between them large enough for a structural member. The Z1-coils for roll are placed on the inside closer to the model since the magnetic field requirement for roll is more demanding than for lift. The X-coils are placed tightly around the tunnel along the X-axis. Optimizing the 14 coil configuration for minimum cost obtains the lowest ampere-meters in Table 3.5-9 among all five designs. The ampere-meters in the 1989 design and the 14 coil design are about equal; however, the 14 coil design is preferred because it has no saddle coils. Saddle coils may be

more efficient for the roll function but are more difficult to wind, require more structure, and are probably more expensive per ampere-meter.

The ampere-meters listed in Table 3.5-9 show some interesting differences for the 14 coil integrated system. The ampere-meters of the 1990 X-coils are about 62% of their 1989 counterpart because the four Z2-coils (front and back) and the four Y-coils help the X-coils produce the drag force. The Y-coils are about the same size in both designs. The Z-coils in the 1990 design are about 63% larger than in the 1989 design, since the 1990 Z-coils are placed farther away from the model to allow space for the roll Z1-coils. In spite of the fact that saddle coils in the 1989 design are more efficient, it is seen that the roll coils (Z1-coils) in the 1990 design have 16% less ampere-meters, due primarily to the roll help from other coils. In addition, the Z1-coils are closer to the model than the Z-leg of the saddle coils. The Y-leg is almost the same distance from the wing as the Z1-coils.

Table 3.5-9

MMI MSBS 1984, 1985, 1989, and 1990 Designs

Coils	X	Y	Z	R	Total	%
1984 Design						
Ampere-meters (MAm)	362	100	86	207	755	100
Energy Stored (MJ)	656	60	50	140	906	100
1985 Design						
Ampere-meters (MAm)	172	71	71	154	468	62
Energy Stored (MJ)	216	38	38	116	408	45
1989 Design						
Ampere-meters (MAm)	106	53	74	108	341	45
Energy Stored (MJ)	93	25	44	58	220	25
1990 14 Coil Design						
Ampere-meters (MAm)	65.6	54	117.2	91.2	328	43
Energy Stored (MJ)	39	23.2	90	59.4	211.6	23
1990 18 Coil Design						
Ampere-meters (MAm)	85.5	116	183	---	384.5	51
Energy Stored (MJ)	72.5	57	123	---	252.5	28

The 18 coil design is developed to achieve a compact design with magnets as close as possible to the model. Four coils are mounted on each of the four tunnel walls, two in front and two in back. Since the lift force is much higher than the side force, the Z-coils are extended over the Y-coils, Fig. 3.5-3. The two X-coils are in their usual position. This configuration is more compact but still requires more ampere-meters than the 14 coil design. The outer cylindrical envelope of the tunnel with the 18 coil design is 3.04 m radius and 5.1 m long compared to 3.17 m and 6.6 m respectively for the 14 coil system.

In summary, the integrated design achievements shown in this study are:

1. A new analytical technique for designing MSBS. Magnets are utilized according to their available capacity in contrast to utilization primarily in the most efficient degree of freedom, as in the conventional design.

2. A demonstration of the applicability of the integrated design philosophy for two different configurations, one conventional and the other non-conventional.

3. Two MSBS designs composed entirely of simple solenoids. The first is a 14 coil design along the more conventional lines of a subset of coils for specific degrees of freedom, except that extra capacity from other coils is used as available. The second is an 18 coil design in which a symmetric set of coils is mounted as close as possible to the model in the most compact configuration. This system is tentatively preferred due to simplicity and compactness.

4. **<u>Appendix</u>**

* Subcontract with CeramPhysics Inc., W. W. Lawless, President.

A.1 EPOXY PROGRAM

A.1.0 BACKGROUND

The goal of this research is to explore the enthalpy-stabilization that can be achieved by adding ceramic powders to Formvar or epoxy for applications involving the commercial alloy superconductor NbTi. The ceramic powders here are chemically stable and have enormous specific heats below 10 K. As originally proposed, this program was to concentrate on spinel ceramics CCN(9/1) and CCN(1/0) developed by CeramPhysics, Inc. However, a third ceramic, SCIA, was later introduced into this program primarily because some limited data on an SCIA + epoxy composite were available from a previous Air Force sponsored program.[1]

(a)   (b)
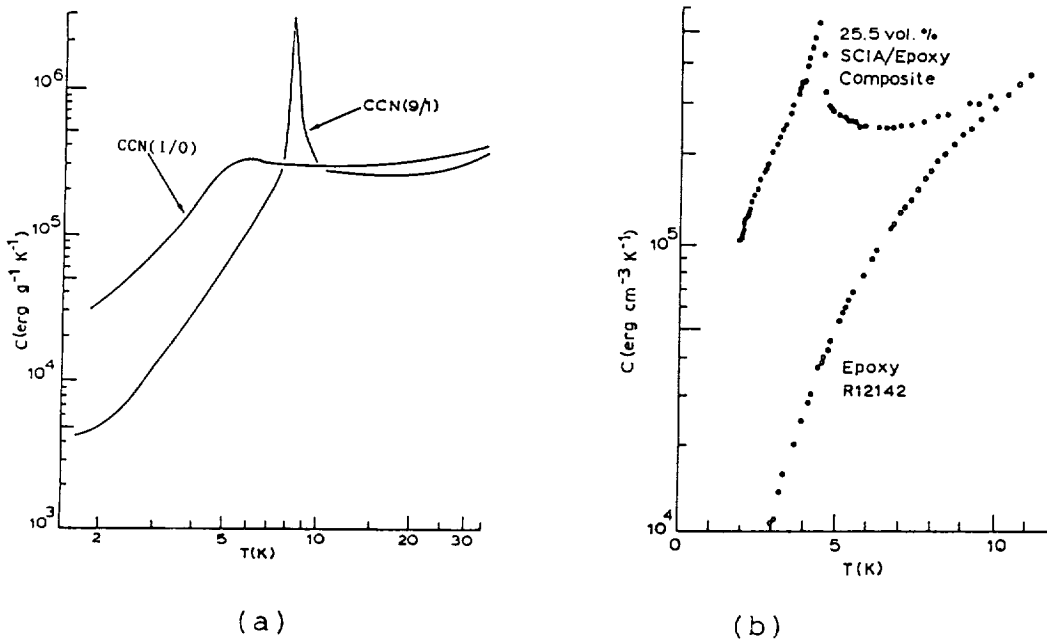
Figure A-1. Specific heat data for the three ceramics in this program: (a) CCN(1/0) and CCN(9/1); and (b) The SCIA ceramic, here in a 25.5 vol% epoxy composite.

Specific heat data for these three ceramics are shown in Fig. A-1 where the SCIA data in Fig. A-1 are for a 25 vol.% epoxy composite. To illustrate the enormity of these specific heat values, we note from Fig. A-1(a) that at about 6-7 K the CCN

ceramics have a specific heat $C \simeq 4 \times 10^5$ erg g^{-1} K$^{-1} \simeq 0.25$ J cm^{-3} K^{-1} using densities ~ 6 g/cm^3. For comparison, Pb at this temperature has a specific heat $C \simeq 0.02$ J cm^{-3} K^{-1} (note that the volumetric basis is the most demanding basis for comparing specific heats at low temperatures). Going further, the SCIA composite in Fig. A-1(b) has a specific heat maximum $C \simeq 0.3$ J cm^{-3} K^{-1} conveniently located at 4.3 K.

The research program here involved the fabrication of ceramic + epoxy composites by California Fine Wire Co. and the measurement of specific heat, thermal conductivity, and thermal contraction at low temperatures by CeramPhysics, Inc. In addition, CeramPhysics performed measurements of specific heat and magnetocaloric phenomena in intense magnetic fields on selected composites at the National Magnet Laboratory.

A convenient epoxy was selected by California Fine Wire for composite fabrication (Envirotex epoxy). The previous data for SCIA composites involved a different epoxy (R12142), and the ultimate dielectric insulation matrix will most probably be Formvar. Consequently, it is important to ask if the results obtained with one epoxy are transferrable to another epoxy or to Formvar.

Fortunately for this program, the low temperature properties of all amorphous materials are the same (e.g., epoxies, resins, glasses, etc.).[2] Therefore, for the purpose of fabricating and measuring ceramic/epoxy composites the only requirements for the epoxy are that it be available and workable, and the "Envirotex 1:1 Polymer Coating" satisfies these conditions. We can thus confidently move forward with the assurance that the results obtained with this epoxy are transferrable to any other amorphous-matrix materials.

As an illustration of the universality of the properties of amorphous solids at low temperatures, the specific heats of the two epoxies and of G.E. 7031 varnish are shown in Fig. A-2. As seen in Fig. A-2, these specific heats are essentially identical.

The specific heat of the Envirotex epoxy measured in this program is shown in Fig. A-2, and these data will be used below.
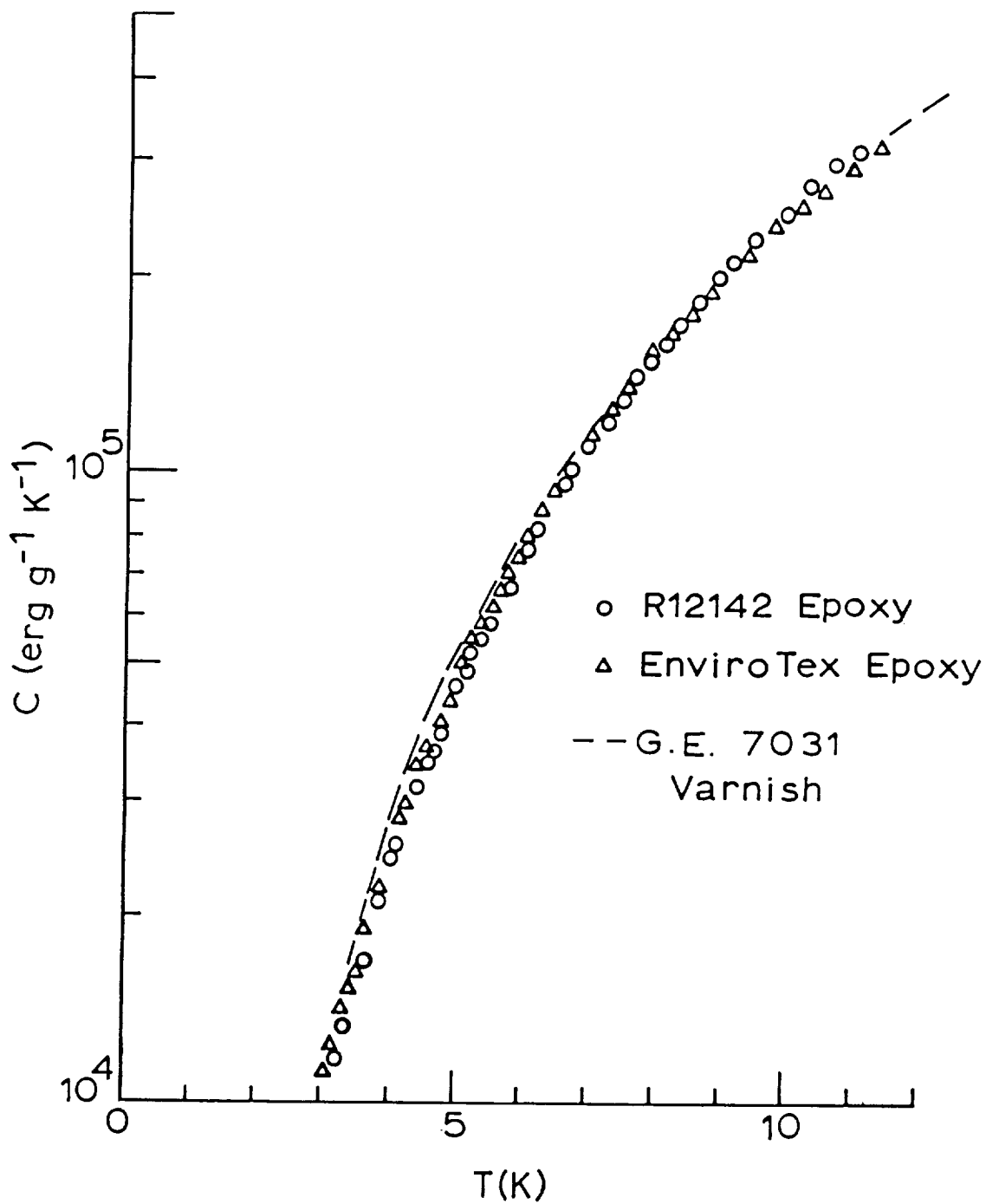
Figure A-2. Specific heats of two epoxies and of G.E. 7031 varnish illustrating the universality of the properties of amorphous solids at low temperatures.

Although this research is based primarily on specific heat considerations, the thermal conductivity of the composite can also play an important role, and it is worthwhile here to discuss the possible tradeoffs between specific heat (enthalpy) and thermal conductivity with regard to stabilizing heat transients in NbTi wire in, say, a magnet application.

First, it is recognized that a spectrum of thermal disturbances can arise in the NbTi wire, and the combination of wire insulation plus potting epoxy serve two complementary thermal roles: (1) To absorb thermal energy produced within the winding; and (2) To transmit this energy to the helium coolant.

At one extreme, if the volumetric specific heat of the dielectric system is large enough to absorb the maximum thermal disturbance with a minimal temperature rise, then stabilization is achieved regardless of the thermal conductivity of the dielectric system.

At the other extreme, if the thermal disturbance is so large that the enthalpy of the dielectric system is overwhelmed, then the specific heat becomes unimportant and the emphasis shifts to the thermal conductivity. In fact, in this case the specific heat should be as small as possible to maximize the thermal diffusivity.

There is an intermediate case for thermal disturbances shorter in time than the thermal relaxation time (the two cases above occur when the disturbance time is somewhat larger and much larger than the relaxation time, respectively). In this case, the important thermal parameter is[3]

$$\eta = \sqrt{\kappa C}, \tag{A-1}$$

where κ is the thermal conductivity and C is the volumetric specific heat of the dielectric system.

In view of the parameter η, κ and C are on an equal footing in the intermediate case.

The research on composites here is aimed at a recommendation(s) for a ceramic + epoxy system that optimizes the above

considerations, and the reporting of this research is organized along the following lines:

Experimental Methods

Measurements in Zero Magnetic Field

Measurements in Intense Magnetic Fields

Data Analyses

Conclusions and Recommendations

A.1.1 EXPERIMENTAL METHODS

Thermal Contraction

The method here is based on the availability of a General Radio 1620 Capacitance Measuring Assembly which has the capability of resolving capacitance values to six figures. Consequently, if one end of the test bar is silvered and brought into close contact with a metal plate, then a capacitor is formed by the silvered surface and the metal plate. As the test bar thermally contracts, the capacitance changes, and the purpose of the method is to relate this capacitance change to the thermal contraction coefficient.

The apparatus built for this measurement is shown schematically in Fig. A-3. Three high-purity copper rods are brazed into a mounting plate (only two rods are shown in Fig. A-3), and this plate bolts into a temperature-controlled reservoir post in a cryostat. The test bar also mounts on this plate, and the method involves measuring the difference in thermal contractions between the copper rods and the test bar (note that copper has the smaller thermal contraction, see below).

A Nylon screw is potted in the bottom of the test bar, as shown in Fig. A-3, and the test bar is mounted on the copper mounting plate with a Nylon nut. The thermal contraction of this Nylon screw insures that the test bar is always securely mounted.

The top end of the test bar is silvered, as shown, and a copper-electrode plate is positioned on top of the bar with mounting nuts. Nylon bushings and washers are used to electrically isolate the copper electrode, as shown. This assembly is done at room temperature, and there are two possible approaches for bringing the copper-electrode plate into close proximity with the silvered end of the test bar: (1) Gently resting the plate on the bar; or (2) Inserting a Teflon sheet, positioning the plate, then removing the sheet. The advantage of the former approach is that a larger signal is obtained, whereas the latter approach allows a capacitance-measurement check at room temperature before cooldown (see below).

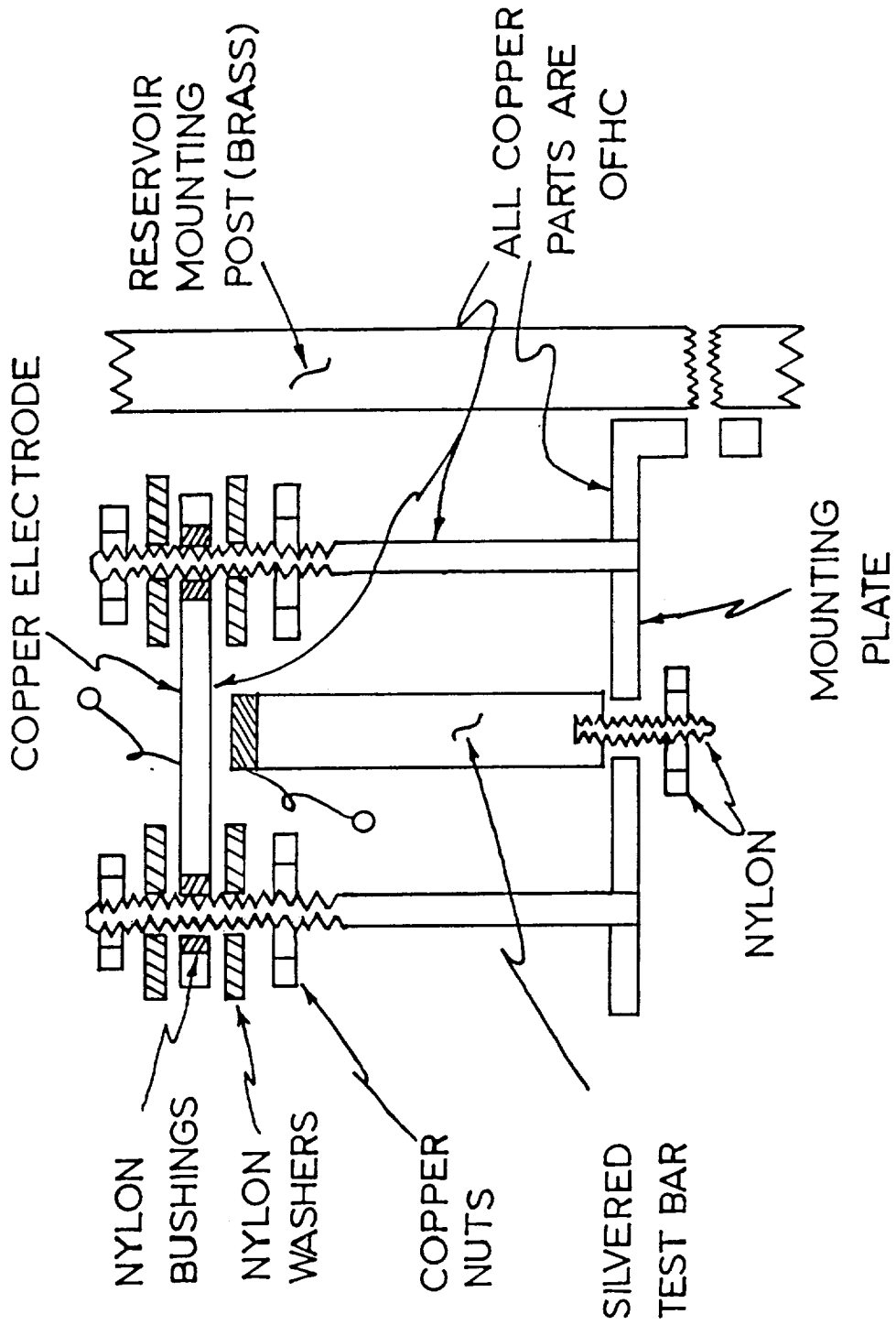Finally, all measurements are done in a hard vacuum to

Figure **A**-3. Test apparatus for measuring thermal contraction.

insure that the dielectric constant of the gap is unity. The reservoir mounting post in Fig. A-3 is temperature-controlled within an adiabatic shield and is outfitted with calibrated Ge and Pt thermometers. All hookup leads are coaxial cables to eliminate lead capacitance.

Next, we consider the theory of the method and estimate the experimental resolution obtainable. The starting point here is the capacitance of a plane-parallel capacitor where the plate area is $\underline{A}$ and the plate separation is $\underline{x}$,

$$C = 8.85 \times 10^{-2} \, \epsilon A/x \tag{A-2}$$

where ϵ is the dielectric constant of the medium in the gap, the capacitance C is in picofarads (pF), and A and x are in cm^2 and cm, respectively. We ignore any lead capacitance in Eq.(A-2); the lead capacitance is expected to be very small and can be easily measured in any case.

Define L_u and L_s as the room-temperature lengths of the test bar (unknown) and copper rods (standard), respectively, and let x_o be the gap separation at room temperature. Then from Eq.(A-2)

$$1/C_{293} = x_o/k \tag{A-3}$$

$$1/C_T = (x_o + \Delta L_u - \Delta L_s)/k \tag{A-4}$$

where $k = 8.85 \times 10^{-2} \epsilon A$ and T < 293 K. We note in Eq.(A-4) that ΔL_s is needed as a _positive_ quantity. Next, we write for ΔL_s

$$\Delta L_s = L_s (\Delta L/L)_s = L_s \, \phi(T) \tag{A-5}$$

where $\phi(T)$ is the NBS thermal contraction table for copper (see Table A-1 below).

Combining Eqs.(A-3)-(A-5), we have the desired result

$$\Delta L_u/L_u = (L_s/L_u) \, \phi(T) + (k/L_u)(1/C_T - 1/C_{293}) \tag{A-6}$$

A-8

Table A-1

Thermal Contraction of Copper
(c.f. NBS Monograph 29)

T(K)	$\phi(T) \times 10^5$
0	326
10	326
20	326
30	325
40	324
50	321
60	316
70	310
80	302
90	293
100	283
120	260
140	235
160	208
180	179
200	149
220	118
240	87
260	55
273	33
280	22
293	0

for the thermal contraction of the test bar, $\Delta L_u/L_u$.

We return here to the comments made above regarding the positioning of the electrode plate on the top of the test bar. In one case, $x_o = 0$ and $1/C_{293} = 0$; in the $x_o \neq 0$ case, however, the measurement of C_{293} provides a check on the setup according to Eq.(A-3).

Consider now a numerical example. We select a test bar of Araldite epoxy, 2.54 cm long and 0.64 x 0.64 cm^2 in cross section. Assume that a 0.013 cm gap has been achieved with a Teflon sheet, and let the copper rods be 2.54 cm long. For a hard vacuum $\varepsilon = 1.00$, and using the NBS tables for copper and Araldite we find that the capacitance changes from 2.81 pF at room temperature to 1.18 pF at 0 K. This is a very large capacitance change given the capability of the General Radio bridge, and so the method is feasible. For the case of a smaller gap, say, $x_o = 0.005$ cm, we find for the respective capacitances, 7.02 and 1.57 pF. Finally, for the case that $x_o = 0$, we find a capacitance of 25.0 pF at 280 K, 2.02 pF at 0 K.

The capacitance signals here are sufficiently large that the largest source of error will probably be the uncertainty in measuring L_u and L_s. Along this line we note that L_u can be independently measured very accurately (as can the area A), and in the case that $x_o = 0$, then $L_u = L_s$ and Eq.(A-6) simplifies to

$$\Delta L_u/L_u = \phi(T) + k/L_u C_T. \tag{A-7}$$

A test of this thermal contraction method was made from room-temperature to 77 K. Two samples were run simultaneously. An aluminum rod and a nylon bar were machined to convenient dimensions ($\sim$ 2 cm in length and .3 - .4 cm^2 in cross-section). Both samples were "off-the-shelf" items, so there was no knowledge of the source or exact composition of the materials.

Each piece was drilled and tapped for a nylon screw at the bottom end. This screw held each sample tightly to the bottom plate. A single sheet of cigarette paper was placed between the aluminum rod and the bottom copper plate in order to isolate the

sample electrically. The top face of the nylon was painted with an air-dry silver paste which adhered completely to the face even when the sample was plunged directly into liquid nitrogen. The paste was extended down the side of the sample where a small copper wire was attached using more paste. Electrical contact to the aluminum rod was made by drilling and tapping a small hole in the side of the rod and mechanically attaching a wire.

It turned out to be relatively easy to adjust the top copper plate close to the top sample face. The top plate was placed against the face and the screws holding the plate were placed in position. Slight turns of each of the lower screws then raised the top plate away from the sample ~ 0.001-.002". Shining a strong light through the gap allowed for any adjustment to ensure the plates were parallel. At 300°C (at the minimum gap distance) the capacitance readings were ~ 4.5 and 11 pF for the aluminum and nylon respectively.

Capacitance-temperature data was obtained every 25 K from liquid nitrogen temperatures to room temperature. For these samples, the capacitances dropped by 3.4 and 2.2 pF for the Aℓ and nylon respectively. The noise level was excellent and the capacitance of each sample could be read to ±.0002 pF for both samples over the entire temperature range.

After the initial run, the leads to each sample were cut at the sample but held in the same place with tape. Another run was then made over the entire temperature range to measure the lead-to-lead capacitances which were on the order of 0.2 -0.3 pF. There was a slight temperature dependence to the lead capacitance over the range 77-300 K (on the order of 0.05 pF).

The data for both samples are shown in Fig. A-4 and are within 10% of the handbook values as shown. It should be recalled that the exact composition of both samples is not known; however, most aluminum alloy samples and nylon samples should be close (±20%) to each other. It is thus possible that the differences in Fig. A-4 are due solely to sample differences. Certainly the fact that both are close to the table values and one is high and the other is low indicates that there are no
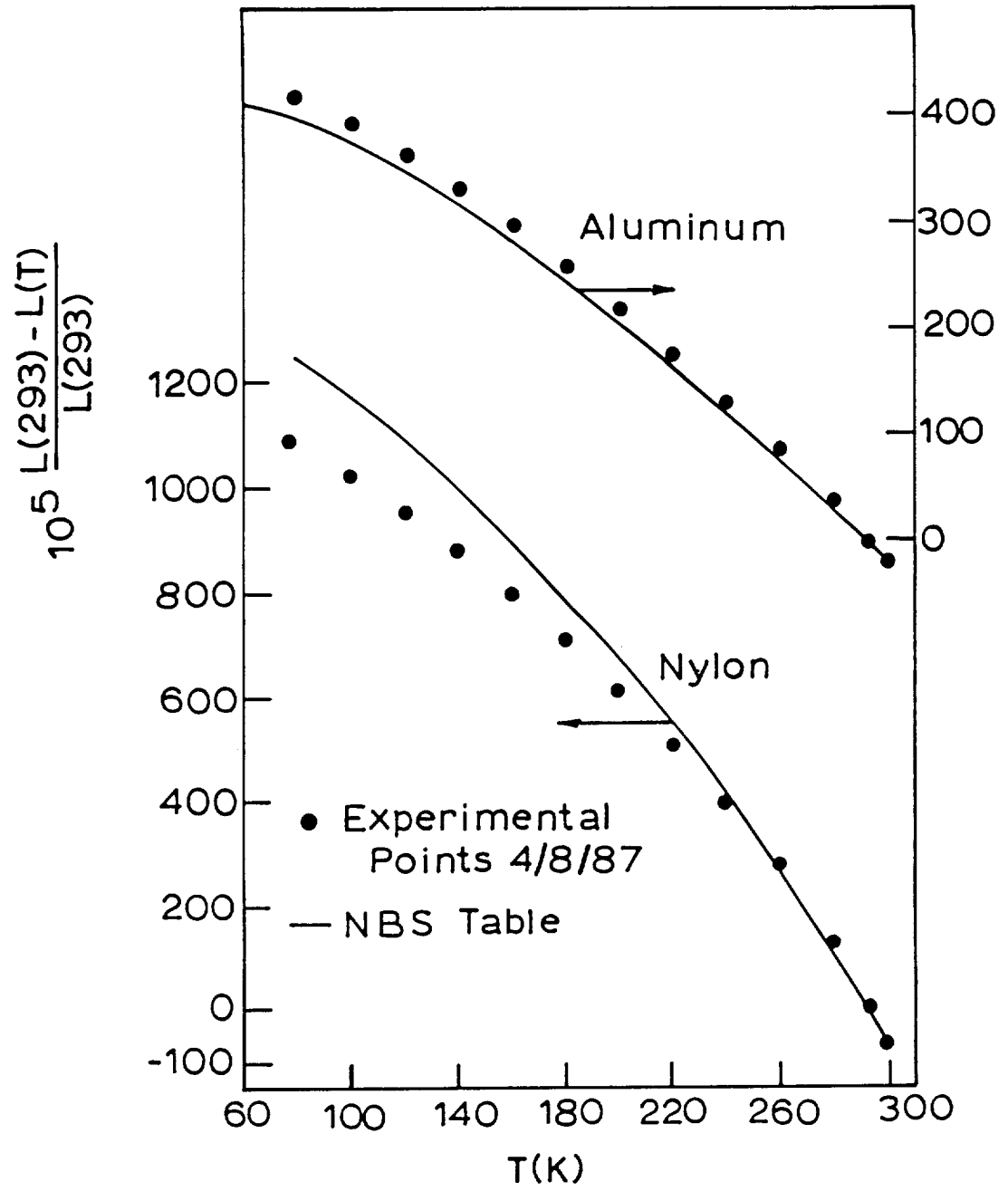
Figure A-4. Thermal contraction data measured on aluminum and nylon compared to the NBS Table data.

large systematic errors in the measurements.

An error calculation for the worst case (when the temperature is nearest the reference temperature) indicates an error of ~±2% for reading errors of dimensions and capacitances alone. This analysis does not take into account any possible systematic error (e.g., an error from the use of incorrect values for the length changes of the copper support rods). The rods are made of ETP (high purity) copper and the length changes are calculated using NBS tables for copper. The small calculated reading error is less than the size of an experimental point in Fig. A-4.

Specific Heat, Thermal Conductivity (Zero Magnetic Field)

The methods and apparatuses used for measuring specific heat and thermal conductivity at low temperatures in zero magnetic field have been documented.[4,5]

Measurements in Intense Magnetic Fields

The methods used by CeramPhysics for measuring specific heats in intense magnetic fields have been documented.[6]

The experimental methods for measuring magnetocaloric properties at low temperatures are not well documented in the literature or in reference books. Consequently, we will give a brief review of these methods here.

The experimental arrangement is shown schematically in Fig. A-5. The sample (1) is in the form of a disc having a groove wherein a thermometer element (2) is fixtured. A heater (7) is fixtured on the periphery of the disc, and the sample is suspended from a copper pin (3) by a mechanical link wire (4). A spiraled copper-wire thermal link (5) is also used if the sample has a large specific heat. Finally, the pin (3) is mounted into the reservoir (6).

The mechanical link (4) must be capable of supporting the sample under large magnetic forces during field ramping, and we have found that a 0.012-cm diam manganin wire wrapped around the sample through the groove as shown in Fig. A-5 will withstand ramp rates up to 20 T/min. Both the mechanical link (4) and the

thermal link (5) are indium-soldered
to the pin (3).

Experience with various thermo-
meters (2) has led us to use ground
220 Ω Allen-Bradley resistors below 30
K. These elements have the advantages
of small size (~ 10 mg), large sensiti-
vity, and simple measuring instrumenta-
tion; however, these elements have to
be calibrated in situ, and the magneto-
resistance effect must be calibrated.

Between 1.5-30 K, these thermo-
meter elements are described very
accurately by the equation[7]

$$\log R = A + BT^{-P}, \tag{A-8}$$

Figure A-5. Experimen-
tal arrangement for
magnetocaloric studies.

and in the case of magnetocaloric
measurements, the in situ calibrations
are done in zero field using a calibrated Ge thermometer mounted
in the reservoir. Our (unpublished) magnetoresistance
corrections established over several years for these elements are

$$\Delta A/A = -1.621 \times 10^{-3} + 4.269 \times 10^{-4} \, H - 2.874 \times 10^{-6} \, H^2$$
$$\Delta B/B = -2.205 \times 10^{-3} + 1.400 \times 10^{-3} \, H - 5.243 \times 10^{-6} \, H^2 \tag{A-9}$$
$$\Delta P/P = -4.085 \times 10^{-3} + 1.699 \times 10^{-3} \, H - 9.972 \times 10^{-6} \, H^2$$

where H is in kG. Here, $\Delta A/A = (A_H - A_0)/A_H$, etc.

The reservoir (6) in Fig. A-5 is temperature controlled
using a capacitance thermometer[8] mounted in the reservoir. This
is a very important feature because it is critical in magnetocal-
oric measurements to control the reservoir temperature very
precisely in the presence of intense and changing magnetic
fields, and the field-independence of the capacitance thermometer
makes this possible.

As we shall see below, the thermal links between the samples

and the reservoir have long time constants, yet the samples have to be brought into thermal equilibrium with the reservoir for calibrating the thermometer elements. However, this is easily accomplished by using both the temperature controller and the sample heaters; in fact, this is the primary reason for fixturing the heaters on the samples in these measurements. Another reason for having a sample heater is to pulse the sample for determining the thermal time constant of the copper-wire link (see below).

The thermal link between the sample and the reservoir plays a central role in these measurments and deserves careful consideration. The copper-wire thermal link is the dominant thermal link, and heat transfer by either gas conduction or radiation must be eliminated. This is accomplished by putting zeolites or charcoal granules in the bottom of the can to absorb He gas and by lining the can with aluminized Mylar (A two-can insert cannot be used due to space limitations in the magnet). Next, in the general case that power $\dot{Q}$ is supplied to the sample having a total heat capacity C and linked to the reservoir by a wire of thermal conductance G, the power balance equation is

$$\dot{Q} = C(dT/dt) + G(T-T_0) \tag{A-10}$$

where T_0 is the reservoir temperature. Equation (A-10) is valid provided the difference $T-T_0$ is small.

The solution to Eq.(A-10) is

$$T-T_0 = (T_m-T_0)e^{-t/\tau} \tag{A-11}$$

where the time constant τ is given by

$$\tau = C/G. \tag{A-12}$$

The solution Eq.(A-11) corresponds to the sample being heated from T_0 to T_m, and $t = 0$ is that time corresponding to $T = T_m$ [i.e., Eq.(A-11) describes the cooldown]. As we shall see below, Eq.(A-11) is used to determine τ from experimental time-tempera-

ture records from chart traces.

Solutions to Eq.(A-10) lead to an important correction factor. If the measured change in the sample temperature for a caloric event is ΔT_{meas} (e.g., for pulse heating, $\Delta T_{meas} = T_m - T_o$), the actual change, ΔT_{act}, is given by

$$\Delta T_{act} = \Delta T_{meas} (1 + \Delta t/2\tau) \qquad (A-13)$$

where Δt is the time duration of the caloric event (i.e., heating or cooling). Equation (A-13) reflects the fact that if $\Delta t \sim \tau$ then heat energy will flow between the sample and the reservoir during Δt, and the measured ΔT will be reduced.

Consequently, one wishes to make τ large compared to Δt to avoid the correction, Eq.(A-13), but Eq.(A-12) shows that $\tau \propto T^2$ (i.e., $C \propto T^3$, $G \propto T$). Therefore, to achieve a large τ at, say, 2 K carries the penalty of very large τ-values at higher temperatures and hence long cooldown periods (Note that He exchange gas cannot be used).

It has been our experience that for $\tau \sim 10^2$ s at 4 K, an overnight helium cooldown will bring the samples to 4 K from room temperature. In any case, τ is always determined experimentally at helium temperatures to see if the correction Eq.(A-13) is necessary.

The use of a copper-spiral thermal link adds a complicating feature -- namely, the thermal conductance G of this type of link changes in a magnetic field (in contrast to a manganin link). Moreover, the spiral contains segments which are both transverse and longitudinal to the magnetic field. Fortunately, the transverse and longitudinal magneto-thermal-conductivity of this copper wire have been measured,[9] and the effect of a field is to decrease G and therefore to increase τ according to Eq.(A-12). The measured data[9] for the longitudinal and transverse magnetothermal conductivities of the copper wire used here are reproduced in Fig. A-6.
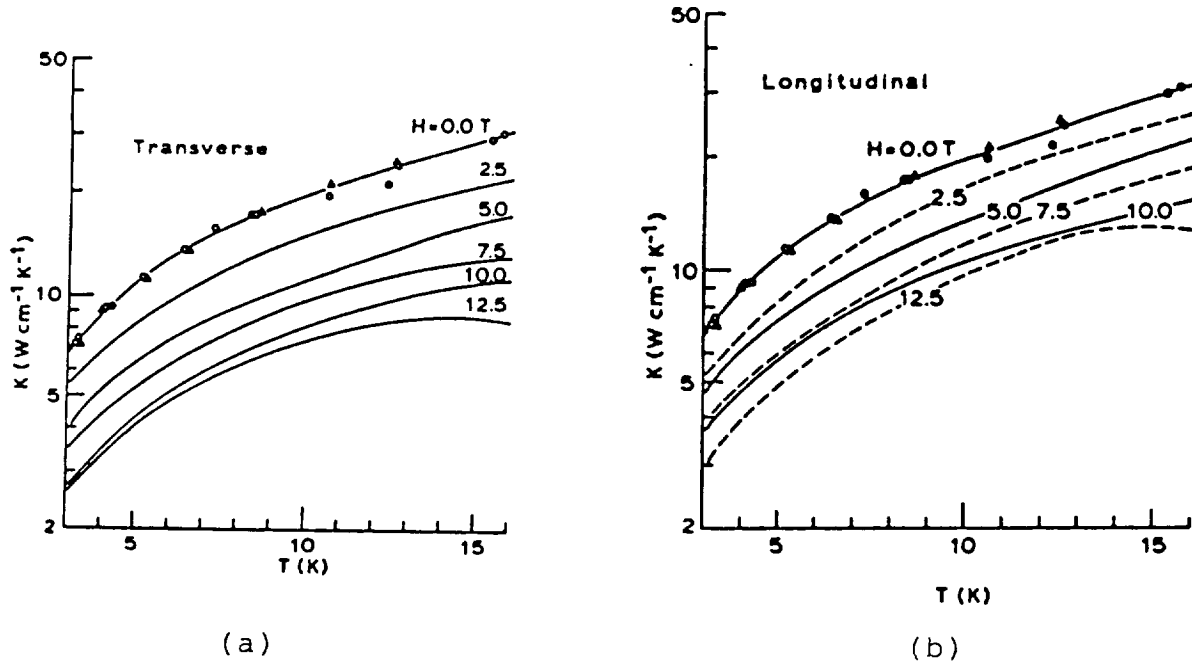
(a)

(b)

Figure A-6. Transverse (a) and longitudinal (b) magnetothermal conductivity data[9] measured on the copper wire used in the magnetocaloric measurements.

Neglecting the anisotropy of the magnetothermal data in Fig. A-6 for convenience, we have from the Wiedemann-Franz law (i.e., $k\rho/T = L$) that

$$1/K \simeq 1/K_0(1 + kH), \tag{A-14}$$

and since $G \propto K$, we have from Eq.(3-11)

$$\tau_H = \tau_0(1 + kH). \tag{A-15}$$

Since linear ramps were used, $H = rt$, we have for the mean value of τ

$$\tau_H = \langle\tau\rangle = \frac{1}{\Delta t} \int_0^{\Delta t} \tau \, dt = \tau_0(1 + \frac{1}{2}kr\Delta t) \tag{A-16}$$

Recognizing that $r\Delta t = H$, we have the final result

$$\tau_H = \tau_0(1 + \frac{1}{2}kH) \tag{A-17}$$

A-17

We have neglected the field dependence of the heat capacity C entering Eq.(A-12) because experience with these ceramics in question has shown that this is a small effect.

Returning to the data in Fig. A-6, we find for the field coefficient k in Eq.(A-13) that k(transverse) = 0.179 and k(longitudinal) = 0.138 (H in Tesla). Tight spirals of the copper link (5) in Fig. A-5 are always used so that the transverse magnetothermal conductance dominates, and we adopt

$$k \approx 0.179 \ T^{-1} \qquad\qquad (A-18)$$

Finally, there is another correction factor to the ΔT_{meas} in any caloric event. Namely, the _addenda_ fixtured to the sample (e.g., thermometer, heater, etc.) are also heated or cooled in the event so that

$$\Delta T_{act} = \Delta T_{meas} \ (1 + C_a/C_s) \qquad\qquad (A-19)$$

where C_a is the heat capacity of the addenda and C_s is the heat capacity of the sample (including the addenda). Equation (A-19) shows that a premium is placed on minimizing C_a, and for this reason we use the suspended-sample technique shown in Fig. A-5 rather than using a sample holder (note in this regard that if a copper sample holder were used, special attention would have to be paid to eddy-current heating in the holder during field ramping).

Collecting Eqs.(A-13) and (A-19), we have the final result

$$\Delta T_{act} = \Delta T_{meas} \ (1 + C_a/C_s)(1 + \Delta t/2\tau_H) \qquad\qquad (A-20)$$

where τ_H is given by the mean-value theorem, Eq.(A-17).

Hysteretic phenomena may be involved in magnetocaloric heating/cooling. We define ΔT_r and ΔT_h as the reversible and hysteretic components, respectively, and we assume that ΔT_h is the same in sign and magnitude on both up-ramp and down-ramp. Then it is straightforward to show that

$$\Delta T_h = \frac{1}{2}(\Delta T_{up} + \Delta T_{down})$$

$$\Delta T_r = \Delta T_{up} - \Delta T_h = \Delta T_h - \Delta T_{down}$$

where by definition, $\Delta T_h > 0$.

In the experiments reported here, a water-cooled Bitter magnet at the Nat'l Magnet Laboratory (MIT) was used because, in contrast to a superconducting magnet, this type of magnet can be ramped $0 \rightarrow 10$ T in 30 sec [i.e., short Δt in Eq.(A-20)]. Our experiments consisted primarily of ramping $0 \rightarrow H \rightarrow 0$ and measuring the associated ΔT's of the samples on millivolt chart recorders. Four-lead, dc potentiometric methods were used for measuring the three thermometer voltages, and typically for a 25 mV signal, 20 mV were bucked using a potentiometer and 5 mV were displayed on the chart recorder.

A.1.2 MEASUREMENTS IN ZERO MAGNETIC FIELD

In this section we document measurements in zero field of specific heat, thermal conductivity, and thermal contraction on all the composites studied.

Densities were measured on all the composites and these density data are summarized here in Table A-2. The Envirotex epoxy has a density of 1.086 g/cm^3, and the CCN(9/1) and CCN(1/0) ceramics both have a density of 5.862 g/cm^3. The R12142 epoxy has a density of 1.178 g/cm^3, and the SCIA ceramic has a density of 5.163 g/cm^3. All composites were fabricated using these densities (e.g., to achieve a 40 vol.% level of ceramic powder), and the porosity levels in Table A-2 were calulated based on these densities.

Table A-2
Densities and Porosites of Composites

Ceramic Powder	Epoxy	Nominal Ceramic vol.%	Density g/cm^3	Porosity
CCN(1/0)	Envirotex	30%	2.154	17.1%
		40	2.500	20.0
		50	3.179	9.34
CCN(9/1)	Envirotex	30%	1.990	26.7%
		40	2.479	21.0
		50	3.167	9.76
SCIA	R12142	25.5%	2.104	4.11%
	Envirotex	40	2.592	4.60

The density data in Table A-2 reveal two significant trends: (1) For both CCN powders, the porosity levels drop sharply in going from 40 to 50 vol.%; and (2) The SCIA powder mixes into both the R12142 and Envirotex epoxies with resultant small porosities.

Thermal Contraction

Thermal contraction data measured on bars of the composites are shown in Fig. A-7 for the CCN(1/0) composites, in Fig. A-8
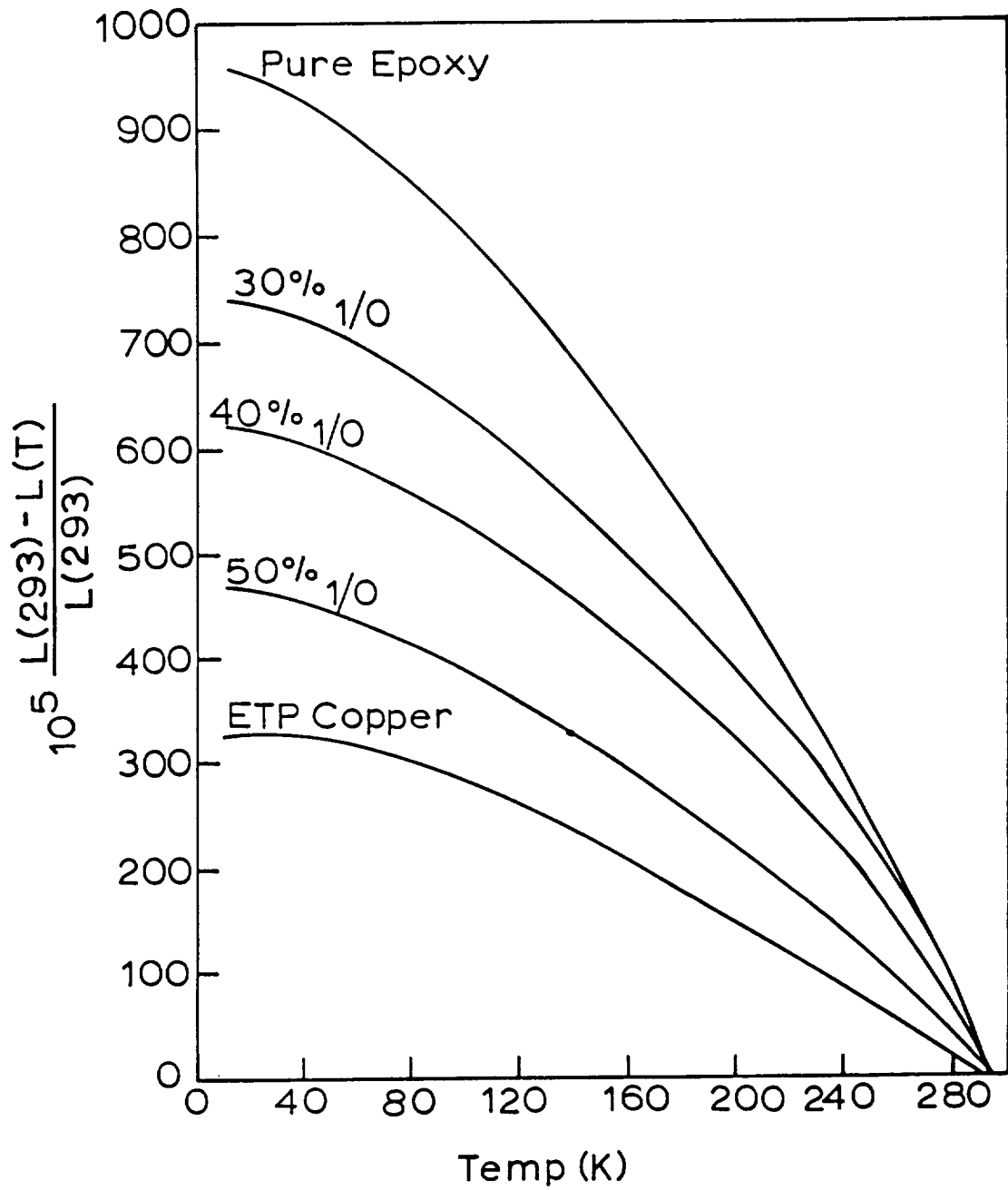
Figure **A-7**. Thermal contraction data measured on the CCN(1/0) - Envirotex composites compared to the pure epoxy and to copper.
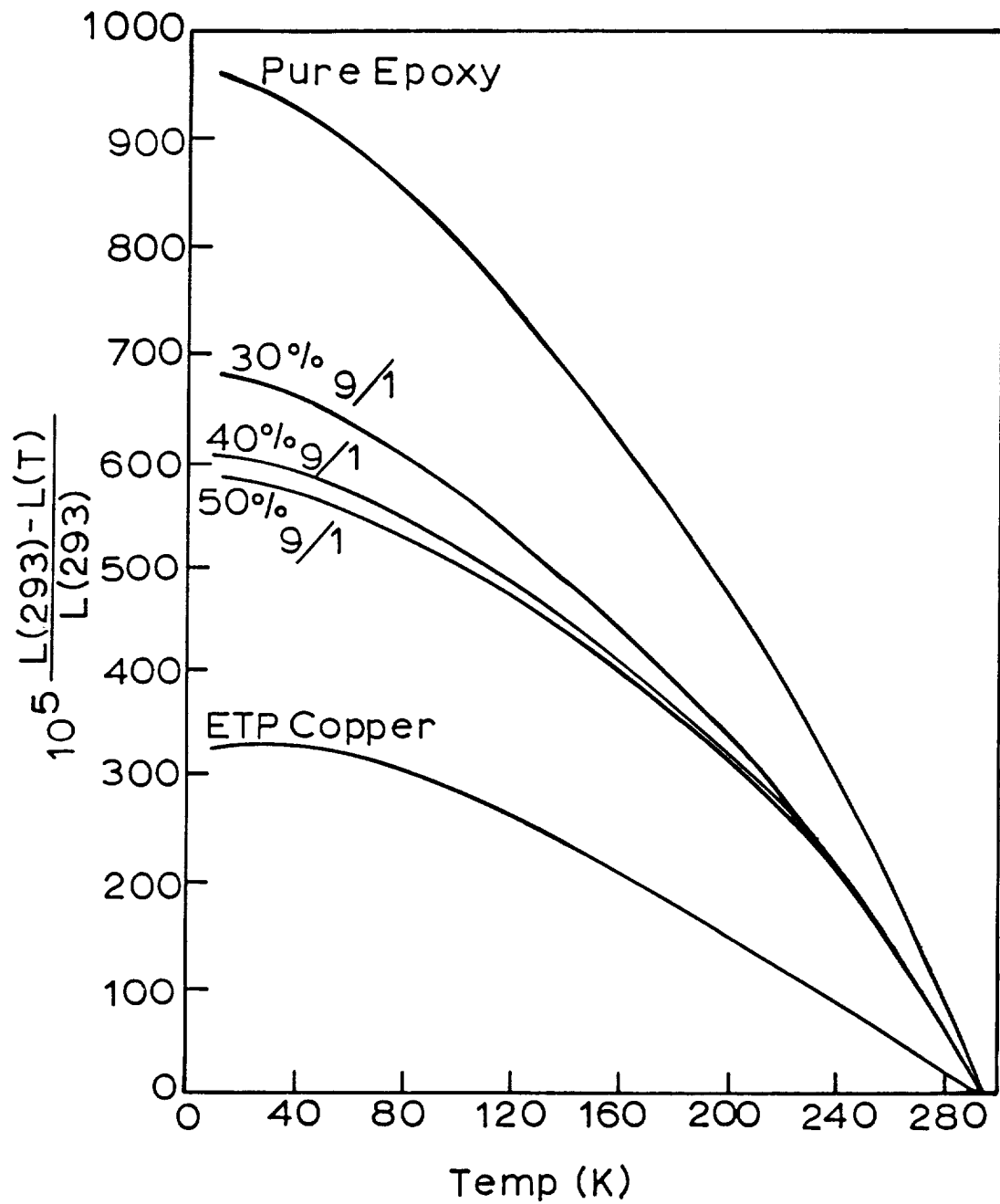
Figure **A-8**. Thermal contraction data measured on the CCN(9/1) - Envirotex composites compared to the pure epoxy and to copper.
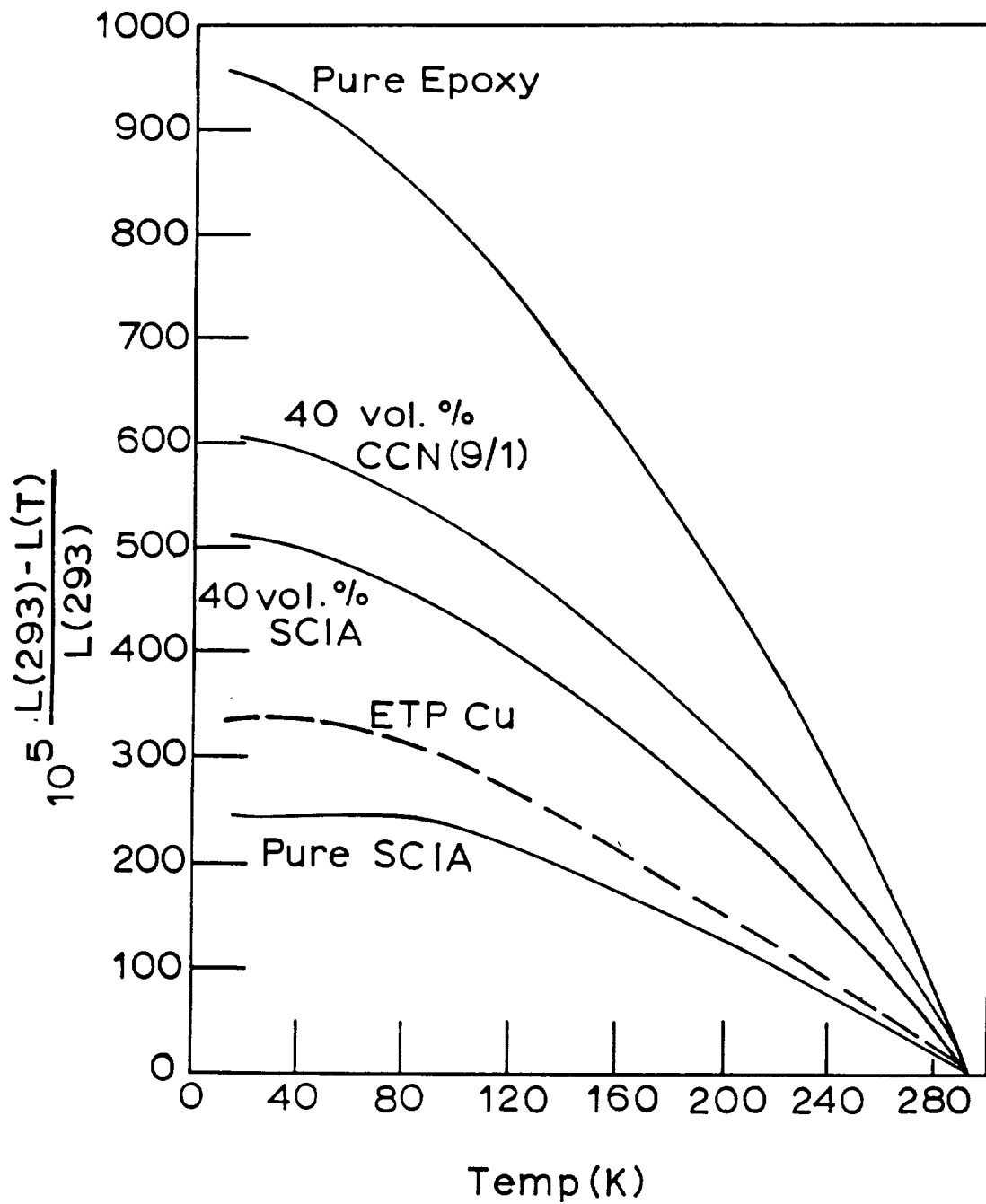
Figure **A**-9. Thermal contraction data measured on the 40 vol.% SCIA composite compared to pure epoxy, copper, pure SCIA, and the 40 vol.% CCN(9/1) composite.

for the CCN(9/1) composites, and in Fig. A-9 for the single 40 vol.% SCIA composite. The Envirotex epoxy is the matrix in all these composites, and contraction data measured on this epoxy are also shown in the figures. For comparison, all figures show the contraction of pure (ETP) copper taken from the NBS Table.

The contraction data for the 40% vol.% SCIA composite with Envirotex epoxy are compared to the data for the 40% vol.% CCN(9/1) composite in Fig. A-9, and this one-to-one comparison shows that the former composite has ~ 20% smaller contraction than the latter composite. The data in Fig. A-9 also show that the contraction curve for copper lies midway between those for pure SCIA and the 40 vol.% SCIA composite.

On comparing the contraction data in Figs. A-7 and A-8 for the CCN composites, it is seen that the data for the CCN(9/1) case appear to saturate because there is little difference between the 40 and 50 vol.% cases, whereas for the CCN(1/0) case there is a steady depression of the curves with increasing powder content.

It is interesting to notice that the 40% SCIA curve in Fig. A-9 and the 50% CCN(1/0) curve in Fig. A-7 nearly coincide. Therefore, we might speculate that if the steady depression of the contraction curves seen in Fig. A-7 for CCN(1/0) were to apply to the SCIA case also, then at about 50 vol.% SCIA a good contraction match to copper might be achieved. Unfortunately, the resources in the present program do not allow a check on this conjecture.

The thermal contraction data measured on all these composites are summarized in Tables A-3 and A-4.

Specific Heat

All specific heat data reported here are given on a volumetric basis using the density data in Table A-2 because this is the more meaningful basis for comparison and for enthalpy estimates.

The contribution of the addenda to the specific heat was computed in all cases during data reduction. For the composites,

Table A-3
Thermal Contraction, CCN(1/0) Composites
$\Delta L/L \times 10^5$

T(K)	0%*	30 vol.%	40 vol.%	50 vol.%
12.8	953	–	–	467
13.5	–	739	–	–
16.9	–	–	621	–
20	948	736	619	464
40	926	721	605	452
60	894	699	585	435
77	859	672	564	418
80	852	667	560	414
100	801	633	527	389
120	744	594	493	361
140	680	549	456	330
160	612	500	416	297
180	540	446	373	261
200	462	384	327	223
220	382	324	291	186
240	291	270	235	142
260	190	195	161	93
273	119	130	104	59
280	78	88	70	39
293	0	0	0	0

*Pure Epoxy (Envirotex)

Table A-4
Thermal Contraction, CCN(9/1) and SCIA Composites
$$\Delta L/L \times 10^5$$

T(K)	0%*	30 vol.%[a]	40 vol.%[a]	50 vol.%[a]	40 vol.%[b]
12.8	953	–	–	585	–
13.5	–	680	–	–	–
14.6	–	–	–	–	509
17.5	–	–	603	–	–
20	948	676	602	582	508
40	926	660	590	569	498
60	894	637	571	551	481
77	859	610	551	532	462
80	852	605	547	528	458
100	801	570	516	499	430
120	744	532	482	468	400
140	680	488	444	433	366
160	612	439	404	396	329
180	540	384	361	356	298
200	462	321	315	314	249
220	382	259	278	279	203
240	291	206	223	226	154
260	190	136	153	156	103
273	119	84	98	100	66
280	78	55	65	67	44
293	0	0	0	0	0

*Pure Epoxy (Envirotex)

*CCN(9/1) Composites

*SCIA Composite

this contribution was less than 1.8%. However, in the case of the pure Envirotex epoxy sample, the addenda contribution varied up to 4.1% -- in any case, these are small corrections using literature data for the addenda components.

Volumetric specific heat data for the 30, 40, and 50 vol.% composites of CCN(9/1) and CCN(1/0) are shown in Figs. A-10 and A-11, respectively. Also shown for comparison are specific heat data for the pure EnviroTex epoxy. The ceramic powder additions dramatically increase the specific heat for both powders (note logarithmic scales). For example, at about 8-9 K the specific heat improvement is an order of magnitude in both cases.

Knowing the specific heat of the pure EnviroTex epoxy allows estimates of the specific heats of the powders in these epoxies, and these separated powder data are shown in Fig. A-12. As seen, the powder data for all the composites for both ceramics agree very well, and this result shows that the fabrication of the composites was done very carefully. Of prime importance, however, these data clearly show that the specific heats are additive in these composites and that no adverse chemical reactions take place between the ceramic powders and the epoxy matrix.

Also shown in Fig. A-12 are "Bulk Ceramic" data for the CCN(9/1) and CCN(1/0) ceramics. The results here for the CCN(9/1) ceramic are not particularly surprising -- the sharp specific heat maximum in the bulk is fine-particle-size-broadened into a broad specific heat maximum. However, for the CCN(1/0) ceramic the broad, featureless specific heat behavior in the bulk ceramic is compressed into a specific heat maximum. We interpret this unusual behavior as arising from the compressive stress exerted on the CCN(1/0) grains by the higher-thermal-contraction epoxy phase (i.e., see Fig. A-7).

As a result of this compressive effect, the specific heats of the CCN(9/1) and CCN(1/0) powders in these composites are brought into commensuration, and this effect is shown graphically in Fig. A-13 where data for the 50 vol.% composites are plotted side by side. The 50% CCN(1/0) composite has the higher overall
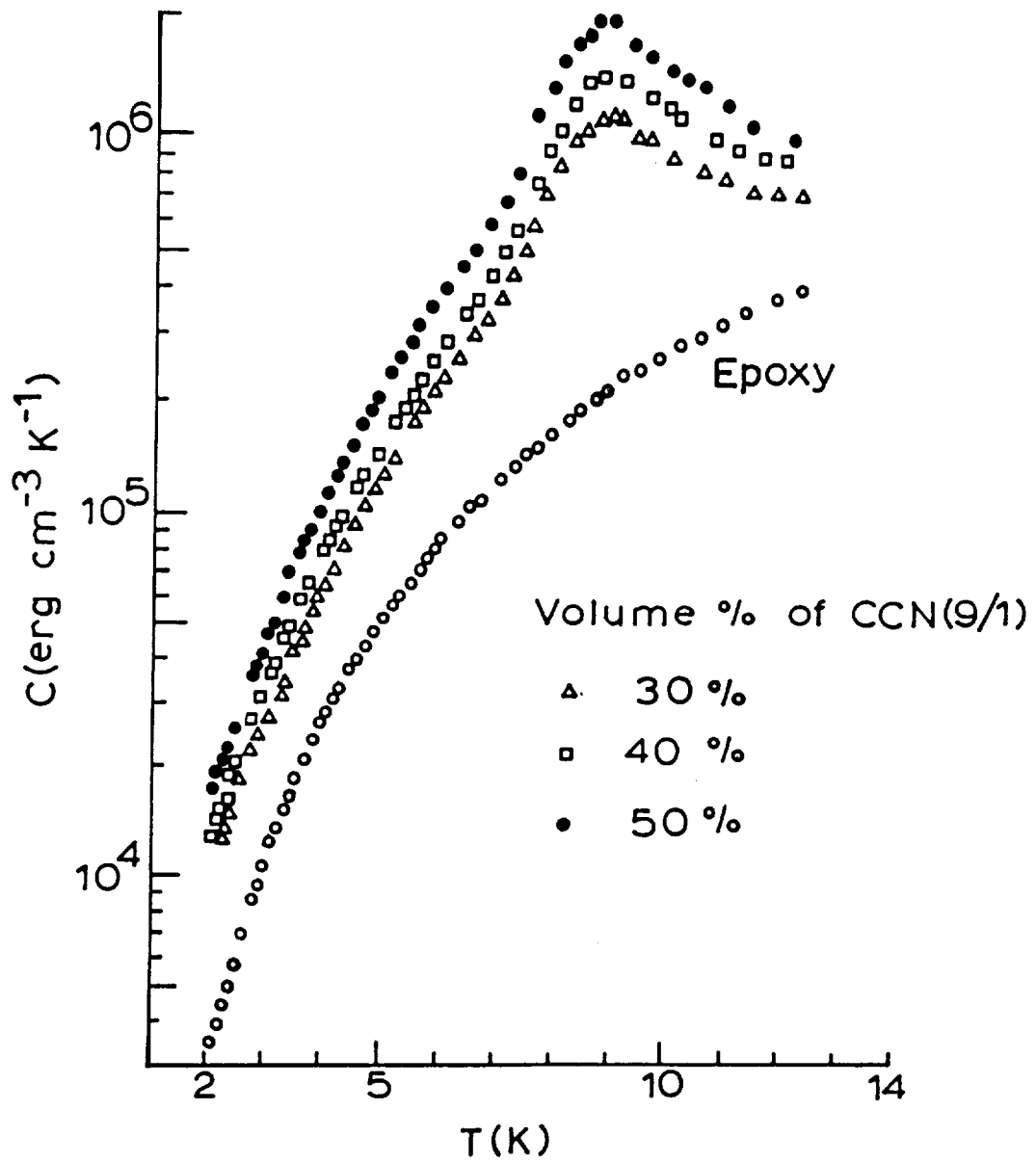
Figure A-10. Volumetric specific heat data measured on the CCN(9/1) composites and on the Envirotex epoxy.
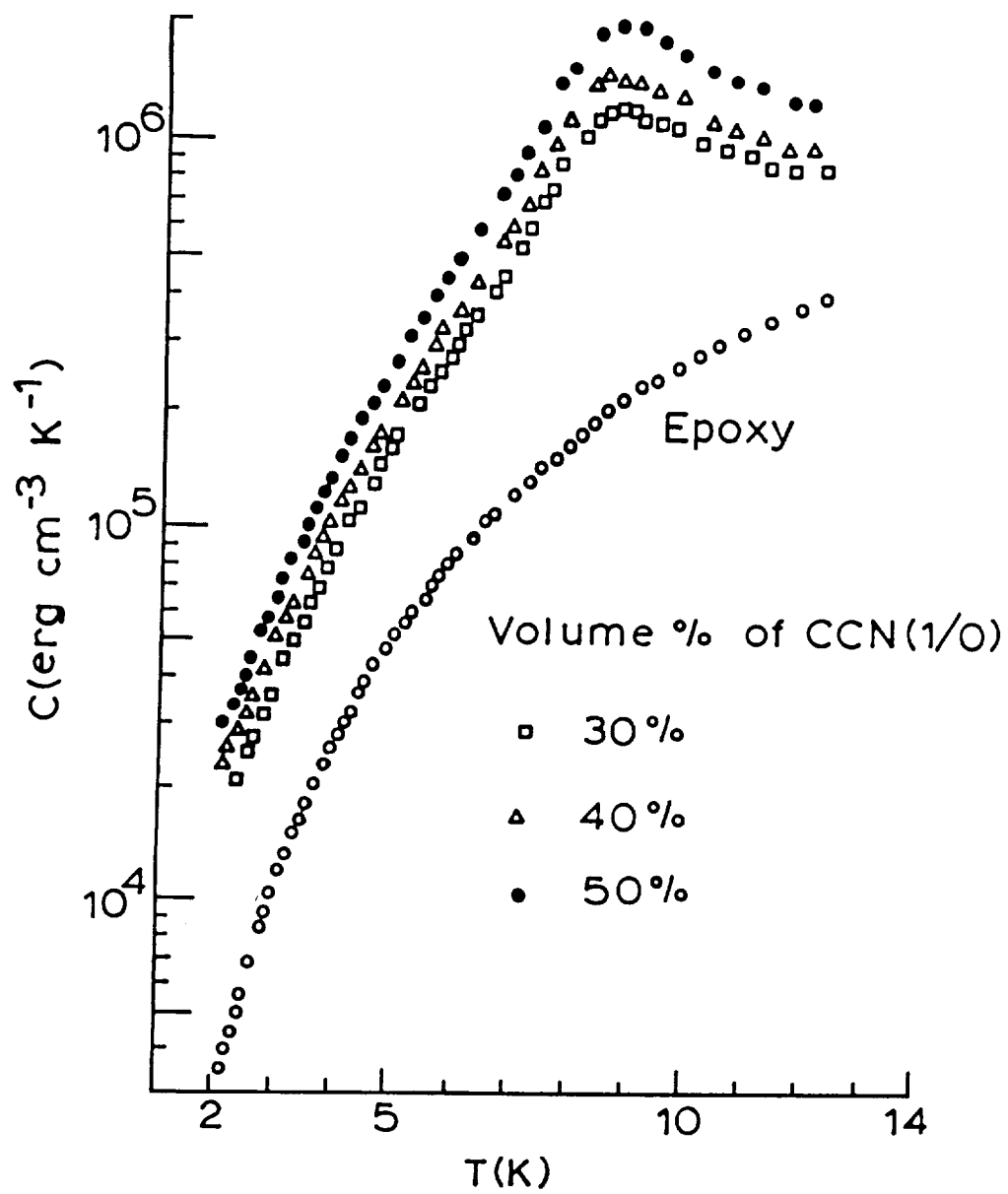
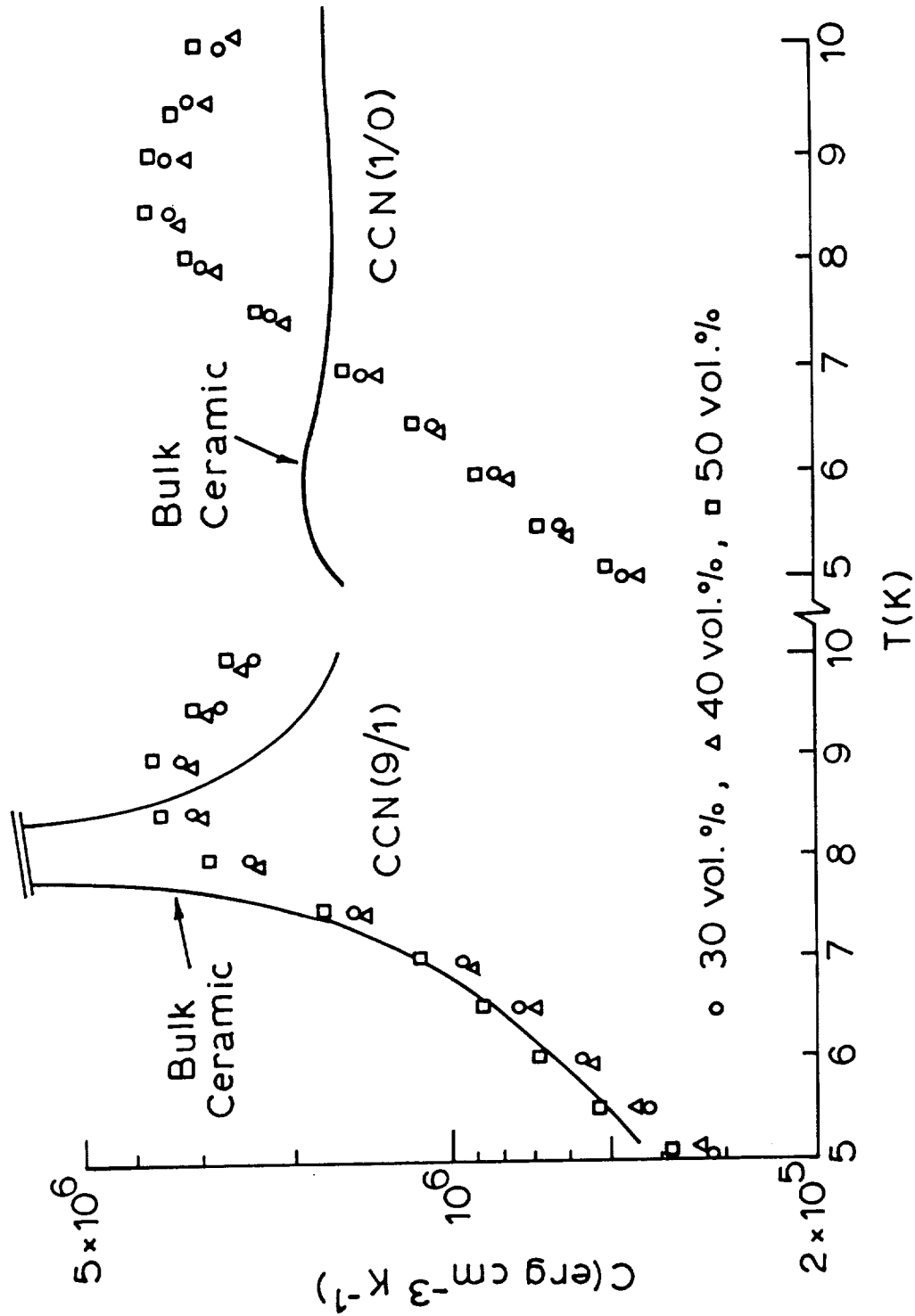Figure A-11. Volumetric specific heat data measured on the CCN(1/0) composites and on the Envirotex epoxy.

Figure A-12. Specific heat data for the CCN powders in the composites. The good agreement between the respective powder data indicates that the powder additions are additive.
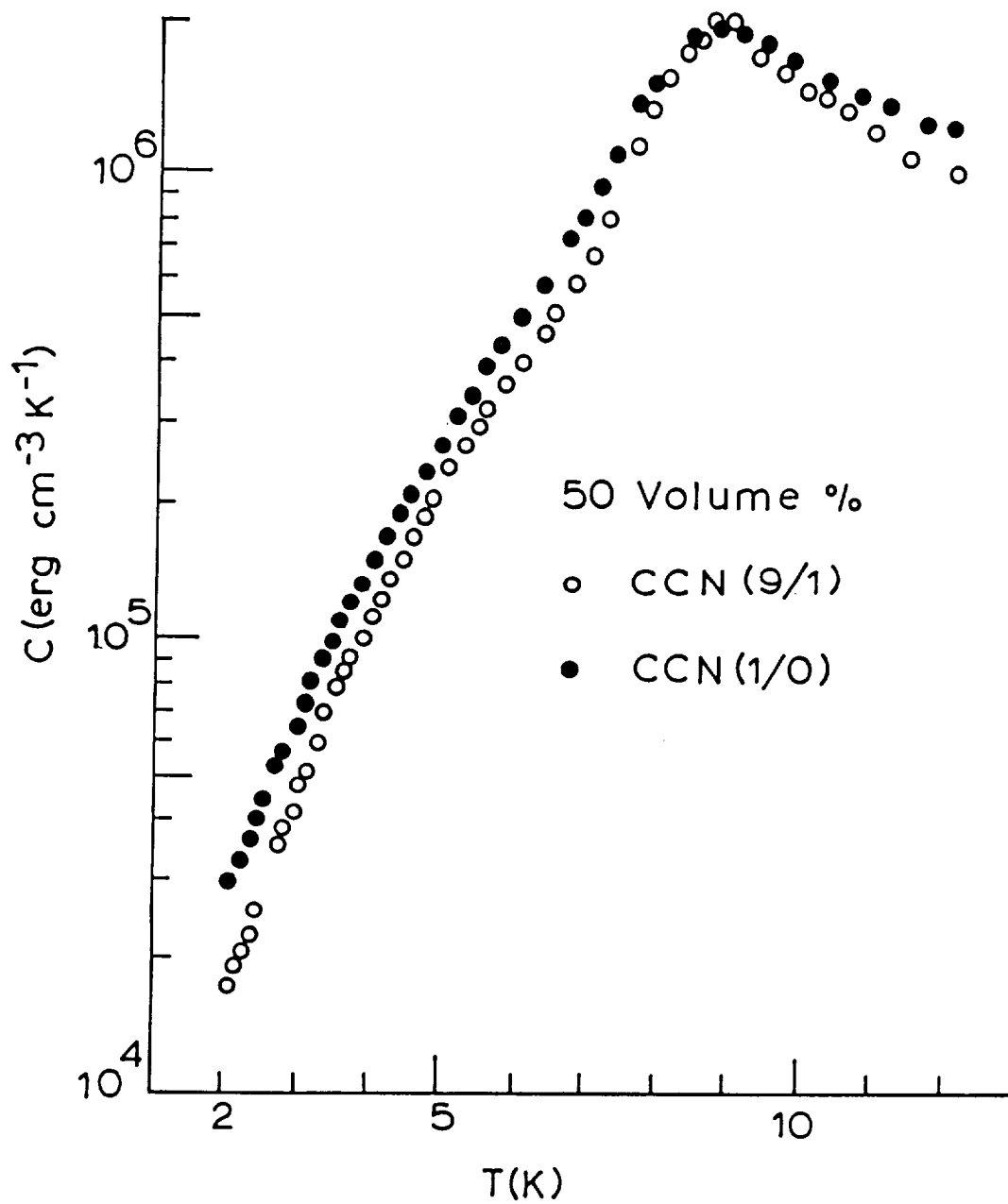
Figure A-13. Separated specific heat data for the CCN(9/1) and CCN(1/0) powders in the 50% composites.

specific heat. We remark that this compressive effect on the CCN(1/0) grains was totally unexpected.

The previously measured data[1] for the SCIA/epoxy composite are shown in Fig. A-14. These data are also plotted volumetrically, and we remind the reader that the epoxy here is R12142 rather than the EnviroTex epoxy. The ceramic powder loading here was 25.5 vol.%, and the composite in Fig. A-14 has a sharp maximum in the specific heat at 4.33 K. Volumetric data for the pure R12142 epoxy are also shown in Fig. A-14.

Volumetric specific heat data for the 40 vol.% SCIA composite with Envirotex epoxy are shown in Fig. A-15. As with the 25.5% composite in Fig. A-14, there is a sharp maximum at 4.35 K in Fig. A-15 for this 40% composite. Volumetric data for the Envirotex epoxy are also shown in Fig. A-15 for comparison.

It is important for this program to determine if the SCIA ceramic powder enters the epoxy matrix in an _additive_ fashion regarding the specific heat; this property has been demonstrated above in Fig. A-12 for the CCN powders. In Fig. A-16 are shown separated specific heat data for the SCIA powders in the two composites in the neighborhood of the specific heat maxima, and the agreement between these powder data is excellent. It is particularly significant that _two_ different epoxies are involved in the Fig. A-16 data, thus demonstrating clearly the additive nature of these specific heats.

Finally, we wish to compare the volumetric specific heats of equivalent composites of CCN and SCIA in the important temperature range above 4.2 K. For this comparison we select 40 vol.% powder composites, and we select the CCN(1/0) powder because from Fig. A-13 this powder addition has a larger specific heat than the CCN(9/1) powder addition. This comparison of 40% composites of CCN(1/0) and SCIA is shown in Fig. A-17 and shows that on a one-to-one comparison basis the SCIA composite has the _larger_ specific heat up to 6 K. Moreover, since the specific heats of these powders in the epoxy composites have been shown to be additive, we can definitely state that for _equivalent_ vol.%'s the SCIA composites will always have the _larger_ specific heats up
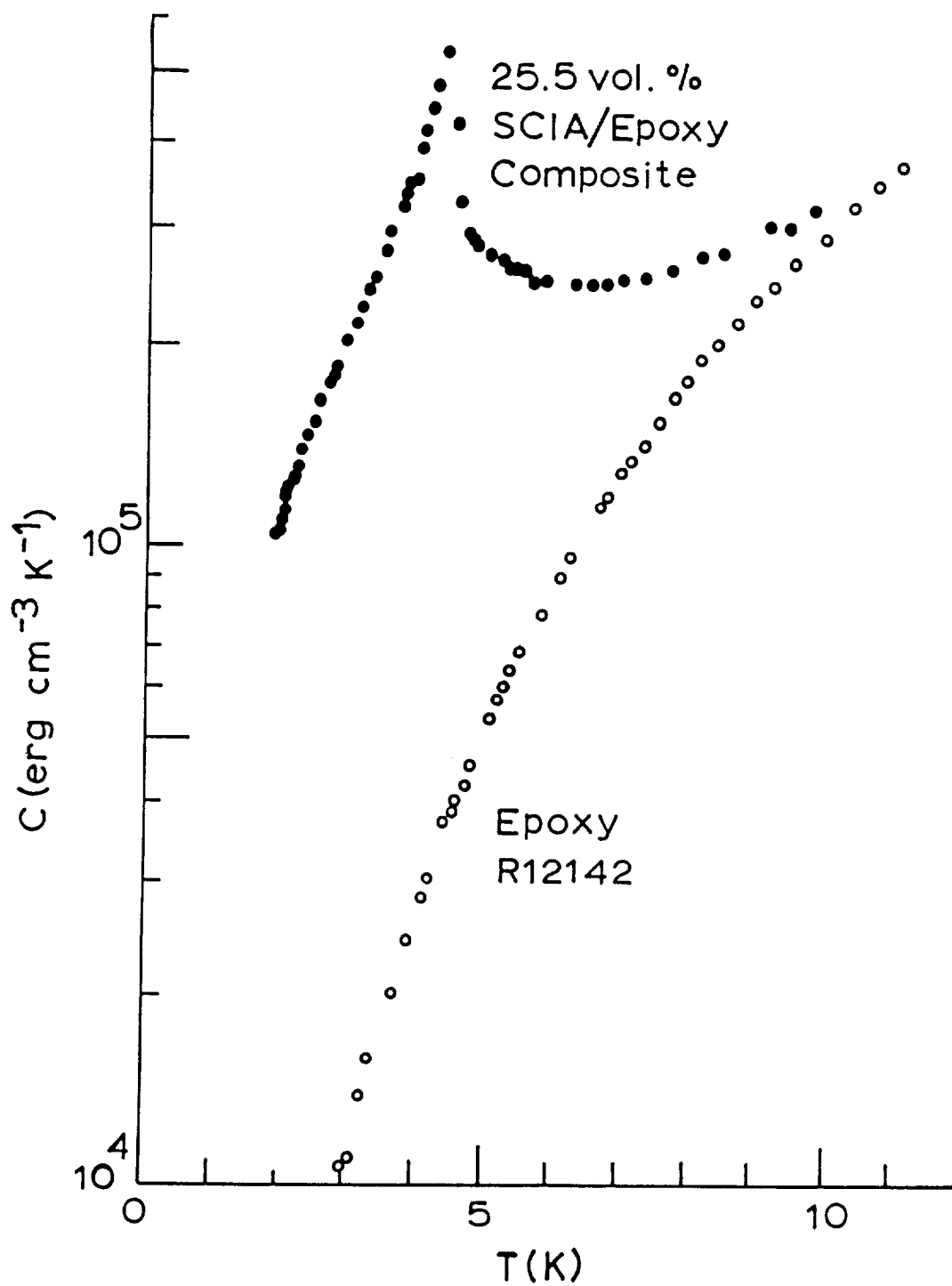
Figure **A-14**. Volumetric specific heat data for a 25.5 vol.% SCIA composite
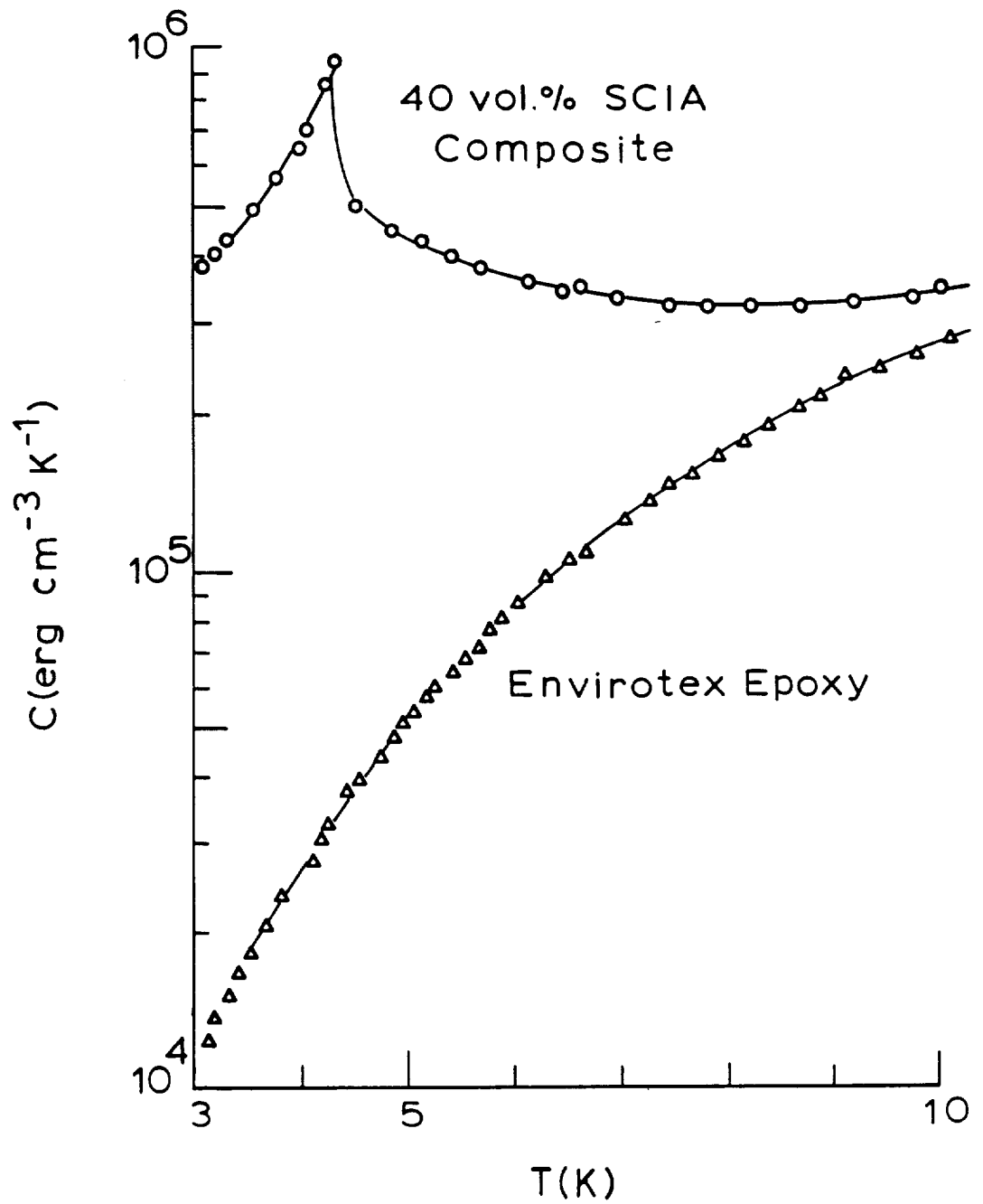with R12142 epoxy.

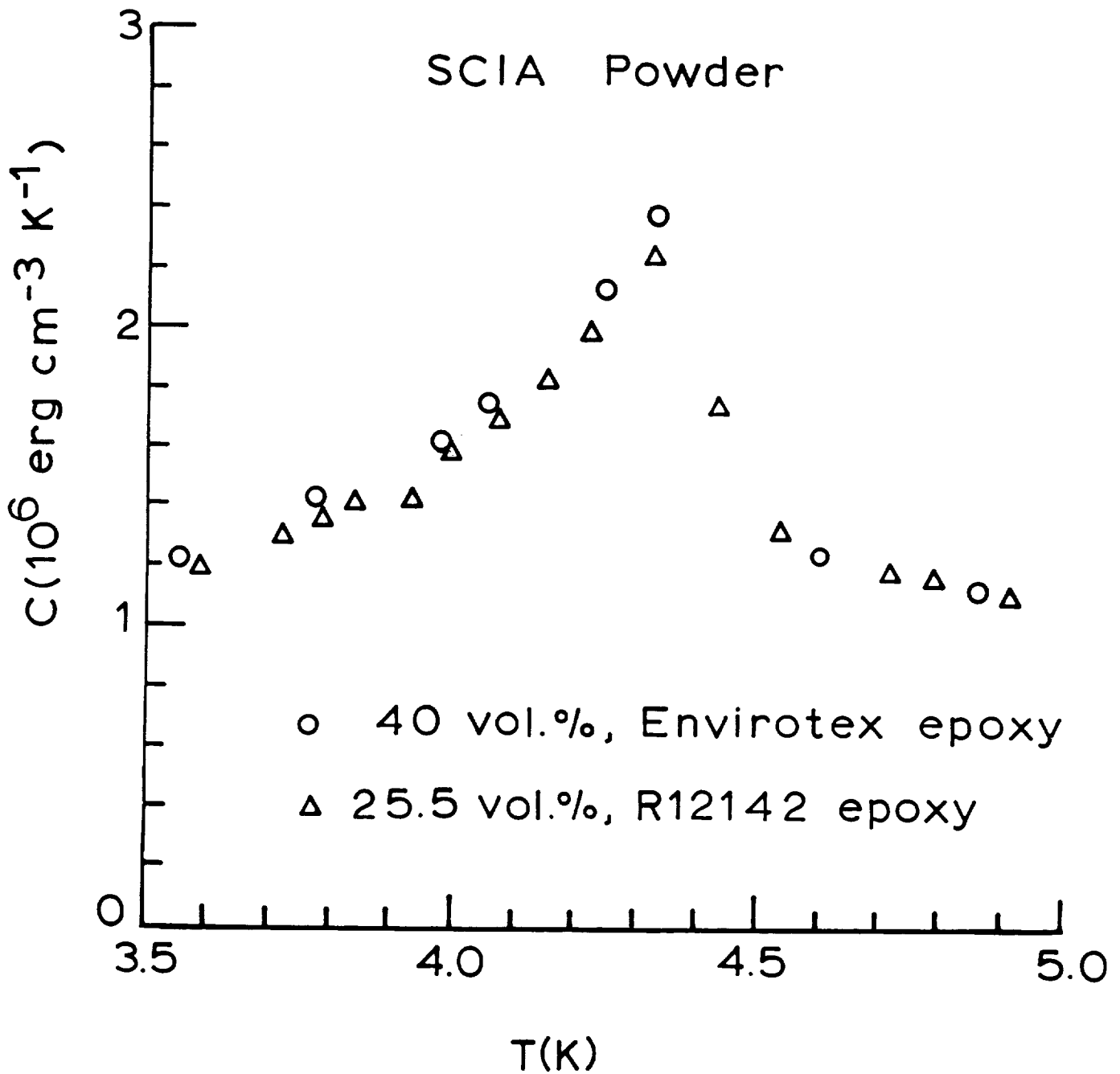Figure A-15. Volumetric specific heat data for the 40 vol.% SCIA composite in Envirotex epoxy.

Figure A-16. Separated specific heat data for the SCIA powders in the composites with the Envirotex and R12142 epoxies.
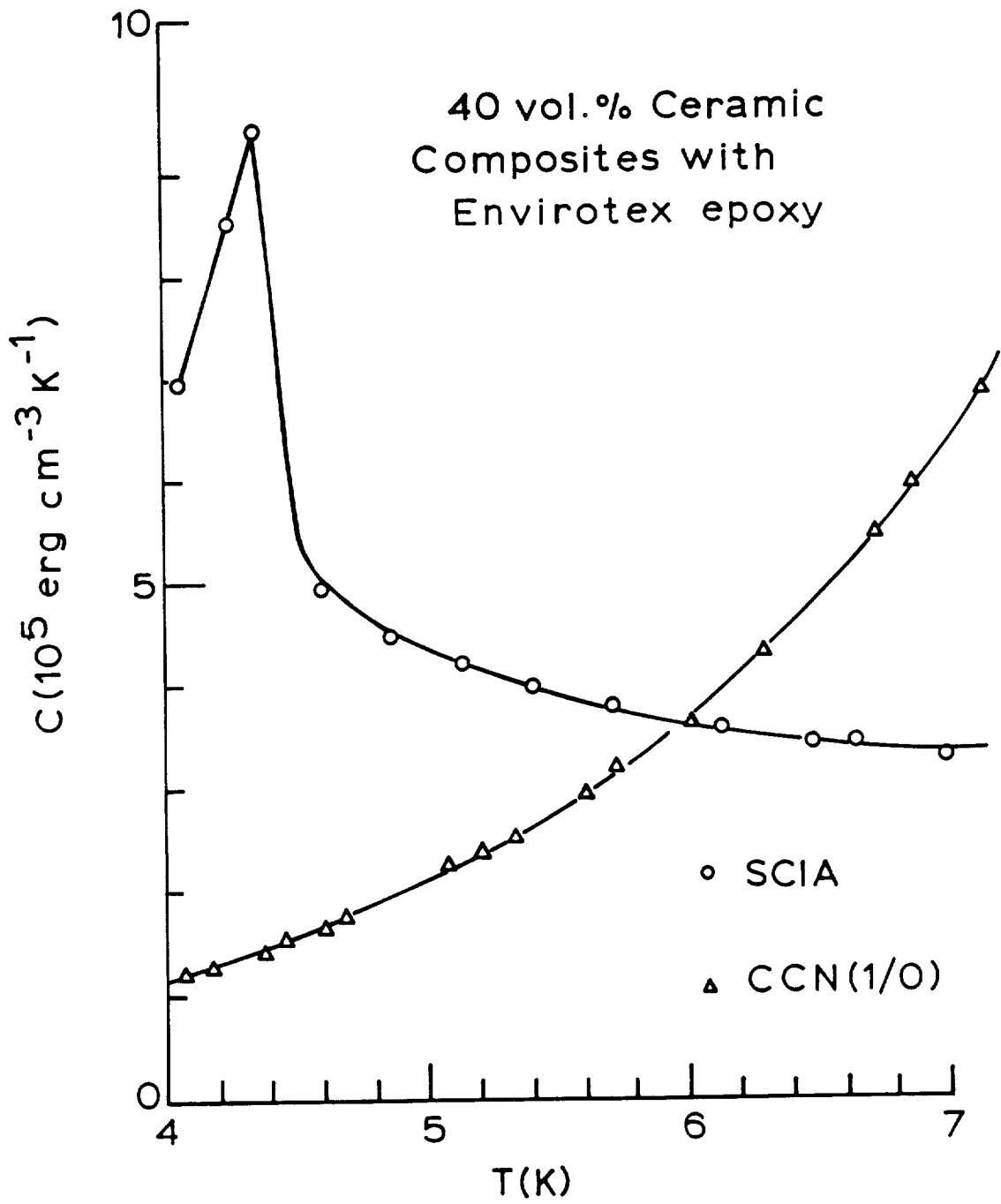
Figure A-17. Comparison of the volumetric specific heats of 40 vol.% composites of CCN(1/0) and SCIA.

to 6 K.

Thermal Conductivity

Thermal conductivity data for the CCN(9/1) and CCN(1/0) composites are shown in Figs. A-18 and A-19, respectively. Also shown for comparison are data measured on the Envirotex epoxy.

The data for the Envirotex epoxy in Figs. A-18 and A-19 show the well-known plateau in the thermal conductivity exhibited by all amorphous materials, and it is interesting to observe that this plateau is also reflected in the data for the lowest filling ratios (30%). This is to be expected since connectivity between the ceramic grains occurs at about 37%.

There is an improvement in the thermal conductivity of the CCN composites in Figs. A-18 and A-19 as the filling ratio increases. However, in all cases the thermal conductivity is depressed compared to that of the pure epoxy.

Thermal conductivity data for the SCIA composites -- 25.5 vol.% in Envirotex and 40 vol.% in R12142 epoxies -- are shown in Fig. A-20, and linear variations of the thermal conductivity with temperature are seen. It is interesting to observe that at 25.5 vol.%, well below the connectivity limit, there is no evidence for the plateau in the thermal conductivity, in contrast to the 30 vol.% data in Figs. A-18 and A-19 for the CCN composites.

Data for the two epoxies are also shown in Fig. A-20, and the R12142 epoxy has the larger thermal conductivity. Nonetheless, the 40 vol.% composite with Envirotex has the larger thermal conductivity of the two composites, and this reflects the intergranular connectivity in this composite.

Finally, in Fig. A-21 are shown a comparison of the thermal conductivity data for the 40 vol.% powder composites with the Envirotex epoxy in the important temperature range above 4.2 K. This comparison is a companion figure to the comparative specific heat data shown in Fig. A-17. The Fig. A-21 data show that the thermal conductivity of the SCIA composite is about $2-2\frac{1}{2}$ times larger than that of the CCN(1/0) composite in the temperature range shown. Up to 5.7 K, however, the epoxy has the largest
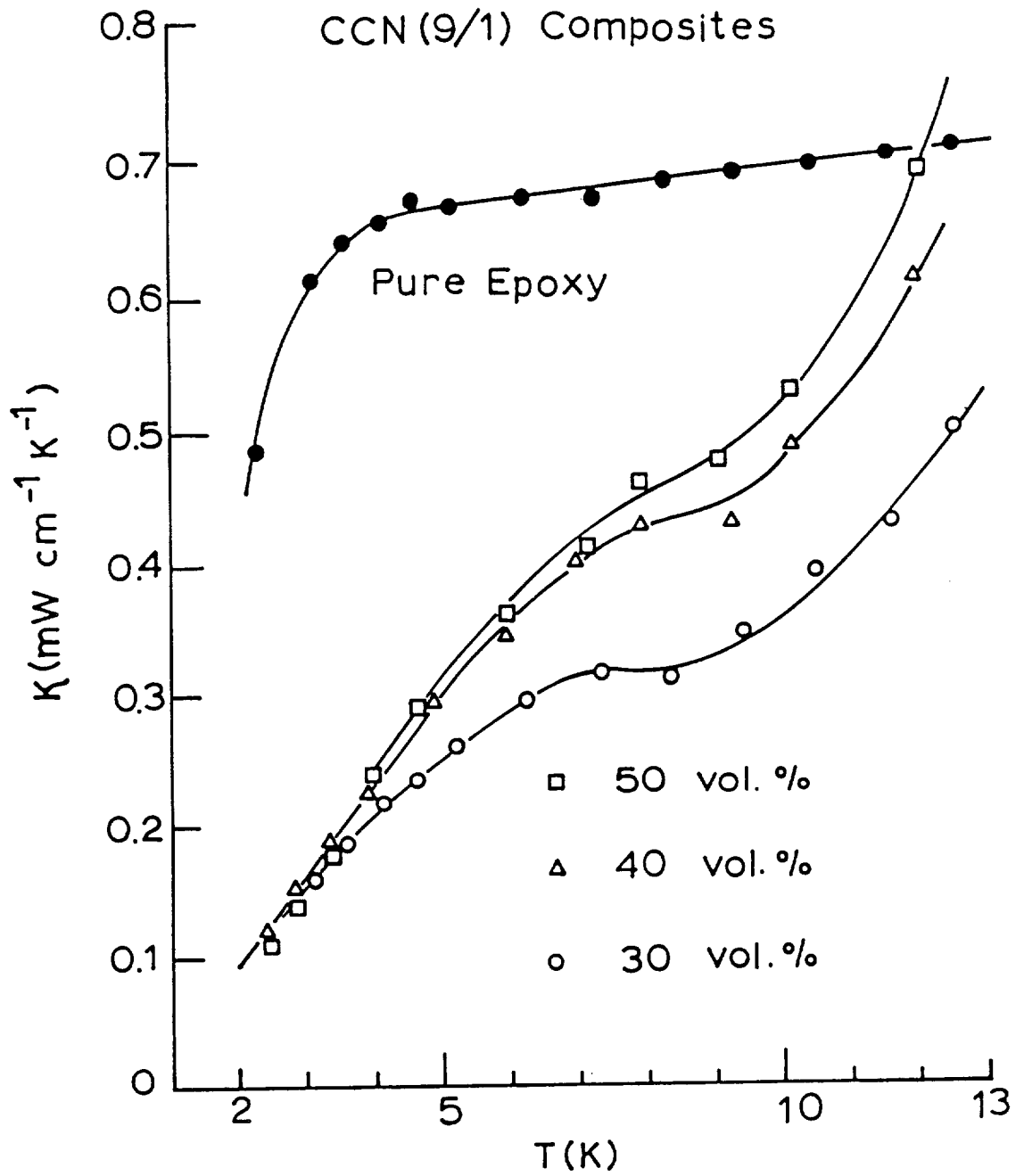
Figure **A-18.** Thermal conductivity data measured on the CCN(9/1) composites. Data for the Envirotex epoxy are shown for comparison.
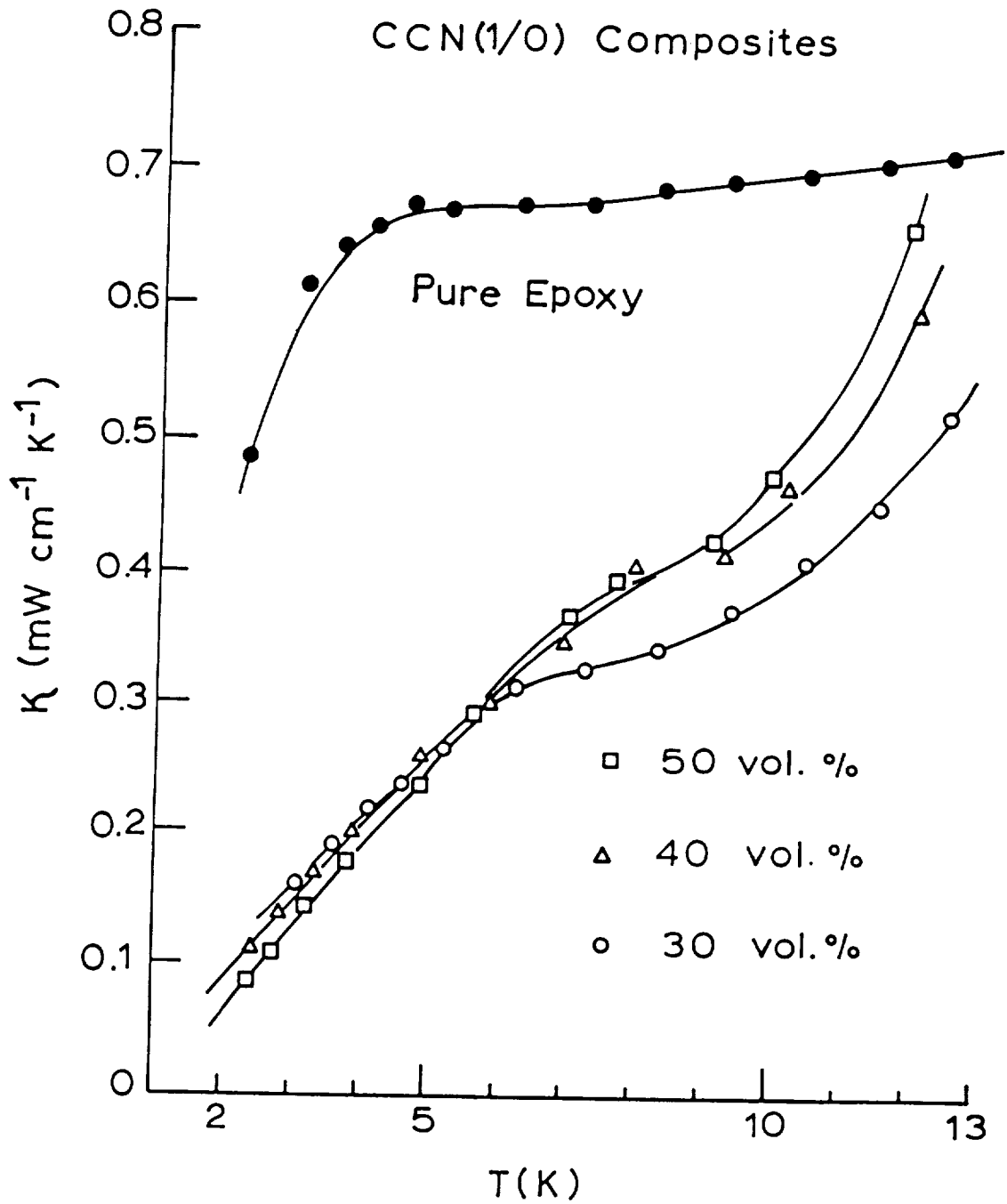
Figure **A-19**. Thermal conductivity data measured on the CCN(1/0) composites and on the Envirotex epoxy.
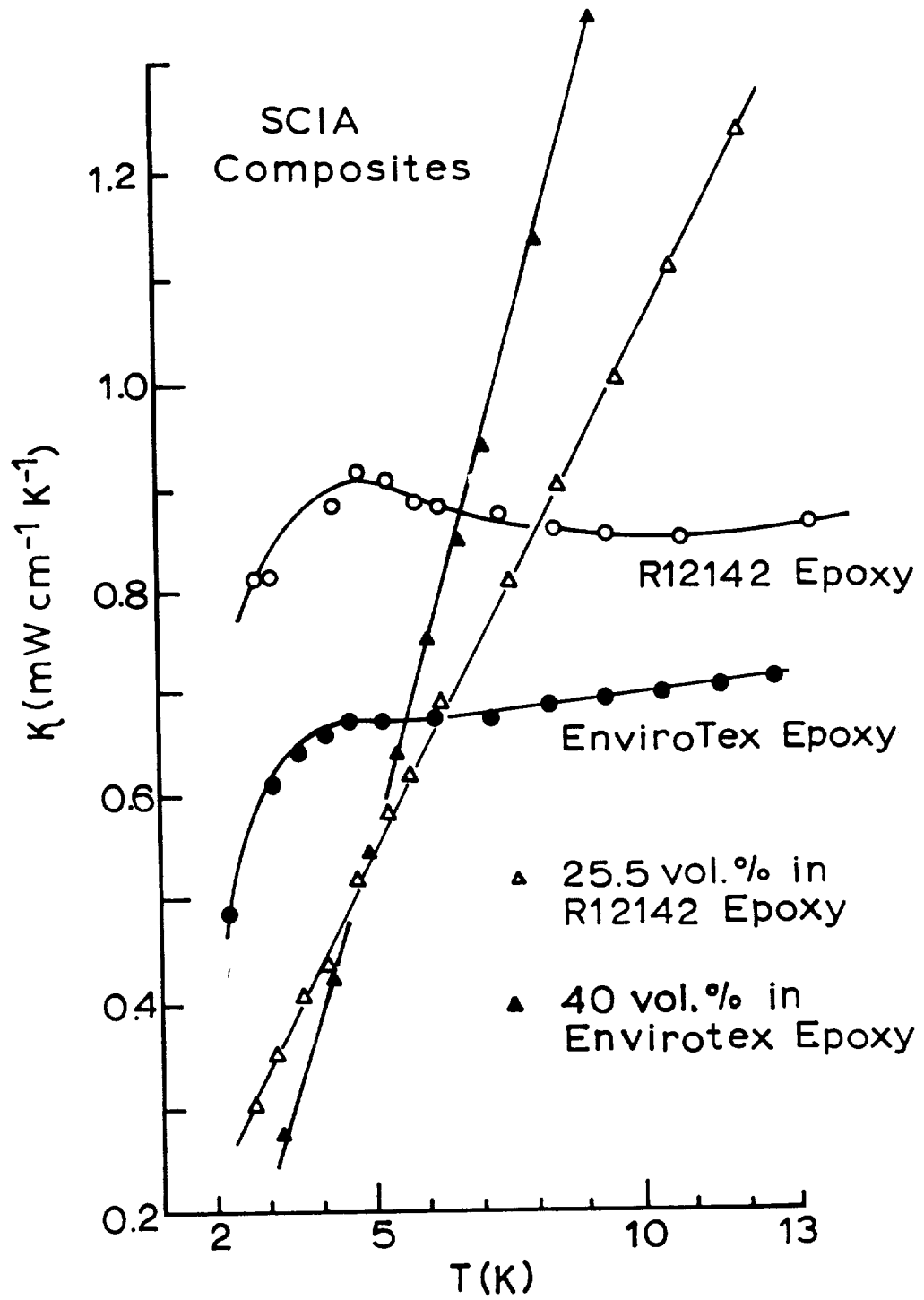
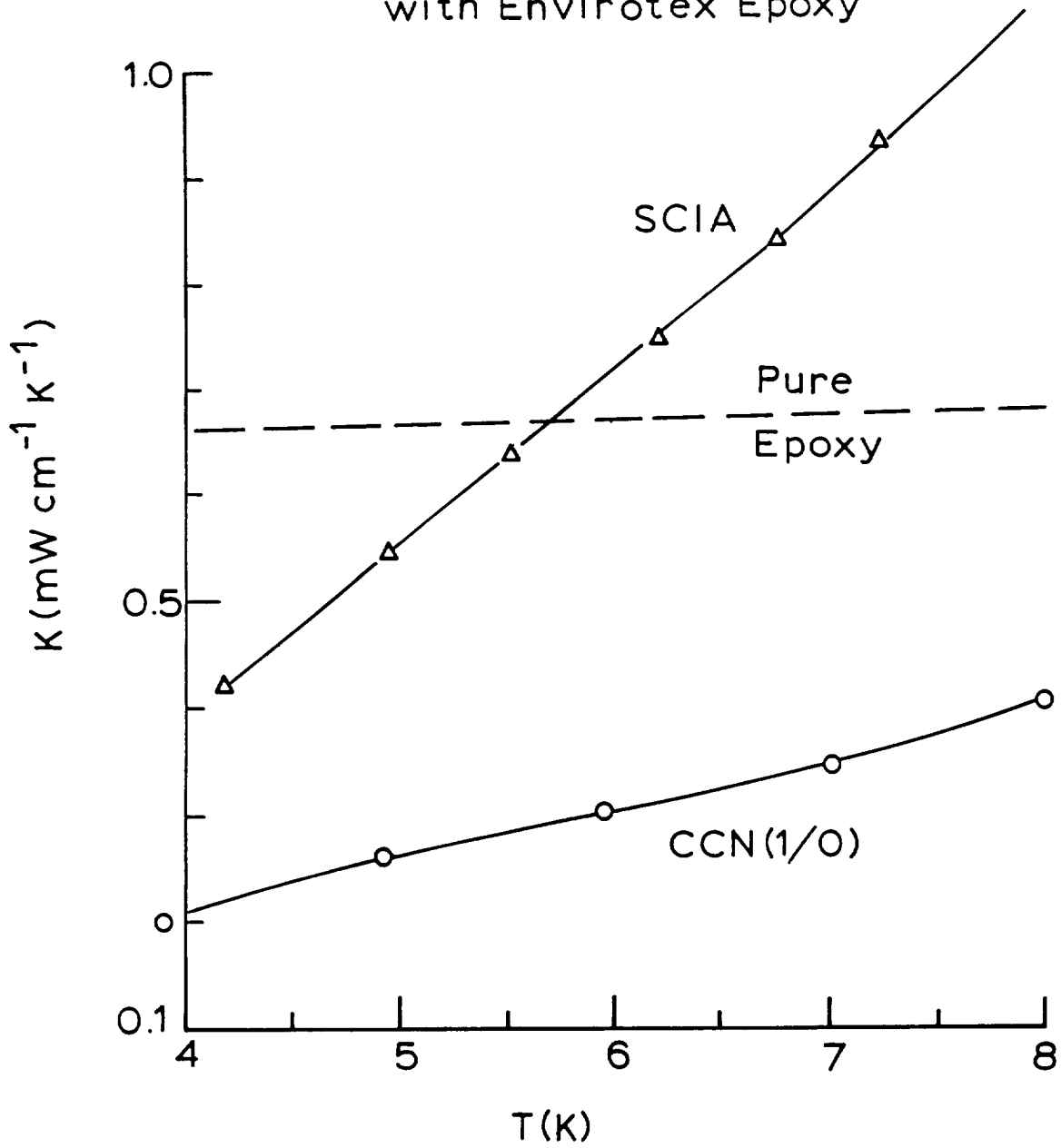Figure A-20. Thermal conductivity data for the SCIA composites with the Envirotex and R12142 epoxies.

Figure A-21. Comparison of the 40 vol.% powder composites with the Envirotex epoxy. Thermal conductivity data for the pure epoxy are also shown.

thermal conductivity.

Review of Zero-Field Thermal Properties

A large amount of data have been documented in this section, and it is worthwhile to review the salient findings from these zero-field measurements.

1. From Figs. **A-7** to **A-9**, the thermal contraction of 40% SCIA is equivalent to that of 50% CCN(1/0); the indications are that a 50% SCIA composite may match copper very closely in thermal contraction.

2. Both the CCN and SCIA ceramic powders enter the epoxy matrices such that the component specific heats are additive, Figs. **A-12** and **A-16**.

3. In a one-to-one comparison at the 40 vol.% powder level in the Envirotex epoxy, the SCIA composite has a larger specific heat up to 6 K than that of the CCN(1/0) composite, Fig. **A-17**. Similarly, this SCIA composite has the larger thermal conductivity, Fig. **A-21**.

C 3

A.1.3 MEASUREMENTS IN INTENSE MAGNETIC FIELDS

The zero-field thermal measurements in the previous section appear to favor the SCIA composites over the CCN composites, at least up to 6 K. However, since these materials are intended for applications involving intense magnetic fields, any judgements here must take into account thermal properties in the presence of such fields. In this section we consider magnetocaloric effects and field-dependent specific heats for these composites in the range 4-10 K.

Four composite samples were selected for these magnetic-field measurements: 40 vol.% CCN(9/1), 40 vol.% CCN(1/0), and 50 vol.% CCN(1/0) in the Envirotex epoxy; and 25.5 vol.% SCIA in the R12142 epoxy (The 40 vol.% SCIA sample was not available at the time of these measurements).

The sample weights and addenda contributions for these four samples are summarized in Table A-5.

We immediately see from Table A-5 that the addenda corrections entering Eq.(A-20) are small. The largest case is only 3% for the SCIA sample, and this occurs at about 10 K; at 4 K this factor is only 0.3% for this sample.

Table A-5
Sample Weights and Addenda Contributions

Sample	Sample Wt.(g)	Addenda Wt.%	Addenda Heat Capacity[c]
40% CCN(1/0)[a]	1.1966	3.92	<1.01%
40% CCN(9/1)[a]	1.0383	4.73	<1.46%
50% CCN(1/0)[a]	1.3967	3.30	<0.71%
25.5% SCIA[b]	1.1830	4.84	<3.35%

[a] Vol.% in Envirotex epoxy

[b] Vol.% in R12142 epoxy

[c] Expressed as a percentage of the total heat capacity in the range 4-10 K [i.e., C_a/C_s in Eq.(A-20)].

We remark that the reason these addenda corrections are small derives from the "suspended sample" technique shown in Fig.

A-5; it is tedious and time-consuming to employ this technique with the associated requirement for _in_ _situ_ thermometer calibration, but the technique yields accurate results.

The carbon-chip thermometers embedded in the samples were calibrated _in-situ_ during each run against a calibrated Ge thermometer in the range 4-10 K according to Eq.(A-8). Six to seven calibration points were taken, and the average fitting errors deserve mentioning: 40% CCN(1/0), 18 mK; 40% CCN(9/1), 7 mK; 50% CCN(1/0), 14 mK; and 25.5% SCIA, 8 mK. These fitting errors are commensurate with the calibration uncertainty of the Ge thermometer in this range, ~ ± 10 mK. Note also in this regard that magnetocaloric measurements involve temperature differences.

Magnetocaloric Measurements

The zero-field time constants, τ_o, were measured as follows: At stabilized set points (i.e., calibration points) the samples were pulsed with the heaters ($\Delta T/T \lesssim 3\%$), and the resulting time-voltage chart trace records were converted to time-temperature records using the Eq.(A-8) calibrations. Analyses of these records according to Eq.(A-11) then yields τ_o. These τ_o-data are summarized in Table A-6.

<div align="center">

Table A-6

Zero-Field Thermal Time Constants

</div>

T_{avg}	τ_o(s)			
	40% CCN(1/0)	40% CCN(9/1)	50% CCN(1/0)	25.5% SCIA
3.97 K	175±5	–	–	–
4.14	–	–	95±2	–
4.25	230±7	174±2	–	207±7
5.06	237±6	241±3	–	742±28
6.11	407±12	351±6	213±7	624±19
7.12	707±52	525±13	–	564.13
7.99	–	–	567±14	–
8.31	783±12	1091±30	–	546±7
10.3	578±4	740±16	–	564±13

We now consider how these time constants enter the correction factor in Eq.(A-20), $(1+\Delta t/2\tau_H)$, where τ_H is given by Eqs.(A-17) and (A-18). We take the following approach: The longest ramp time, Δt, is 30 s to 10 T, and we consider the minimum τ_o to satisfy the condition $\Delta t/2\tau_H < 5\%$. In this worst case, we find that $\tau_o > 158$ s, which is satisfied in all cases in Table A-6 except for the 50% CCN(1/0) sample at 4.14 K. For the remaining three samples in Table A-6, the largest $\Delta t/2\tau_H$-values are: 4.5% for CCN(1/0), 4.5% for CCN(9/1), and 3.81% for SCIA, all at 10 T. At smaller field levels, the $\Delta t/2\tau_H$-values are greatly diminished; e.g., at 5 T, $\Delta t/2\tau_H$ is 65% of the value at 10 T, irrespective of τ_o.

The problem now is to judge from Tables A-5 and A-6 which correction factors may be significant at 10 T, consistent with the $\lesssim \pm 5\%$ uncertainty in measuring the magnetocaloric ΔT's. Since both the addenda and thermal-time-constant corrections are clearly small, we can re-write Eq.(A-20) as,

$$\Delta T_{act} = \Delta T_{meas}(1+C_a/C_s + \Delta t/2\tau_H), \qquad (A-22)$$

and ask under what conditions the combined factor exceeds 5%. Considering the 40% CCN(1/0) sample first, we find the combined factor is < 3.43% in the worst case, and so can be ignored. For the 40% CCN(9/1) sample, we find 6.0% at the lowest temperature (4.25 K), so here the combined factor is important. For the 50% CCN(1/0) sample, we find 9.0% at the lowest temperature, which must be taken into account. And finally for the 25.5% SCIA sample, we find 7.2% at the lowest temperature.

We remark that the advantage of the fast-ramping Bitter magnets at the Nat'l Magnet Lab. is clearly seen in these examples. For illustration, if ramp rates to 10 T ~ 15 min were involved, as is common with superconducting magnets, then the 5% criterion above would correspond to $\tau_o > 3.1 \times 10^3$ s, which in turn would mean prohibitively long cooldown times.

As mentioned above, the capacitance thermometer was used to control the reservoir temperature in intense magnetic fields.

Although the reservoir temperature was precisely controlled and although in the cycle $0 \to H \to 0$ the sample temperature returned very nearly to the reservoir temperature, there is still the problem of defining the average temperature of the magnetocaloric events. Our procedure was to compute the average temperature for each $0 \to H \to 0$ event and then to take the average of all these average temperatures for the complete data set. If the magnetocaloric ΔT's were small, the deviations in these average temperatures were small -- e.g., $\sim \pm 10$ mK for the CCN samples. If, however, the magnetocaloric ΔT's were large, as in the case of the SCIA sample (see below), the corresponding deviations were large, $\sim \pm 100$ mK.

In all the measurements reported here, the <u>hysteretic</u> components computed from Eqs.(A-21) were found to be negligibly small, $\sim 1-5$ mK, and so will be ignored.

The measured, reversible ΔT_r data for the composites are shown in Figs. A-22 through A-25, corrected according to Eq.(A-22) where appropriate. All data are plotted as ΔT_r vs. H^2 for comparison with a perfect paramagnet where $\Delta T_r \propto H^2$. The convention used in these plots is that $\Delta T_r > 0$ corresponds to adiabatic <u>demagnetization</u> cooling, whereas $\Delta T_r < 0$ corresponds to adiabatic <u>magnetization</u> cooling, and this convention is indicated in the figures. Stated differently, an <u>additional</u> enthalpy stabilization mechanism occurs on <u>up-ramp</u> if magnetization cooling occurs.

Figure A-22 shows ΔT_r-data for the 40 vol% CCN(1/0) composite, and in the neighborhood of 4.2 K magnetization <u>heating</u> occurs, although the effect is small, ~ 20 mK. Interestingly, at higher temperatures magnetization <u>cooling</u> occurs above about 3 T, so in some respects the magnetocaloric effects here are self-limiting.

Figure A-23 shows ΔT_r-data for the two CCN(1/0) composites [the 50% vol.% CCN(1/0) sample was selected primarily as a duplicate sample]. The agreement between the data sets at (approx.) 4.3, 6, and 8 K is very good and lends confidence to the experimental and analytical techniques. The 50% sample has
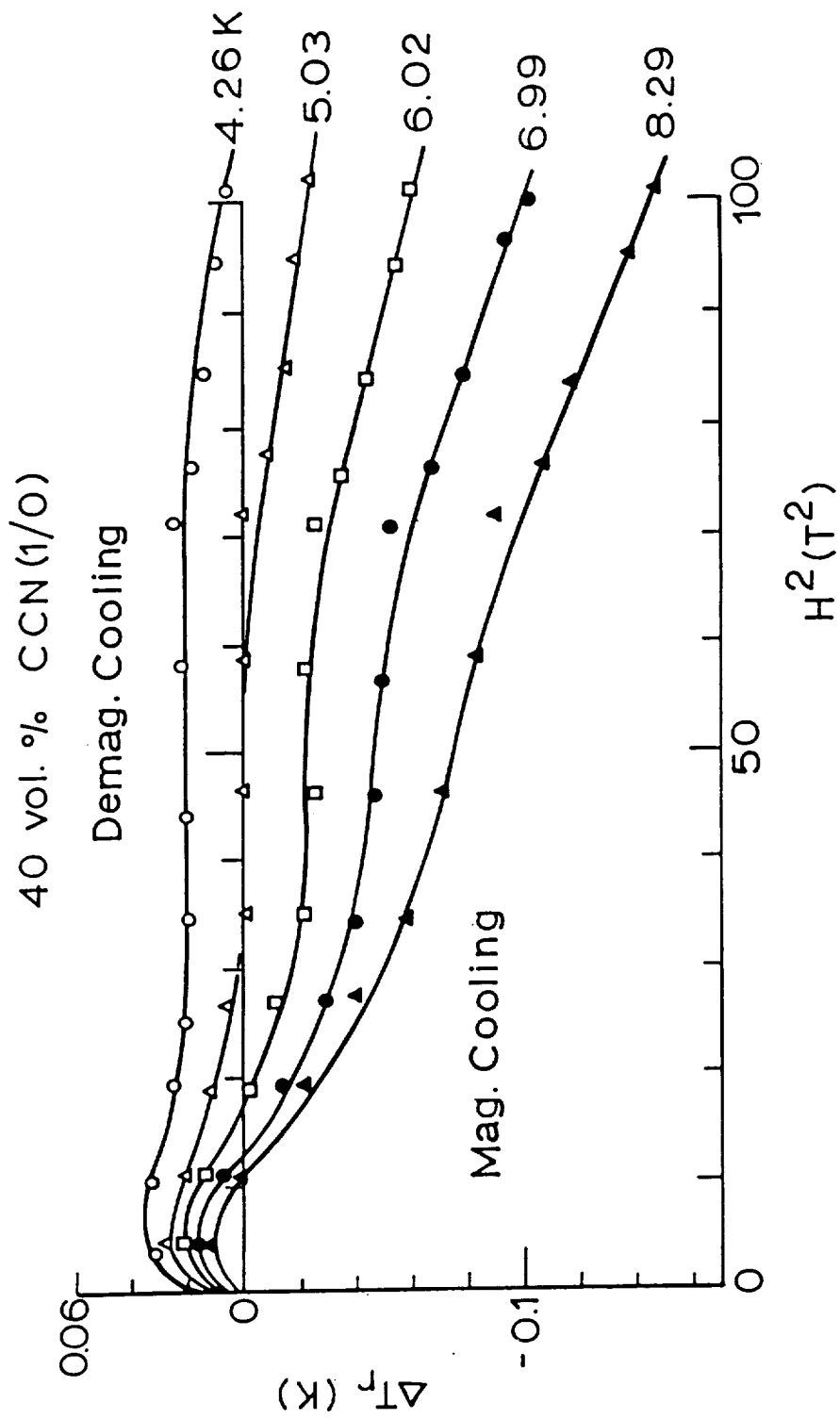
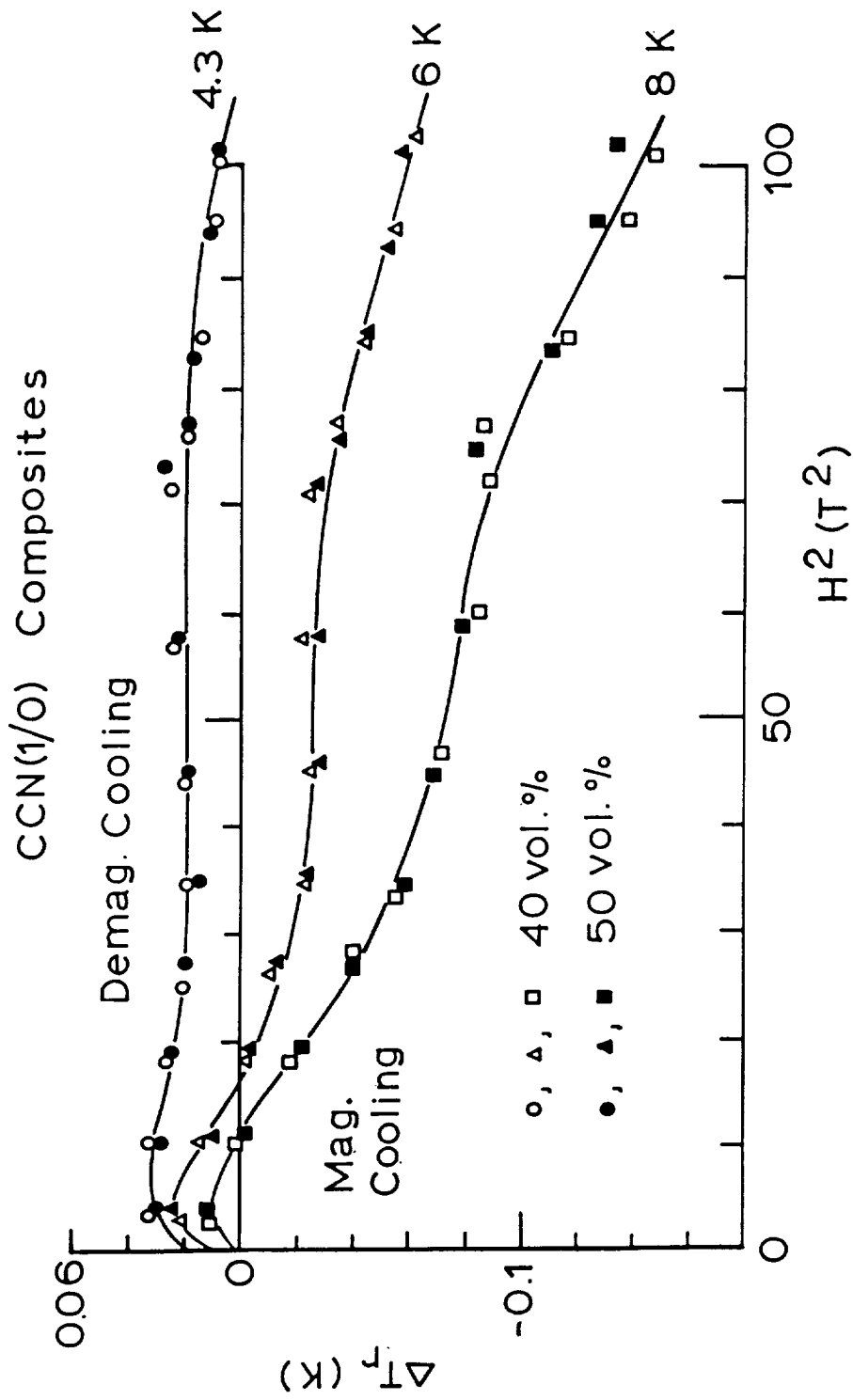Figure **A-22.** Magnetocaloric data measured on the 40 vol.% CCN(1/0) composites.

Figure A-23. Magnetocaloric data measured on the CCN(1/0) composites.
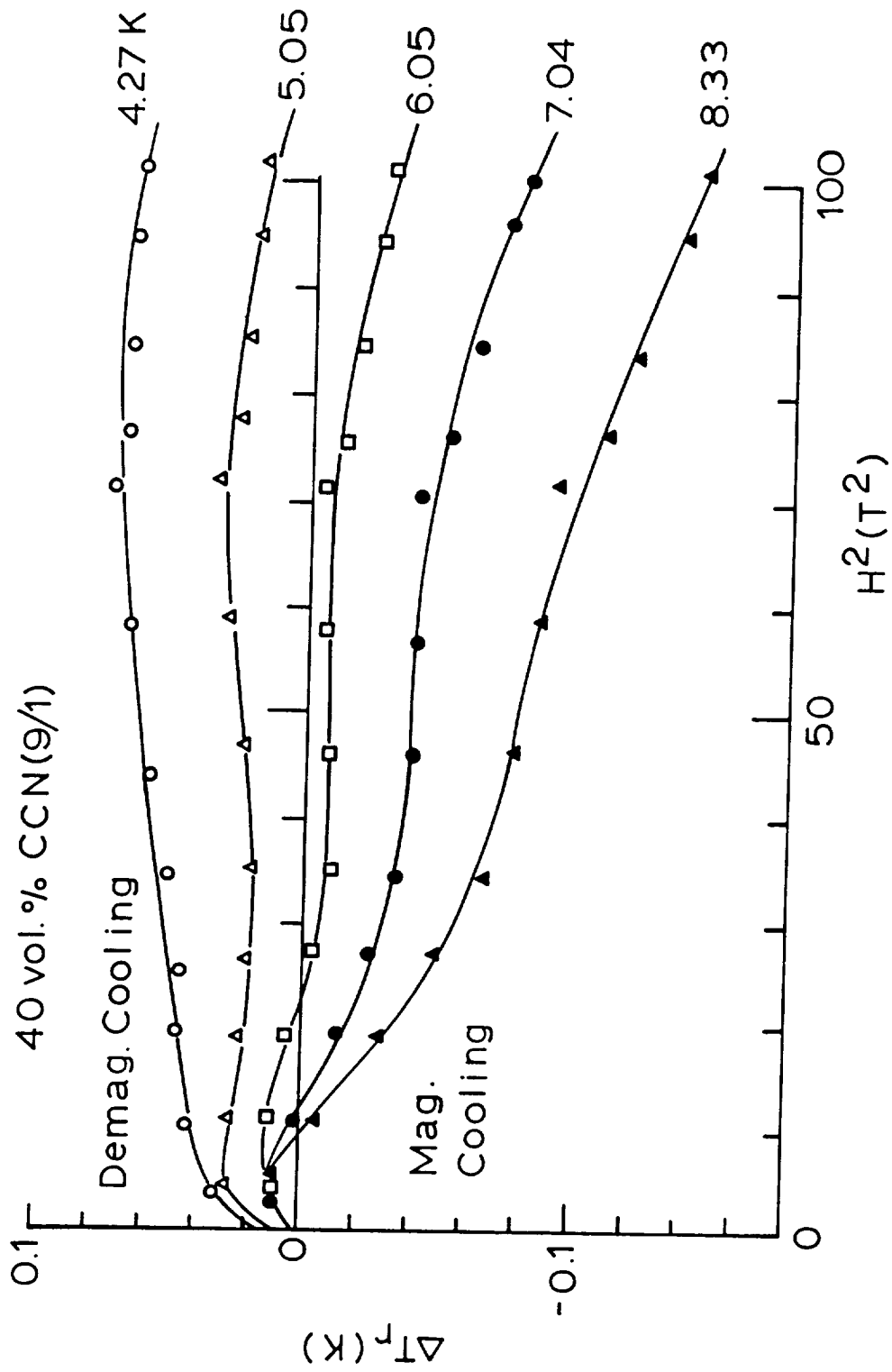
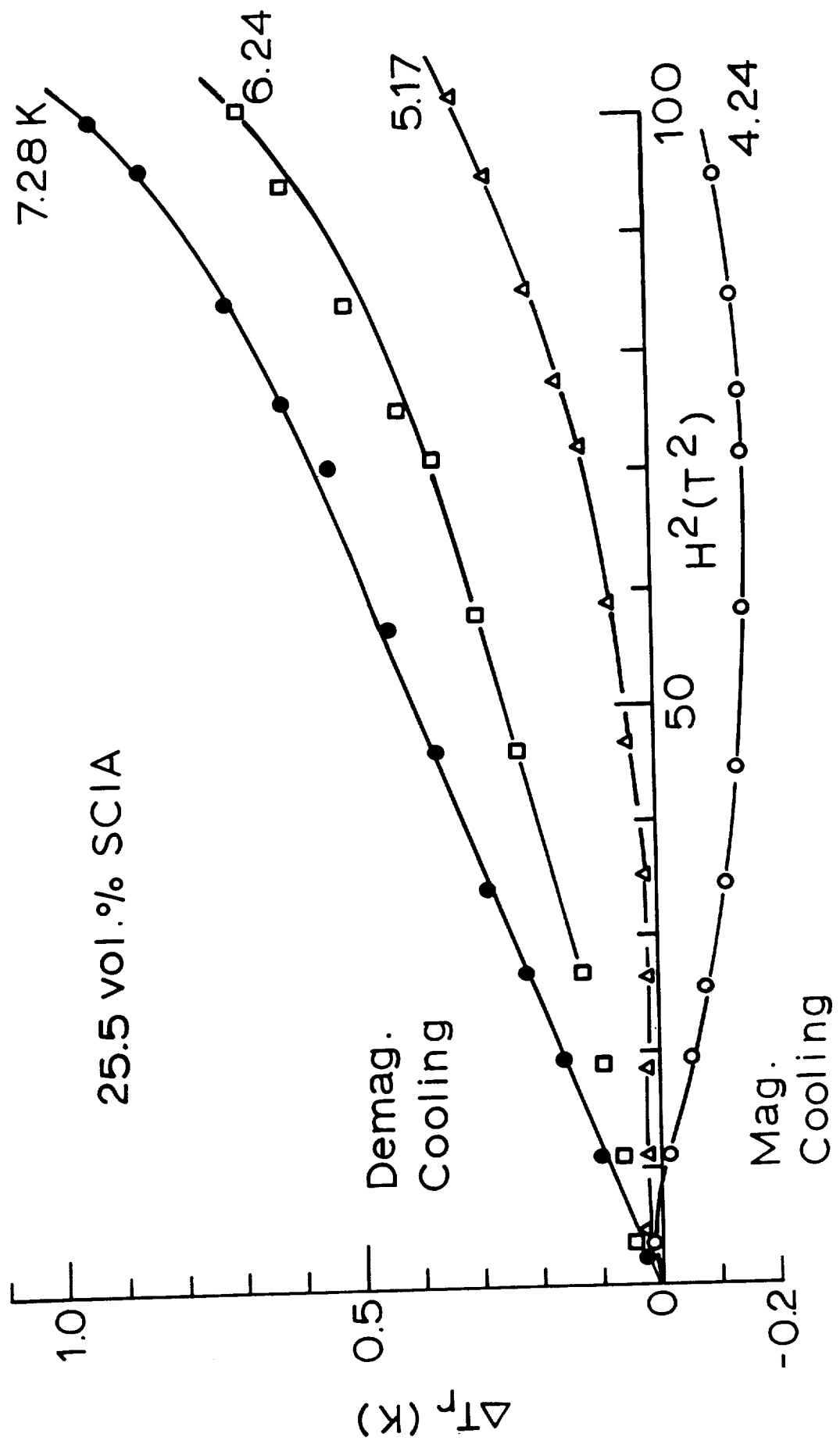Figure A-24. Magnetocaloric data measured on the 40 vo.% CCN(9/1) composite.

Figure A-25.   Magnetocaloric data measured on the 25.5 vol.% SCIA composite.

the larger specific heat and is expected to have slightly smaller ΔT_r's -- this trend is somewhat apparent in Fig. A-23, but the scatter in the data and the different average temperatures (e.g., 8.29 vs. 8.04 K) obscure meaningful comparisons here.

Figure A-24 shows ΔT_r-data for the CCN(9/1) composite, and here a substantial difference is seen on comparison with the corresponding 40 vol.% CCN(1/0) composite in Fig. A-22. Although the overall trends are similar, the CCN(9/1) composite retains a significantly larger magnetization heating ΔT_r in the 4.3-5 K temperature range.

Finally, ΔT_r-data for the SCIA composite are shown in Fig. A-25, and here the reverse trend is seen compared to Figs. A-22 to A-24. Namely, this composite exhibits a magnetization <u>cooling</u> characteristic at 4.2 K which reverts to a magnetization heating characteristic at higher temperatures. By 7.3 K, large effects are seen, $\Delta T_r \sim 1$ K.

Reversible magnetocaloric data for the four composites show interesting phenomena. In all cases, a reversion of the sign of the magnetoclaoric effect is seen, and this has a straightforward explanation: Antiferromagnetic phase transitions are involved which involve extensive spin-frustration; thus, near these transitions there is competition between the magnetization-cooling of antiferromagnetic spins and the demagnetization-cooling of free spins. This is seen most clearly in Fig. A-25 where at the highest temperature the free-spin $\Delta T_r \propto H^2$ behavior is seen up to $\sim$ 8 T.

Field-Dependent Specific Heat Measurements

The magnetocaloric effects measured above represent a potential stabilizing mechanism on up-ramp (magnetization cooling) or down-ramp (demagnetization cooling). To judge the importance of the energetics involved here, data are needed on the magnetic-field dependence of the specific heat which we consider in this section.

The measurements here were performed by the "drift" method cited earlier,[6] with one exception: Instead of capacitance

thermometers on the samples, carbon-chip thermometers were employed. The reason for this change is that erratic electrical noise problems at the NML can frustrate the use of capacitance thermometry for the samples (the capacitance thermometer on the reservoir is not affected). These carbon-chip thermometers require a magnetoresistance correction, given by Eq.(A-9). The samples here were maintained at helium temperatures between the magnetocaloric and specific-heat experiments, so the calibrations of the thermometers according to Eq.(A-8) were used in both measurements.

Once the drift conditions were established, the data were recorded every 15 s on a Minc 11 DEC system, and the amplifier function of the Keithley Model 181 nanovoltmeters was employed as input to the Minc. The reservoir was temperature-controlled at about 1.9 K in all the drifts using the capacitance thermometer in the reservoir. The 10-4 K drift times ranged from about 30 min in zero field to 1 hr at 10 T. All data reductions were done at CeramPhysics using software developed over several years. The results of these measurements are shown in Figs. A-26 through A-30.

The specific heat data in Fig. A-26 are for the 40% CCN(1/0) composite at 0,2,4,6,8, and 10 T. As seen, the specific heat has essentially no magnetic field dependence although some structure appears near the specific heat maximum at about 8.5 K. The results in Fig. A-26 are very important for this program because they indicate that the enthalpy stabilization associated with this composite is independent of intense magnetic fields.

A somewhat different picture is seen in the specific heat data in Fig. A-27 for the 40% CCN(9/1) composite where some suppression of the zero-field specific heat by intense magnetic fields is suggested. However, the effect is not large and may be due in part to the scatter in the data.

A comparison of the 40% CCN composites is shown in Fig. A-28 where the mean data from Figs. A-26 and A-27 are collected. The CCN(1/0) composite clearly has the larger specific heat at all temperatures.
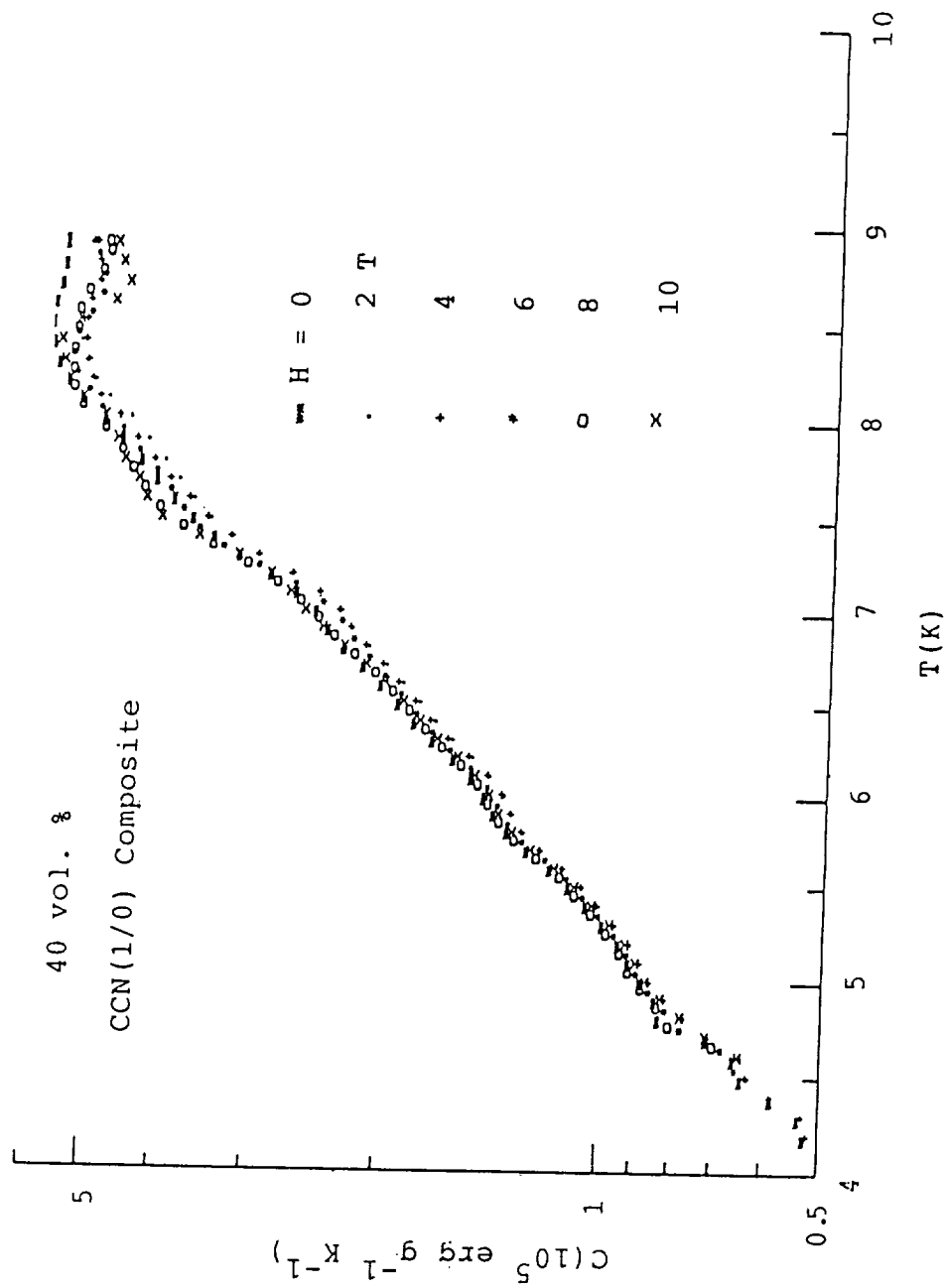
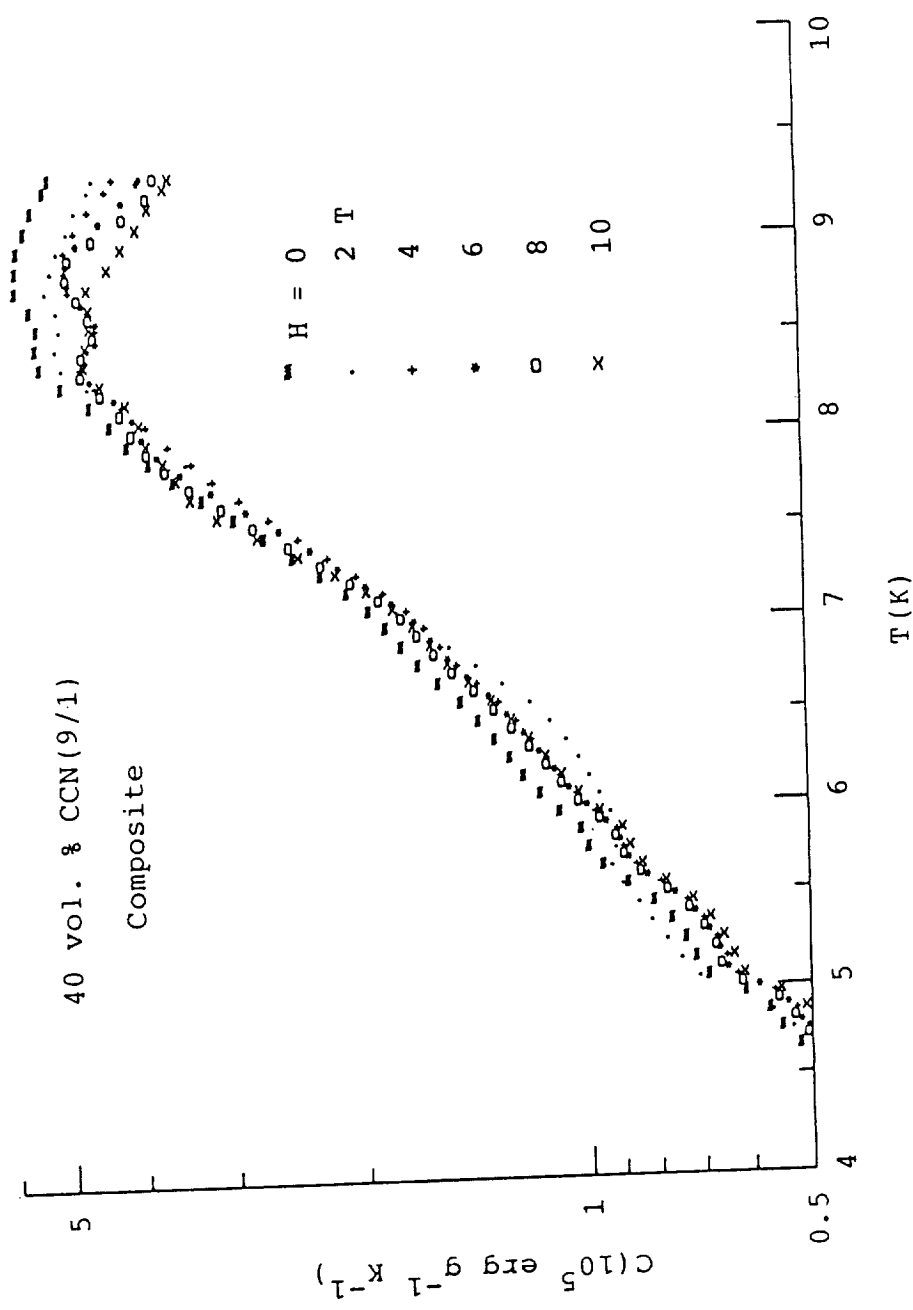Figure A-26. Magnetic-field dependence of the specific heat of the 40 vol.% CCN(1/0) composite.

Figure A-27. Magnetic-field dependence of the specific heat of the 40 vol.% CCN(9/1) composite.
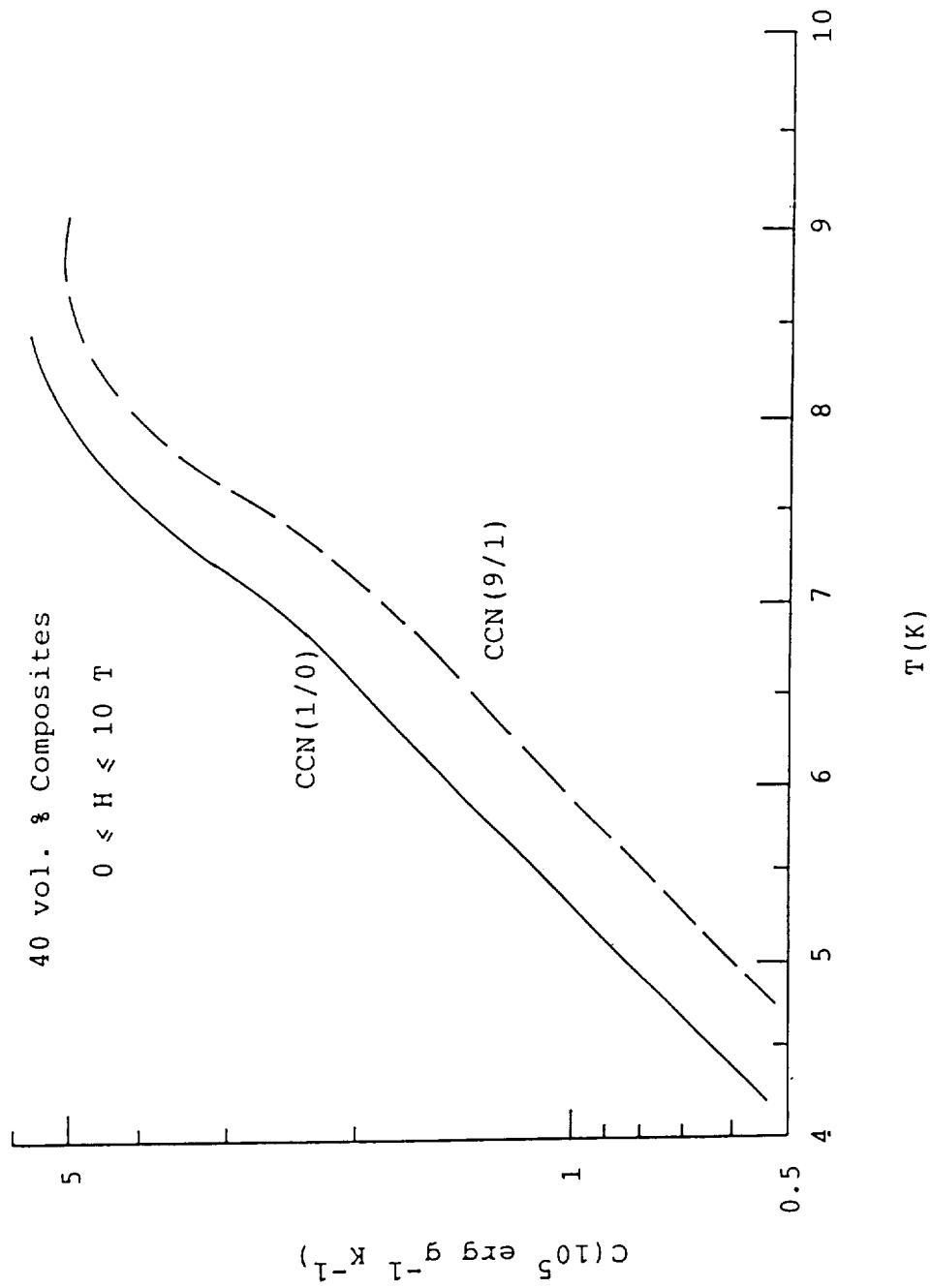
Figure A-28. Comparison of the magnetic-field dependences of the specific heats of the 40 vol.% composites of CCN(9/1) and CCN(1/0).
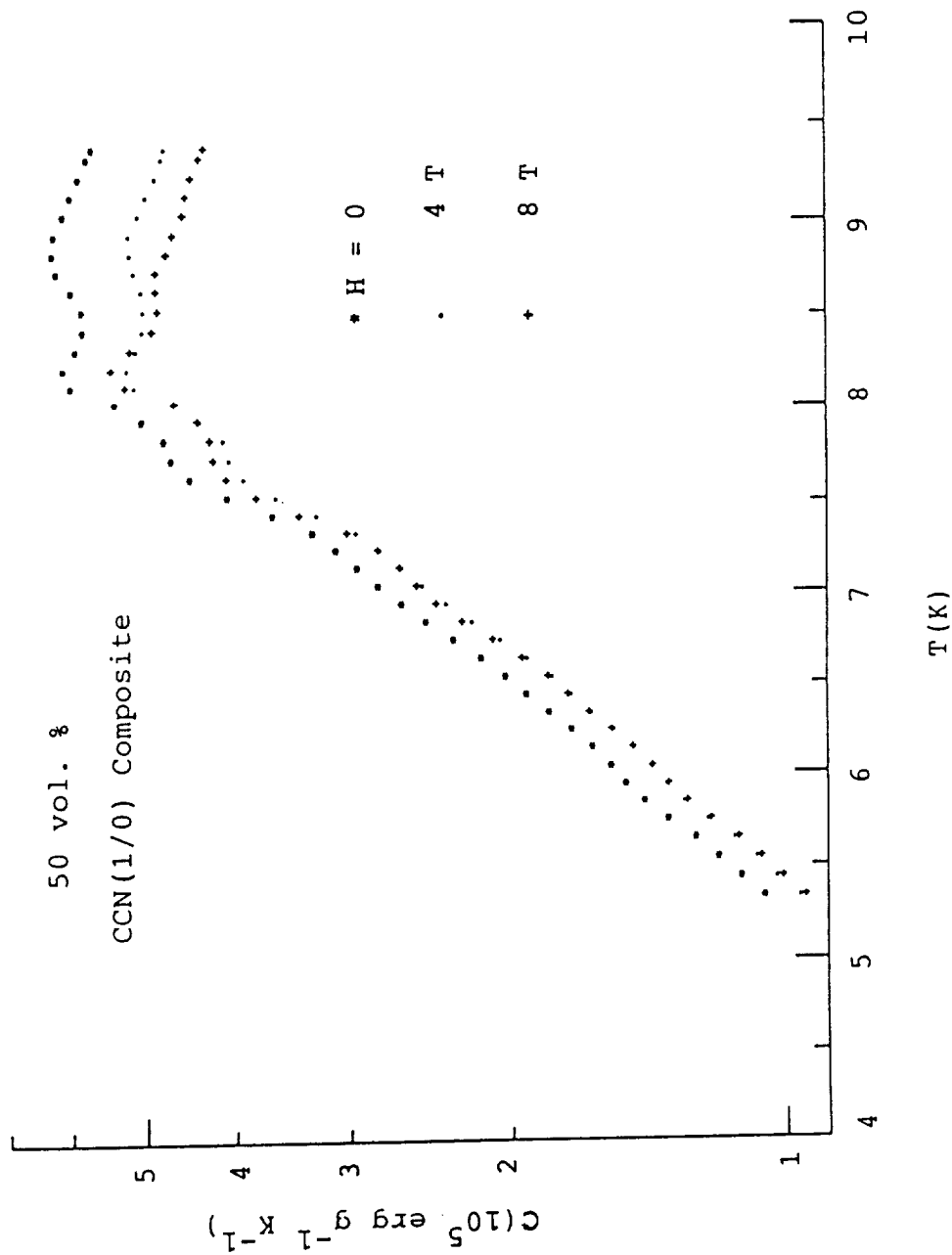
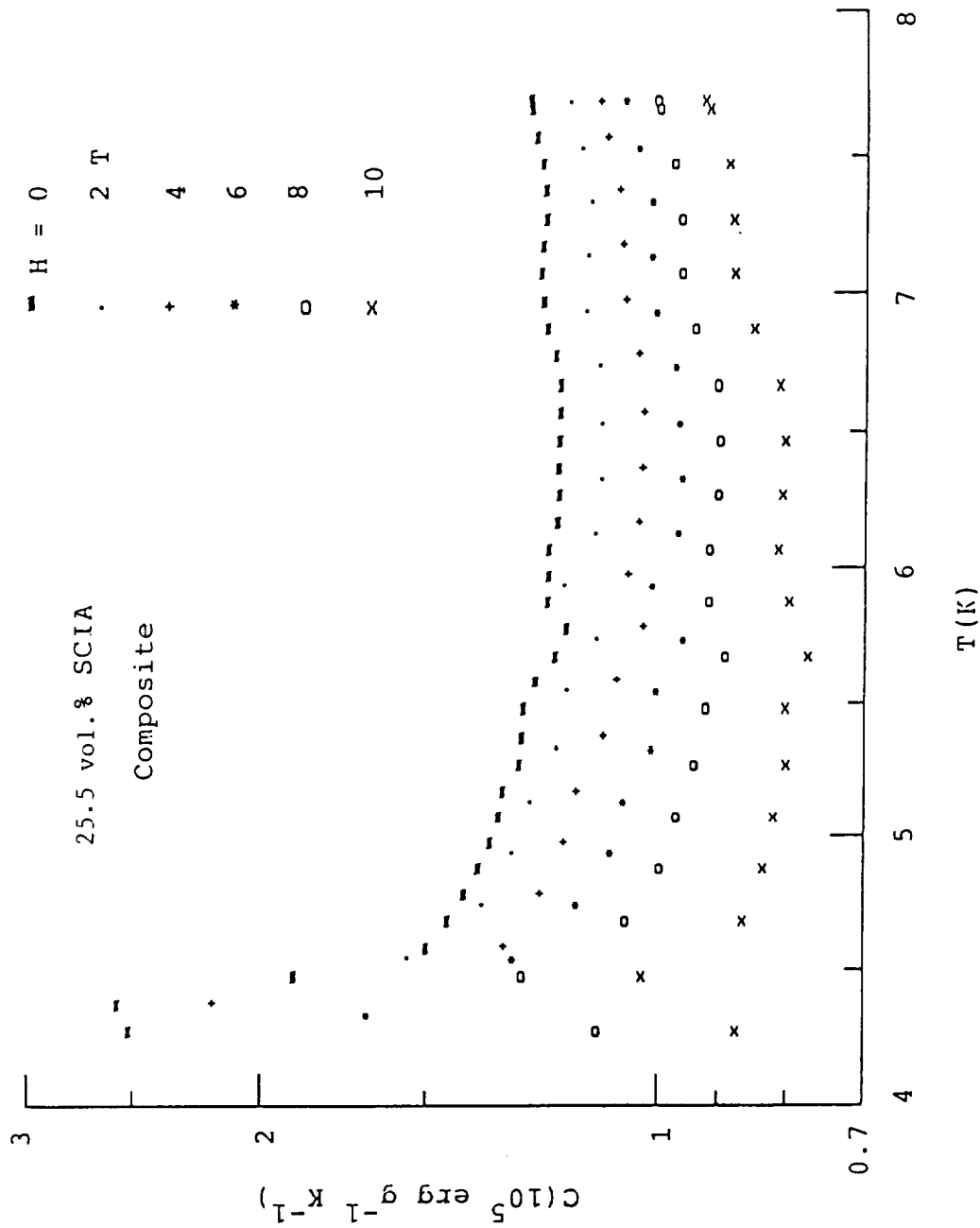Figure **A-29**. Magnetic-field dependence of the specific heat of the 50 vol.% CCN(1/0) composite.

Figure **A**−30. Magnetic-field dependence of the specific heat of the 25.5 vol.%
SCIA composite.

The specific heat data for the 50% CCN(1/0) composite are shown in Fig. A-29 at 0,4, and 8 T, and a field-suppression is evident here, in contrast to the 40% CCN(1/0) composite in Fig. A-26. Although the suppression effect in Fig. A-29 is not large, it is still surprising. The explanation here may lie in the different stress conditions in the two composites due to thermal contraction.

Finally, in Fig. A-30 are shown specific heat data for the 25.5% SCIA composite at 0,2,4,6,8, and 10 T. Here, the field-suppression of the specific heat is unmistakable, in contrast to all the CCN composites. However, the effect here is not large -- at 5 K the H-field suppression at 10 T is ~ 50% of the zero-field specific heat.

Review of Magnetothermal Measurements

It is worthwhile to summarize the principle findings from these magnetothermal measurements:

1. All composites show a reversal of the sign of the magnetocaloric effects with increasing temperature, Figs. A-22 to A-25.

2. At 4.2 K the CCN composites display demagnetization cooling whereas the SCIA composite displays magnetization cooling.

3. The specific heats of the CCN composites are only slightly H-field dependent, Figs. A-26 to A-29.

4. The specific heat of the SCIA composite is suppressed by an H-field, Fig. A-30.

A.1.4 DATA ANALYSES

A very large amount of experimental data on composites have been reported in the above sections, in both zero field and in intense magnetic fields. The studies here have been evolutionary in nature such that at this point we can focus our attention on just the CCN(1/0) and SCIA composites for the purposes of data analyses.

Our analyses here will address three separate areas: (1) Enthalpy relative to 4.2 K taking magnetic field effects into account; (2) The energetics of magnetocaloric effects; and (3) The thermal group parameter, $\eta = \sqrt{\kappa C}$, discussed in Section A.1.0 above.

Enthalpy Relative to 4.2 K

We wish to compare the enthalpies of 40 vol.% powder composites of CCN(1/0) and SCIA with the Envirotex epoxy, and the necessary specific heat data for the CCN(1/0) composite are given above (Figs. A-11 and A-26). However, for the SCIA composite we have zero-field specific heat data on the two composites with different epoxies (Figs. A-14 and A-15), but the H-field dependent specific heat data have been measured only on the SCIA composite with the R12142 epoxy (Fig. A-30). Nonetheless, since we have shown that specific heats are <u>additive</u> for the SCIA powder additions (Fig. A-16), it is straightforward to adjust the H-field data in Fig. A-30 from the 25.5 vol.% in R12142 to the 40 vol.% in Envirotex, and the H = 0 data for the latter case in Fig. A-15 serve as a check on this procedure.

The measured specific heat data for the 40% CCN(1/0) composite and the estimated specific heat data for the 40% SCIA composite were numerically integrated, 4.2-6 K, to obtain the enthalpy (volumetric basis), and these data are shown in Fig. A-31. The enthalpy, $\Delta H_{4.2}$, is field independent for the CCN(1/0) composite, and the field dependence of $\Delta H_{4.2}$ for the SCIA composite is seen in Fig. A-31, based on the measured data in Fig. A-30.

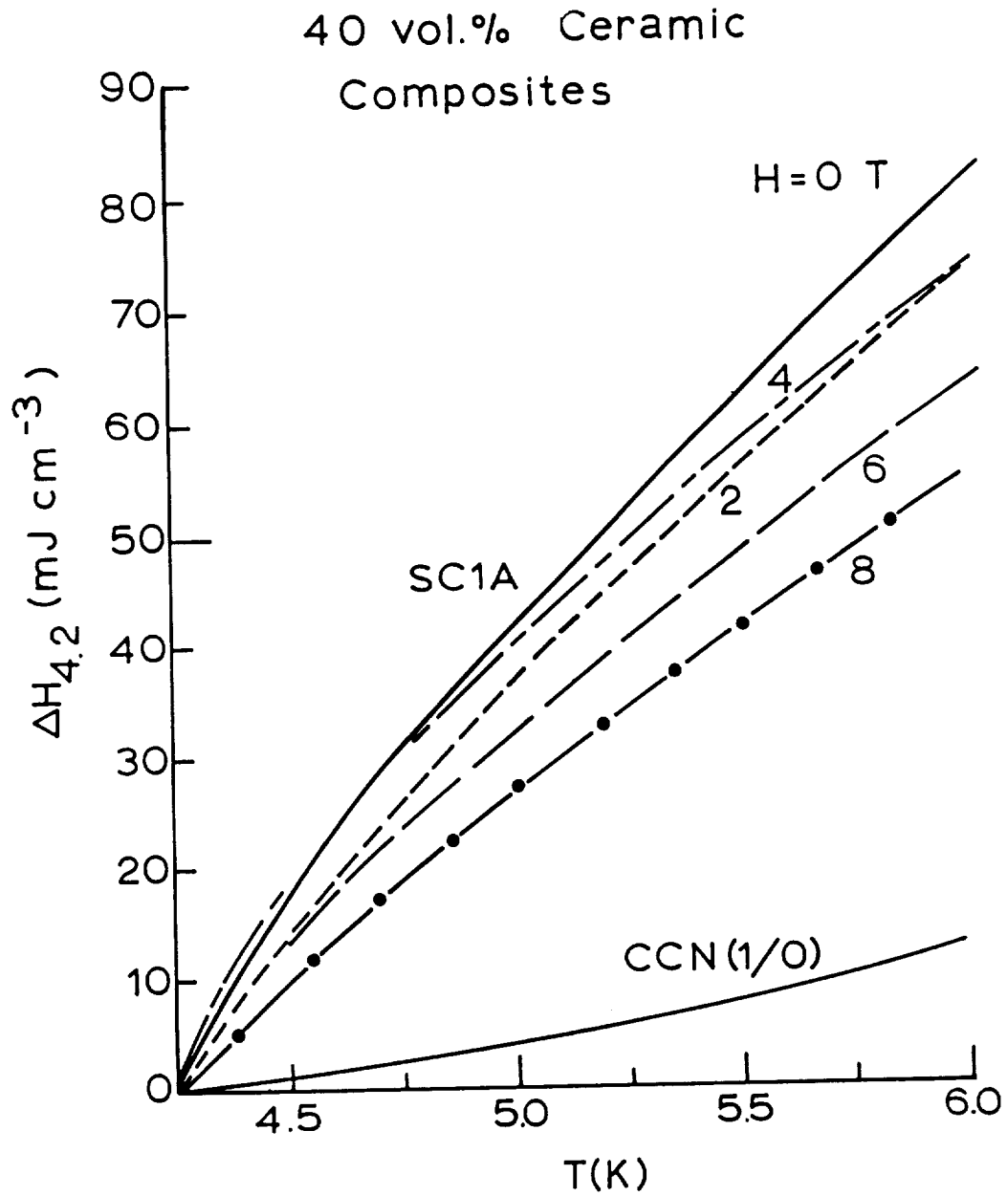It is clearly seen in Fig. A-31 that the SCIA composite has

Figure A-31. Enthalpies relative to 4.2 K for 40 vol.% powder composites of CCN(1/0) and SCIA in Envirotex epoxy.

$\Delta H_{4.2}$ values ~ 5-8 times __larger__ than that of the CCN composite, even taking into account the field dependence. Since the CCN(1/0) composite has a larger specific heat than the corresponding CCN(9/1) composite (i.e., Fig. A-28), we conclude that the SCIA composite(s) offers the __largest__ enthalpy at 6 K of all the materials studied in this program. This represents a breakthrough for the goals of the program.

Going further, on a volumetric basis $\Delta H_{4.2}$ at 6 K for the CCN(1/0) composite is about 5 times larger than $\Delta H_{4.2}$ for the Envirotex epoxy; consequently, from Fig. A-31, $\Delta H_{4.2}$ at 6 K for the SCIA composite is ~ 20-30 times larger than $\Delta H_{4.2}$ for the epoxy.

The H-field data for the SCIA composite in Fig. A-31 show a reverse ordering of the enthalpy curves between 2 and 4 T. This comes about due to the structure in the specific heat near the 4.3 K transition temperature at 4 T in Fig. A-30, but the data here are not sufficient to draw a firm conclusion about this ordering. However, this does not affect the central result here seen in Fig. A-30 that intense magnetic fields do not seriously degrade the enthalpy of the SCIA composite.

Energetics of Magnetocaloric Effects

We next consider the energetics of the magnetocaloric effects measured above and what implications these energetics have on enthalpy stabilization.

First, however, there are some subtleties involved in analyzing these data. The TdS equation for magnetic insulators is

$$TdS = mC_H dT + \mu_o mT(\partial M/\partial T)_H \, dH \qquad \text{(A-23)}$$

where m is the sample mass and C_H is the specific heat at field. Under adiabatic conditions (dS = 0), Eq.(A-23) immediately shows that ΔT_r is __independent__ of the sample mass [i.e., both terms in Eq.(1) scale with m].

However, the magnetocaloric data above are ΔT_r's for

composites whereas we are primarily interested in ΔT_r's for the ceramic powders. This separation is accomplished as a standard addenda correction,

$$\Delta T_{powder} = \Delta T_{composite} \; (1 + C_e/C_t) \qquad (A-24)$$

where C_e is the heat capacity of the epoxy component, and C_t is the heat capacity of the total composite. Equation (A-24) simply reflects the fact that the epoxy component is also heated/cooled in the magnetocaloric event. In the case of the SCIA composite, the field dependence of the specific heat of the SCIA powder (deriveable from the Fig. A-30 data, as discussed above) has to be taken into account in Eq.(A-24), and the specific heats of the two epoxies are known. The separated ΔT_r data for the CCN(1/0) and SCIA powders at 4.2 K are given in Table A-7.

<div align="center">

Table A-7

Magnetocaloric Powder Data, 4.2 K*

$\Delta T_r (K)$

</div>

Powder	2T	4T	6T	8T
CCN(1/0)	0.039	0.031	0.023	0.023
SCIA	~ 0	-0.047	-0.129	-0.175

* $\Delta T_r > 0$ corresponds to magnetization heating, and $\Delta T_r < 0$ corresponds to magnetization cooling.

To study the energetics of magnetocaloric effects in composites, we write the energy-balance equation

$$\Delta H_m = [m_e C_e + m_p C_p (H)] \Delta T_t = m_p C_p (H) \Delta T_p \qquad (A-25)$$

where ΔH_m is the magnetocaloric enthalpy, m_e and m_p are the masses of the epoxy and ceramic powder, C_e and C_p are the specific heats of the epoxy and ceramic powder, ΔT_t is the temperature change of the composite, and ΔT_p is the temperature change of the ceramic powder.

Considering first our "constructed" 40 vol.% SCIA composite

with the Envirotex epoxy from above, we estimate ΔH_m from Eq.(A-25) using the data in Table A-7, and these data are given in Table A-8.

Table A-8

Magnetocaloric Enthalpy Data, 4.2 K

40 vol.% SCIA

H(T)	ΔH_m (mJ cm^{-3})
2	~ 0
4	-4.27
6	-7.58
8	-6.06

The meaning of the Table A-8 data is as follows: If a magnet employing this SCIA composite is <u>up-ramped</u> to, say, 6 T, then there is an <u>additional</u> enthalpy of 7.58 mJ/cm^3 available for energy absorption. Conversely, if the magnet is down-ramped 6T → 0, then this amount of enthalpy appears as heat and has to be dissipated. Stated differently, on up-ramp the composite will drop in temperature 0.125 K, and on down-ramp will rise in temperature an equal amount. On comparing with the data in Fig. A-31, this magnetocaloric enthalpy stabilization at 4.2 K on up-ramp is significant.

For certain applications, it may be desirable to <u>minimize</u> the magnetocaloric energetics, and the data in Table A-7 show that this might be accomplished by using <u>balanced</u> powders of CCN(1/0) and SCIA. This concept was pursued by solving Eq.(A-25) for <u>ternary</u> composites wherein the mass ratio of SCIA/CCN(1/0) was varied, maintaining the total vol.% of ceramic powders at 50%. The results of these estimates at 4.2 K are shown in Fig. A-32 for up-ramp conditions. Here it is seen that a mass ratio of 7.5 % would eliminate magnetocaloric effects on ramping to (or from) 4 T, 2.5% for 6 T, and 3.5% for 8 T.

Thus, it is possible to impart substantial magnetocaloric enthalpy stabilization on up-ramp, Table A-8, or to balance out the magnetocaloric effects entirely, Fig. A-32. Of course, in
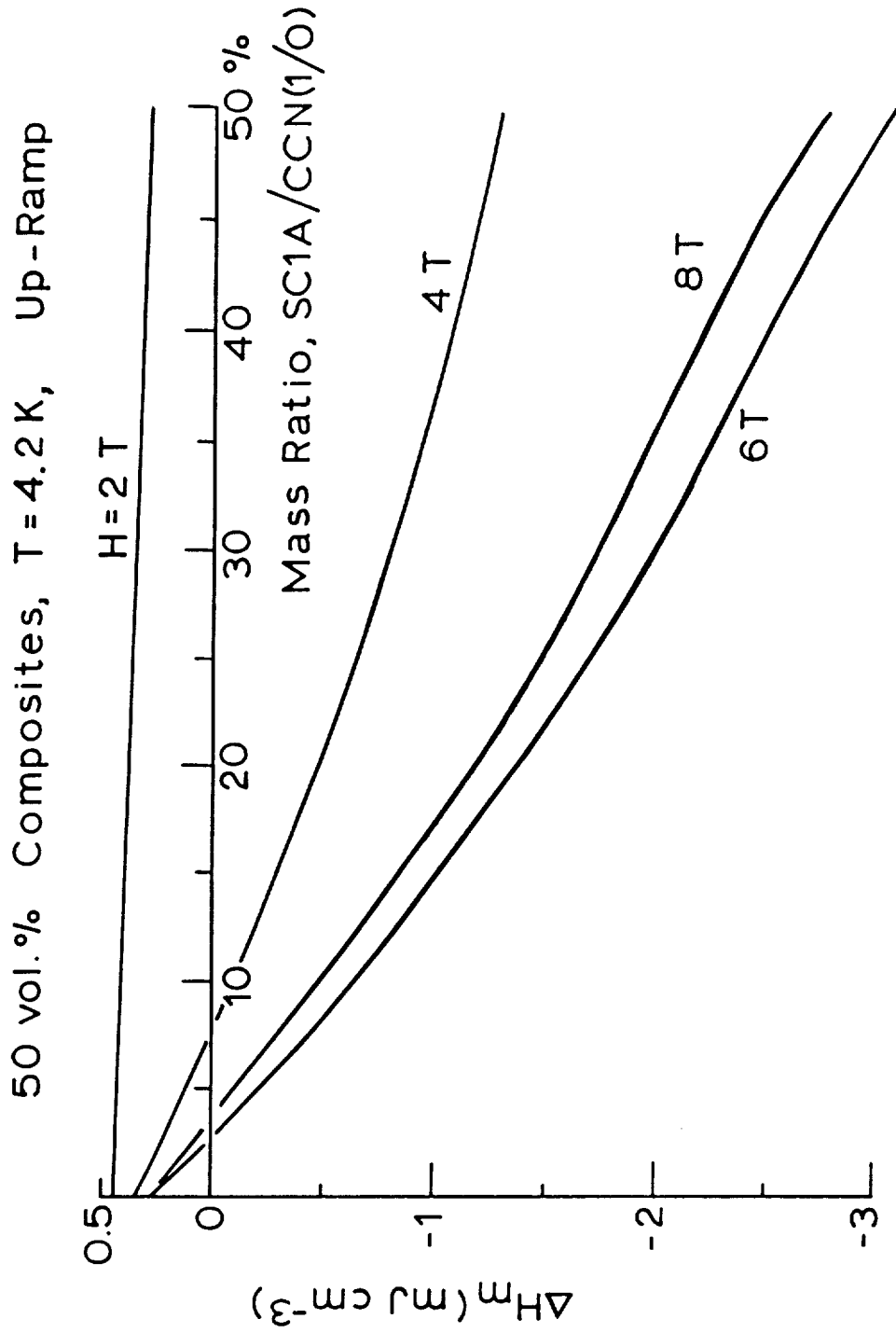
A-63

Figure A-32. Estimated mass ratio of SCIA to CCN(1/0) needed to eliminate magnetocaloric effects in composites.

the latter case, the $\Delta H_{4.2}$ enthalpy stabilization will be severely degraded, as seen in Fig. A-31.

Thermal Group Parameter

As discussed in Section A.1.0 above, for the intermediate case of thermal disturbances shorter in time than the thermal relaxation time the important parameter is the thermal group parameter,

$$\eta = \sqrt{\kappa C}, \qquad (A-26)$$

where κ is the thermal conductivity and C is the volumetric specific heat.

In this section we examine this η-parameter using the experimental data measured in the above sections. We select 40 vol.% powder composites with the Envirotex epoxy for computational purposes, and we focus on the CCN(1/0) and SCIA ceramic powders. In these estimates we assume that κ in Eq.(A-26) is magnetic-field independent (for lack of data to the contrary), and we will employ the H-field dependence of C where applicable.

The appropriate κ- and C-data for the 40% CCN(1/0) composite are given in Figs. A-19 and A-11, respectively. The H-field dependence of C is small, Fig. A-26, and will be ignored.

The appropriate κ- and C-data at zero field for the 40% SCIA composite are given in Figs. A-20 and A-15, respectively. For the field-dependent C-data we select the H = 6 T data in Fig. A-30 for the 25.5 vol.% SCIA composite with the R12142 epoxy, and these data are easily adjusted to the case of a 40 vol.% SCIA composite with the Envirotex epoxy based on the additive nature of the specific heats involved, as discussed above.

Finally, for comparison purposes, we examine η for the pure Envirotex epoxy based on the data in Figs. A-10 and A-18 (assumed H-field independent).

The results of these η-calculations are shown in Fig. A-33 for the temperature range 4-8 K. The spread in the η-values with
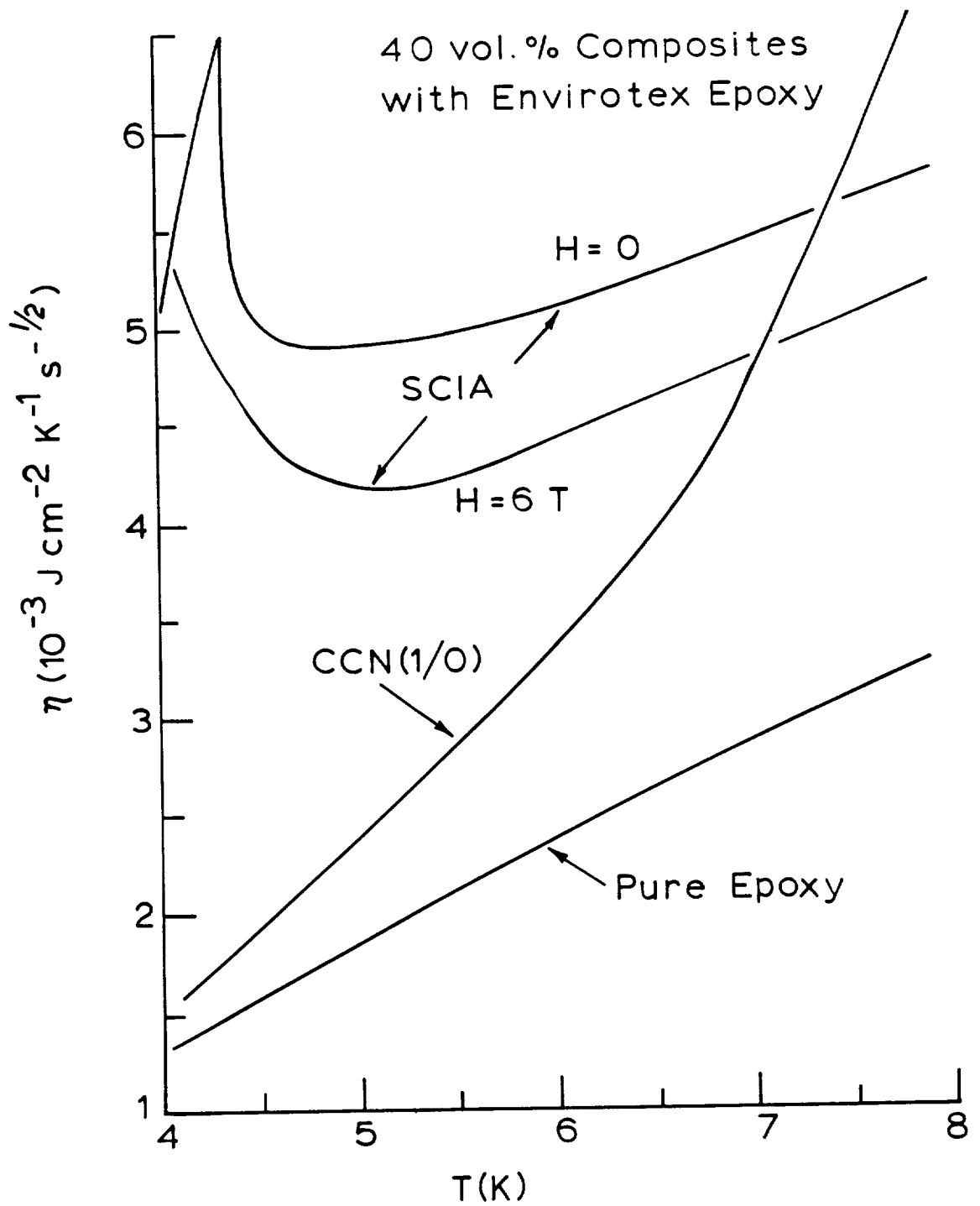
Figure **A**-33. Calculated data for the η thermal group parameter for 40 vol.% composites with the Envirotex epoxy.

magnetic field for the 40% SCIA composite is shown, and H = 6 T is chosen as a representative upper field level.

The data in Fig. A-33 show that η for the SCIA composite at H = 6 T is the largest value obtained up to 7.1 K, but above about 7.4 K η for the CCN(1/0) composite increases rapidly with temperature. In all cases, the η-values for the composites exceed that for the pure Envirotex epoxy.

The η-data for the SCIA composite in Fig. A-33 have minima between 4.7-5.1 K. The reason for this is that although C decreases with temperature above 4.3 K, Figs. A-15 ad A-20, κ increases rapidly with temperature, Fig. A-20, leading to the minimum in η according to Eq.(A-26).

The results shown in Fig. A-33 are specific to 40 vol.% composites for a one-to-one comparison and are limited to H = 6 T in the case of the SCIA composite. However, relaxing these conditions does not lead to qualitatively different results for the following reasons: On the one hand, equivalently changing the vol.%'s of CCN(1/0) and SCIA will simply shift the curves in Fig. A-33 equivalently owing to the additive nature of the specific heats demonstrated above. And on the other hand, selecting a different magnetic field strength for the case of the SCIA composite will shift the H = 6 T curve in Fig. A-33 by the square root of the suppression ratio shown in Fig. A-30 -- this factor amounts to about 70% at H = 10 T compared to the zero-field case.

A.1.5 CONCLUSIONS AND RECOMMENDATIONS

The research results obtained above clearly favor the SCIA powder additions to amorphous materials used either as dielectric insulations applied to the NbTi wire or as potting media, for the following reasons:

1. The physical properties of all amorphous materials are equivalent at low temperatures (e.g., Fig. A-2), so the results obtained here with the Envirotex and R12142 epoxy matrices are transferrable to other amorphous media (e.g., Formvar).

2. The SCIA powders enter into composites with lower resultant porosity levels (Table A-2), thus leading to improved thermal conductivities (e.g., Fig. A-21).

3. At comparable vol.% filling ratios, the SCIA powder additions lead to smaller thermal contractions (Fig. A-9), thus resulting in improved thermal shock resistance and in a closer thermal-contraction match to copper.

4. The SCIA powder additions result in a larger enthalpy stabilization relative to 4.2 K, taking into account the H-field dependence of the specific heat (Fig. A-31).

5. Assuming that stabilization on up-ramp is more important than stabilization on down-ramp, the SCIA powder additions contribute a significant magnetization-cooling stabilization component (Table A-8). However, on down-ramp this same mechanism contributes a deleterious, reversible, de-stabilization heating effect.

6. In the intermediate case of thermal disturbances, the η-parameter for SCIA powder additions is optimal up to about 7 K, even taking into account the H-field dependence of the specific heat (Fig. A-33).

Given all of the above, important caveats must be emphasized, as follows:

1. In the extreme case where the thermal disturbances are large enough to overwhelm the enthalpy of the dielectric-insulating system, the emphasis shifts to the thermal conductivity to transmit the disturbance to the helium bath. In this case, no

ceramic powder additions are called for because the epoxy alone has the larger thermal conductivity up to 5.5 K (Fig. A-20).

2. In the case that magnetocaloric heating/cooling are deleterious on <u>both</u> up-ramp <u>and</u> down-ramp, other things being equal, then <u>balanced</u> powder additions are called for as shown in Fig. A-32.   In this case, however, enthalpy-stabilization suffers, as may be seen in Fig. A-31.

References

[1] Final Report, "Dielectric Insulation for Superconductors", WPAFB Contract F33615-82-C-2227, Aug. 10, 1982.

[2] A.C. Anderson (Private communication).

[3] M. Jakob and G. Hopkins, <u>Elements of heat transfer</u> (J. Wiley, N.Y., 1957), p. 65.

[4] W.N. Lawless, Phys. Rev. <u>B14</u>, 134 (1976).

[5] W.N. Lawless, Cryogenics <u>15</u>, 273 (1975).

[6] W.N. Lawless, C.F. Clark, and R.W. Arenz, Rev. Sci. Instrum. <u>53</u>, 1647 (1982).

[7] W.N. Lawless, Rev. Sci. Instrum. <u>48</u>, 361 (1977).

[8] W.N. Lawless, Rev. Sci. Instrum. <u>42</u>, 561 (1971).

[9] R.W. Arenz, C.F. Clark, and W.N. Lawless, Phys. Rev. <u>B26</u>, 2727 (1982).

NASA Report Documentation Page

1. Report No.	2. Government Accession No.	3. Recipient's Catalog No.
NASA CR-4327		

4. Title and Subtitle	5. Report Date
Magnetic Suspension and Balance System Advanced Study - Phase II	November 1990
	6. Performing Organization Code

7. Author(s)	8. Performing Organization Report No.
R. W. Boom, M. K. Abdelsalam, Y. M. Eyssa, and G. E. McIntosh	
	10. Work Unit No.
	324-02-00-01

9. Performing Organization Name and Address	11. Contract or Grant No.
Madison Magnetics, Inc. 216 Walnut Street Madison, Wisconsin 53705	NAS1-18279
	13. Type of Report and Period Covered

12. Sponsoring Agency Name and Address	Contractor Report 7/86 to 5/90
National Aeronautics and Space Administration Langley Research Center Hampton, VA 23665-5225	14. Sponsoring Agency Code

15. Supplementary Notes

Langley Technical Monitor: Richmond P. Boyden
Final Report – SBIR Phase II

16. Abstract

The design improvements for the system encompass 14 or 18 external superconductive coils mounted on a 8' x 8' wind tunnel, a superconductive model core magnet on a holmium mandrel to fit an F-16 model, model wings of permanent magnet material $Nd_2Fe_{14}B$, and fiber-glass epoxy structure. The MSBS advanced design is confirmed by the successful construction and test of a full-size superconductive model core solenoid with holmium mandrel. The solenoid is 75 cm long and 12.6 cm in diameter and produces 6.1 tesla for a hold time of 47 minutes. An integrated coil system design of a new compact configuration without specific coils for roll or pitch shows promise of simplicity; magnet reductions of 30 percent compared to the most recent 1985 design by Madison Magnetics are possible.

17. Key Words (Suggested by Author(s))	18. Distribution Statement
magnetic suspension magnetic balance superconducting magnets wind tunnel balance	Unclassified-Unlimited Subject Category 09

19. Security Classif. (of this report)	20. Security Classif. (of this page)	21. No. of pages	22. Price
Unclassified	Unclassified	228	A11